Utrecht University

An Investigation of Mantle Attenuation using ScS Reverberations

Henry Brett

March 16, 2018

CONTENTS

Name: Henry Brett
Student Number: 5806771
e-mail: h.t.g.brett@students.uu.nl
Telephone: +31641169799
Supervisor: Prof. Dr. Arwen Deuss
Credits: 30

ABSTRACT

A method of measuring whole mantle attenuation from frequency spectra of multiple core reflected ScS body waves is presented and applied to a global data-set. We compare attenuation measurements and shear wave tomography to identify regions of temperature anomalies, water and partial melt in the mantle using empirically derived relations between these properties. Specific regions are studied in detail such as: (1) South America, which appears to have a temperature dominated attenuation structure, but requiring partial melt or water to increase absolute values of attenuation. (2) Fiji, whose attenuation structure reveals the likely presence of partial melt. (3) Japan which also has a temperature controlled attenuation structure but requiring partial melt to increase absolute values. The role of focussing and de-focussing from velocity structure on attenuation measurements is investigated by comparing measured attenuation to 3D synthetic seismograms. This leads to the insight that low attenuating regions are affected more by foccussing and de-foccussing but highly attenuating ones are not.

1 INTRODUCTION

Attenuation is the loss of seismic energy due to inelastic properties within the Earth (defined here as the conversion of kinetic energy to thermal). It is important as it has the potential to provide an independent constraint on temperature, volatile content and partial melting in the mantle. This would be invaluable as current mantle tomography for velocity variations produces non-unique solutions for these three properties. A correlation between high temperatures and high attenuation has been observed through numerous studies and by comparing V_s (shear wave velocity) to attenuation structure it is thought that the effect of temperature variations on V_s in specific regions will be discernable (Dalton et al. (2009),Romanowicz and Mitchell (2015)). Attenuation remains, however, a notoriously difficult property to accurately and reliably measure from seismic data (Romanowicz and Mitchell, 2015). Velocity structure within the mantle causes un-even distributions of seismic energy. This is known as focusing and de-focusing (or scattering) of seismic energy and will influence the measured amplitude at the surface and therefore will influence attenuation measurements. Focusing energy has the potential to reduce measured attenuation from the true value and de-focusing will make attenuation appear greater.

Measuring mantle attenuation can be done using normal modes, surface waves and body waves. Normal modes are free oscillations of the entire Earth which by their nature sample whole Earth structure (with varying depths of sensitivity). This has made normal modes a powerful method for measuring large scale mantle attenuation structure. Surface waves travel across the surface of the Earth and primarily sample the upper mantle. It has been found that where normal modes and surface waves sample the same volume they measure systematically different attenuation. This study will use body waves; body waves are short period data compared to long period surface waves and normal modes and requires ray theory. They travel the mantle and core but we will focus on body waves which only travel through the mantle. Due to body waves relatively short period they should be more sensitive to small attenuation structure than normal modes while also able to sample more of the mantle than surface waves.

Throughout this research we use horizontally polarized shear waves to measure attenuation, this is due to their high sensitivity to parameters thought to influence attenuation. ScS phases are shear waves which travel from an earthquake through the mantle, reflect from the Core Mantle Boundary (CMB) and return to the surface, where it is recorded. ScSScS phases do the same but with another reflection from the CMB and can be thought of as an echo or reverberation of the ScS phase. The raypaths are shown in Figure 1. Looking at event-station pairs with low epicentral distances, $\theta < 5°$, (the distance between the source and seismometer) the ScS reverberations are well recorded and clean. This provides an interesting dataset to investigate attenuation as the ScS and ScSScS phases approximately sample the same volume of mantle between earthquake and reciever with each reverberation. Theoretically, if there is no influence from focussing and de-focusing, any amplitude differences between the ScS and ScSScS phase should be due to attenuation and geometrical spreading within the mantle.

The earliest use of ScS phases to calculate mantle attenuation was conducted by Kovach and Anderson (1964). Kovach and Anderson (1964) used analogue data and yet despite the increased measurement uncertainty there was already evidence for large lateral differences in attenuation. After these early efforts and the advent of digital seismometers modern studies involving larger datasets to measure Q (Anelastic Attenuation Factor) was published by Revenaugh and Jordan (1987). Revenaugh and Jordan (1987) (along with other researchers: Sipkin and Jordan (1980) and Lay and Wallace (1983)) using ScS reverberations found that average mantle Q for ScS phases was between 220-240. Revenaugh and Jordan (1987) focused initially on events from Tonga recorded on station KIP (Hawaii) and drew conclusions on whole mantle attenuation structure. Revenaugh and Jordan follwed up with a four part series of papers using ScS reverberations to infer numerous properties (including attenuation) of different layers of the mantle (Revenaugh and Jordan (1991a), Revenaugh and Jordan (1991b),Revenaugh and Jordan (1991c), Revenaugh and Jordan (1991d)). Furthermore, they used sScS phases (similar to ScS but initially travel towards the surface) which will also be used in this research to show reliability of attenuation results. One of the main limitations of their research however was the lack of large volumes of data which meant that they had to analyse ScS phases with larger epicentral distances ($\theta > 10°$). This will lead to errors as the ScS and ScSScS phases will not have sampled the exact same attenuation structure.

Kanamori and Rivera (2015) provide us with the most up to date ScS attenuation research making use of a larger dataset (220 event-station pairs). They found that attenuation varies rapidly over short distances and that there is no obvious correlation between attenuation and travel times. Their research relied on a time domain approximation to calculate attenuation and only briefly compared their results to 3D synthetic seismograms, essential for understanding the effect of focusing and de-focusing caused by velocity structure (which they assumed to be negligible).

To quantitatively interpret attenuation measurements in the context of temperature, water content and partial melt in the mantle requires empirical relationships determined by laboratory experiments. The sensitivity of attenuation to temperature variations was first suggested by Anderson (1967), increasing temperature will result in higher attenuation and slower shear wave velocity and was shown experimentally by Faul and Jackson (2005). Furthermore, the effect of water in the mantle on attenuation has been investigated ((Karato, 2003), (Karato and Jung, 1998)) and was found to increase attenuation greatly and decrease velocity moderately. Finally, the effect of partial melt is dependant on the melt mechanism. It has been shown through a combination of numerical modelling and laboratory experiments that partial melting will decrease velocity but not significantly affect attenuation when a melt-squirt mechanism is in effect (Hammond and Humphreys, 2000), while a grain-boundary sliding mechanism will significantly increase attenuation but produce a relatively moderate decrease of velocity (Faul et al. (2004) and Jackson et al. (2004)).

Dalton et al. (2008) produced a 3D shear-wave attenuation model for the whole mantle using fundamental mode Rayleigh (Surface) waves. Then Dalton et al. (2009) brought together all the major empirical laboratory-measured relations between attenuation, temperature, water content and partial melting discussed above for 150km deep olivine and used this to interpret their global attenuation model. Dalton et al. (2009) concluded that temperature anomalies can account for the majority of attenuation and seismic velocity anomalies but that water and compositional differences are required to explain some regions.

We will compare and improve upon the time domain approach used by Kanamori and Rivera (2015) but will make a more extensive use of a frequency domain spectral ratio method (Tonn, 1991). This spectral ratio method produces more reliable values of attenuation by calculating an average attenuation for a range of frequencies. Furthermore we compare 3D synthetic seismograms with a constant attenuation factor (Tromp et al., 2010) to our measured attenuation to provide a greater understanding of the effects of focussing and defocussing on attenuation calculations. Finally we will interpret our results on a regional and global level and use the empirical relations combined by Dalton et al. (2009) to provide detailed interpretations of specific regions.

The first section in this paper describes the pre-processing, data collection and attenuation measurements. The second section presents the results and interprets them globally, investigating travel time differences and outlining the differences between synthetic seismograms and the data. This section continues by investigating specific regions with high data-density. In the final section the limitations, underlying assumptions of this method and potential causes of attenuation in specific regions are discussed.

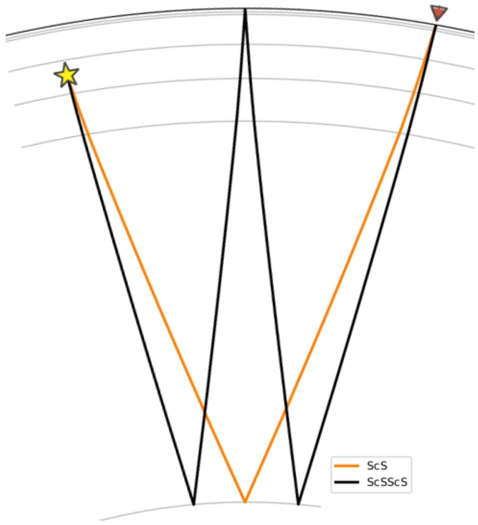

Figure 1: The ray paths taken by ScS and ScSScS phases. Epicentral distance has been exagerated to $\theta = 20°$ for clarity. Figure generated using ObsPy and Taup.

2 Methodology

2.1 Data Selection

We started with investigating event-station pairs also used by Kanamori and Rivera (2015), in order to verify our methodology. Data was collected for one hour after the first P-wave arrival and for event-station pairs occuring after 2011 to allow simultaneous collection of 3D synthetic seismograms (Tromp et al., 2010) using the *BREQ_FAST* request process. ScS and ScSScS phases are best recorded on long period horizontal component seismograms, thus LHN and LHE channels were collected with a 1Hz sampling rate.

After the event station pairs of Kanamori and Rivera (2015) had been collected and interpreted event-station pairs which met three key criteria were collected: (1) Events must have moment magnitudes between 6.3 and 7.7. Events with $M_w < 6.3$ did not have enough energy to produce clear ScS and ScSScS phases. Equally, if the magnitude is greater than $M_w = 7.7$ then there is a long wave train which does not produce the impulse like arrivals neccessary for reliable attenuation calculations. (2) Epicentral distance (distance between event and station) must be less than 5°. This is to ensure ScS and ScSScS phases sample the same attenuation structure. (3) Events had to be distinct and not contain arrivals from other events. Appendix Table A1 provides all the event-station information.

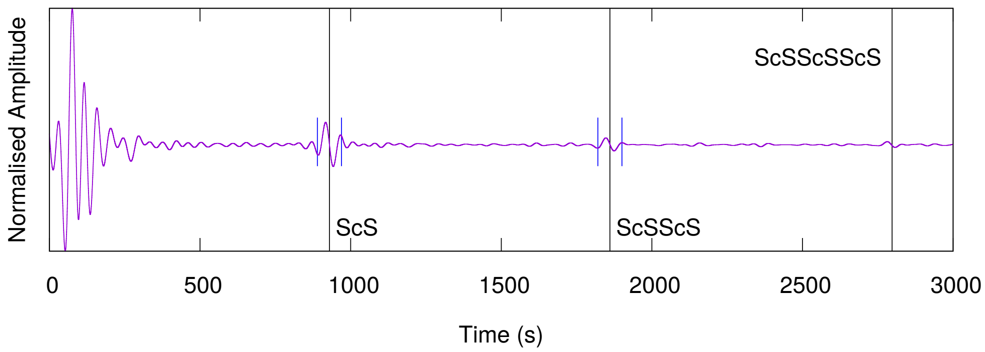

Figure 2: Butterworth filtered data with ScS and ScSScS arrivals shown by the vertical black lines. Blue vertical lines indicate length of time windows used for attenuation calculation. A ScSScSScS arrival is also shown, however never used for interpretation due to poor signal to noise ratio. Data comes from station ADK in the United States, for an event on the 24th of July 2011, LH1 00 component with M_w: 6.9.

2.2 Pre-Processing

The first processing steps involved removing the instrument response of the data and converting velocity to displacement. Then the data were rotated along the great-circle-path and only the transverse component kept. This is because the transverse component contains all the SH energy (Revenaugh and Jordan, 1987). Hereafter all the processing steps are conducted on both un-rotated and transverse components.

The data's sampling rate is too low for later analysis of the ScS and ScSScS phases (shown by comparing Figures 6a and 6b) therefore data is resampled from a dt of 1s to 0.05s. The data still contains other phases and higher frequency noise, thus butterworth filtering is conducted between 0.008Hz and 0.0275Hz with 4 nodes and 2 passes. The result of this processing is seen in Figure 2. The predicted ScS and ScSScS arrival times are calculated from the AK135 travel time model (Kennett et al., 1995) as shown on Figure 2. The predicted arrival times are accurate to within 10 seconds and are used to define 80 second time windows encompassing the ScS and ScSScS phases.

2.3 Measuring Q: Time Domain

Attenuation is measured using methods in the time and frequency domain. The time domain method is simpler to implement and is adapted from Kanamori and Rivera (2015), this allows initial comparison of results.

Quality factor Q is a dimensionless parameter used to represent energy loss by attenuation, defined by:

$$Q = 2\pi \frac{E_{max}}{\Delta E} \tag{1}$$

where E_{max} is the maximum energy contained in one period and ΔE is the energy lost by

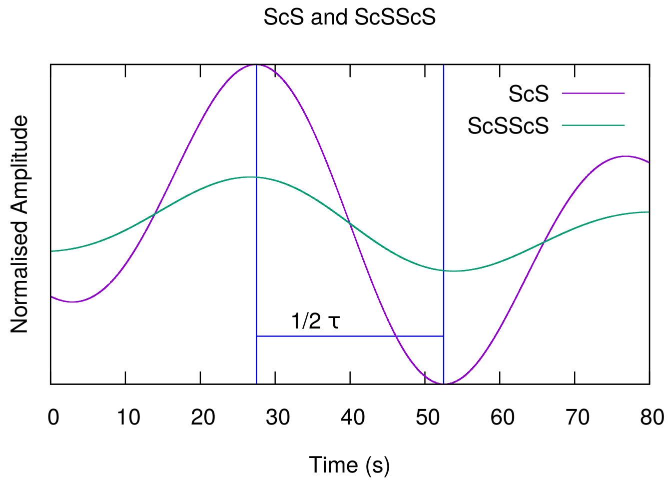

Figure 3: The 80 second windows shown on Figure 2 of the ScS and ScSScS phases plotted on top of eachother. blue lines indiciate how $\frac{1}{2}\tau$ is read from the data. In this case $\frac{1}{2}\tau = 24$. Data is the same as Figure 2.

each cycle (Romanowicz and Mitchell, 2015). For this research the maximum energy is measured from the amplitude of the ScS arrival and then the energy loss is measured from the amplitude of the ScSScS arrival. It can be seen from Equation 1 that high energy loss results in small values of Q, as such $q = 1/Q$ is also used when interpreting regions of high attenuation.

Kanamori and Rivera (2015) used the following equation to relate the amplitude ratio of ScSScS and ScS to attenuation,

$$\left|\frac{ScSScS}{ScS}\right| = g \cdot exp\left(-\frac{\pi f t_r}{Q}\right) \tag{2}$$

where $\left|\frac{ScSScS}{ScS}\right|$ is the amplitude ratio of the ScSScS and ScS phases, t_r is the difference in arrival times between ScS and ScSScS and f is the dominant frequency measured from the seismogram. In seismology when calculating attenuation the frequency band of interest must be defined and for the time domain method one dominant frequency is selected. Measuring the the time difference between the highest and lowest peaks in ScS gives half the dominant period, $\frac{1}{2\tau}$, from this we calculate $f = \frac{1}{2\tau}$. This is seen on Figure 3. Finally, g is the geometrical spreading which is given analytically by

$$g = \frac{2 - h/H}{4 - h/H} \tag{3}$$

where h is the event depth and H is the depth to the CMB.

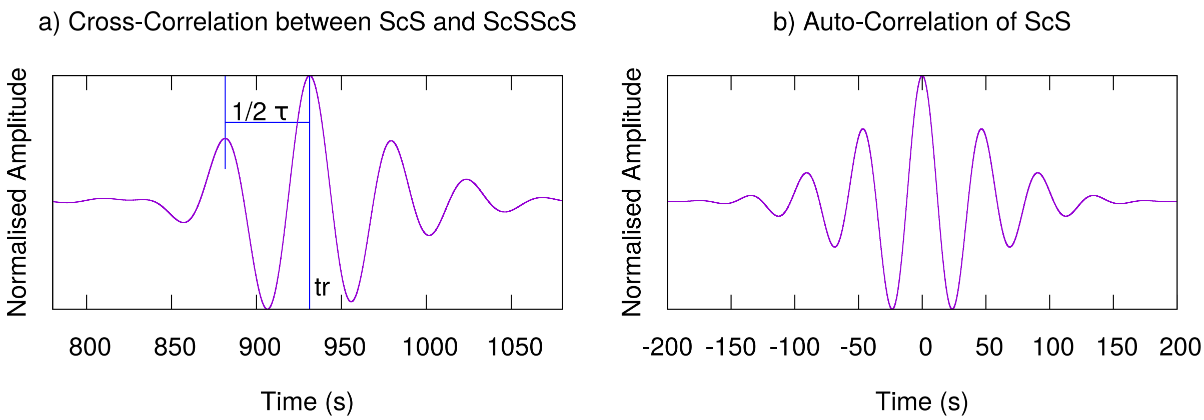

Figure 4: Cross-Correlation between ScS and ScSScS and Auto-Correlation of ScS. The Cross-Correlation shows how τ and t_r is selected. Same data as Figure 2.

Re-arranging Equation 2 produces the time-domain equation which we use to measure Q

$$Q = -\pi f t_r \Big/ ln\left(\left| \frac{ScSScS}{ScS} \right| \Big/ g \right) \tag{4}$$

While the approach used by Kanamori and Rivera (2015) works, I found their results difficult to reproduce with the Q values differing by ±20. Furthermore the values did not agree well with the more robust frequency domain approach (see section 2.4). I suspect this is due to the time domain method only calculating the attenuation of a single frequency of ScS while in reality a range of frequencies are attenuated. Furthermore, the amplitude ratio calculation was naive; it was simply defined as the difference between the largest values.

To improve the time domain approximation I calculated the cross-correlation and auto-correlation between the time window's of the ScS and ScSScS phases (Figure 4). Using the auto- and cross-correlation improves the calculation in three ways: (1) It provides a more reliable measurement of t_r. Previously t_r was given by the time difference of the ScS and ScSScS maxima, ignoring the rest of the waveform, but by calculating a cross-correlation the whole waveforms of ScS and ScSScS are compared. Looking at Figure 4 it can be seen that the maximum value of the cross correlation corresponds to the time difference between the ScS and ScSScS where their waveforms are most similar. This then provides us with a better measurement of t_r taken directly from the data, improving upon the modelled arrival from AK135 Kennett et al. (1995) by as much as 10s. (2) A more representative value of "dominant frequency". The method used by Kanamori and Rivera (2015) calculated the dominant frequency purely from the ScS seismogram. However, by using the time difference between the largest and second largest values in the cross-correlation as a value for $\frac{1}{2}\tau$ a dominant frequency which combines the frequency content of ScS and ScSScS is measured. (3) An amplitude ratio calculation which combines the amplitudes of all frequencies, not just the amplitude of the dominant frequency. Using the largest values of the cross-correlation (C) between ScS and ScSScS and auto-correlation of the ScS phase (AC) we now calculate the ratio of the ScS and ScSScS phases thus:

$$\left|\frac{ScSScS}{ScS}\right| = \frac{(C(t))_{max}}{(AC(t))_{max}} \tag{5}$$

This is more robust as it will take into account not just the amplitude at the maxima of the ScS and ScSSCS phases but of the whole waveform.

2.4 Measuring Q: Frequency Domain

To measure Q in the frequency domain a spectral-ratio method adapted from Kanamori and Rivera's time domain equation is derived. This was later found to also be used by a near surface seismic study investigating different methods of measuring attenuation by Tonn (1991). Taking a fast fourier transform of the ScS and ScSScS windows the frequency content of each phase is calculated. The spectral-ratio method uses the following equation to evaluate Q:

$$ln\left(\frac{ScSScS(f)}{ScS(f)}\right) = \left(\frac{-\pi t_r}{Q}\right) f + ln(G) \tag{6}$$

where ScSScS(f) and ScS(f) are the frequency dependent amplitudes and G is the geometrical spreading measured from the spectral plot. It can be seen that this equation is a relatively simple re-arrangement of Equation 4 with the exception of the geometrical spreading factor. G and g (from equation 3) are both values of geometrical spreading but they are not the same. G is measured from the spectral ratio method using equation 6 while g is calculated analytically. Plotting the ratio $ln\left(\frac{ScSScS(f)}{ScS(f)}\right)$ as a function of frequency and fitting a line through the points between 0.008Hz and 0.0275Hz (the same frequencies used when butterworth filtering during pre-processing, section 2.2) allows a gradient, m, to be estimated which is equal to:

$$m = \left(\frac{-\pi t_r}{Q}\right) \tag{7}$$

and thus Q can be evaluated.

For our example of the 2011 ADK event the frequency spectra of ScS and ScSScS are shown in Figure 5. We find that the ScS spectra contains higher frequencies than the ScSScS spectra. This is because higher frequencies are more strongly attenuated than lower frequencies. Therefore ScSScS, which travels through the mantle twice, will have lost more of its higher frequencies than ScS, which only travels through the mantle once. It is the ratio of this preferential attenuation that is measured to produce a value of Q for the spectral ratio method.

The amplitude ratio of $ln\left(\frac{ScSScS(f)}{ScS(f)}\right)$ against frequency is shown on Figure 6. The regression provides a gradient estimate and is shown by the green line fitted through the frequencies between 0.008Hz and 0.0275Hz.

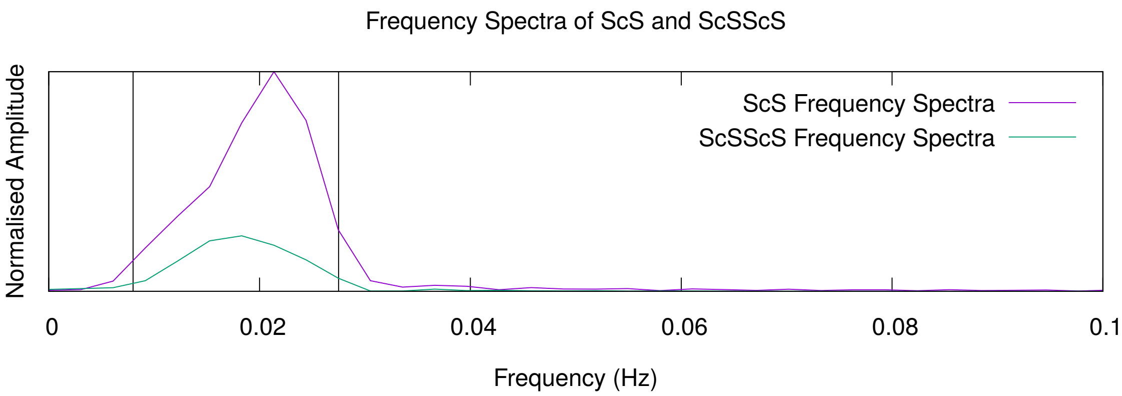

Figure 5: The frequency spectrum of ScS and ScSScS. Black lines show the frequency window between 0.008Hz and 0.275Hz upon which attenuation calculations are conducted. Same data as Figure 2.

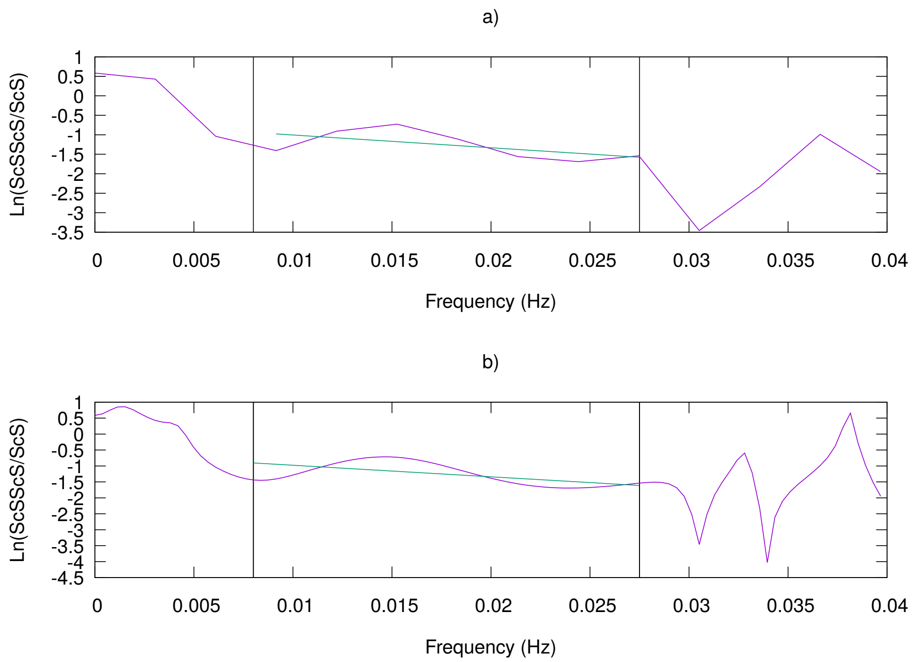

Figure 6: a) Same data as Figure 5 without initial re-sampling of data or zero-padding of the fast fourier transform. b) Same data as Figure 5 with initial re-sampling of data and zero-padding of the fast fourier transform. The black lines show the window between 0.008Hz and 0.0275Hz where a line is fitted through the data. The green line is the line fitted through the data points using least squares and the gradient of that line provides us with an estimate for Q.

The resolution and number of data points in the frequency calculation for data sampled at 1Hz is not ideal (see Figure 6a), providing less than 10 points to fit a line. This highlights the need for prior re-sampling and zero-padding of the Fourier Transform (Figure 6b). Figure 7 provides a quick overview to the processing.

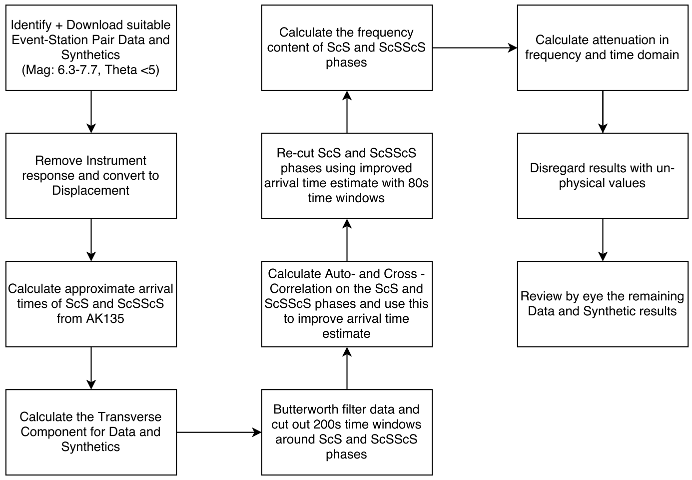

Figure 7: Processing workflow from data collection to quality control of results.

3 RESULTS AND INTERPRETATION

We will now use the methods described in section 2 to measure attenuation for event station pairs. See Appendix Table A1 for a list of all event-station pair information and corresponding Q values. Firstly the quality control and selection methodology for the results is explained, followed by a presentation of results on a global scale. An explaination of how attenuation measurements and velocity structure is interpreted is presented followed by a discussion of attenuation measured in regions with high data density. Finally, a comparison between attenuation measured from data and attenuation measured from synthetic seismograms is made to identify the effects of focussing and de-focussing and results from other ScS reverberations are discussed.

From each event-station pair a time domain and frequency domain attenuation value was calculated for the north, east and transverse components of the seismogram, often for two instruments. This provided on average 12 values for attenuation to choose from. The combined improvements in the time domain method (using the cross- and auto-correlation, explained in section 2.3) resulted in greater agreement between the time domain Q value and the frequency domain Q value. As an example, I measured Q in both time and frequency for the event on the 24th July 2011 for station ADK (same data used by figures 2-6). Kanamori and Rivera's method resulted in a Q(time-domain) of 100, however after adjusting the time domain method to use values from cross- and auto-correlations Q(time-domain) was 90. This agrees much better with the value of Q calculated in the frequency domain: 100. Despite these improvements to the time domain method Figures 8 and 9 show that the two methods agree approximately but that the frequency domain produces, on average, higher values of attenuation. I believe this is due to the frequency domain method measuring attenuation of the whole frequency spectrum and not just the dominant frequency. This makes it a more robust and reliable method than the time domain method and as such the frequency domain attenuation value will be used throughout the interpretation of our data.

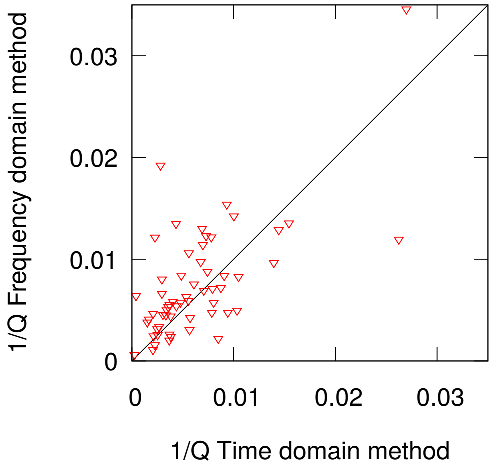

Figure 8: Comparison of the Attenuation values calculated in the time and frequenciy domains for the same event station pairs after quality control of results. $q = 0.005$ is equal to mantle average $Q = 220$

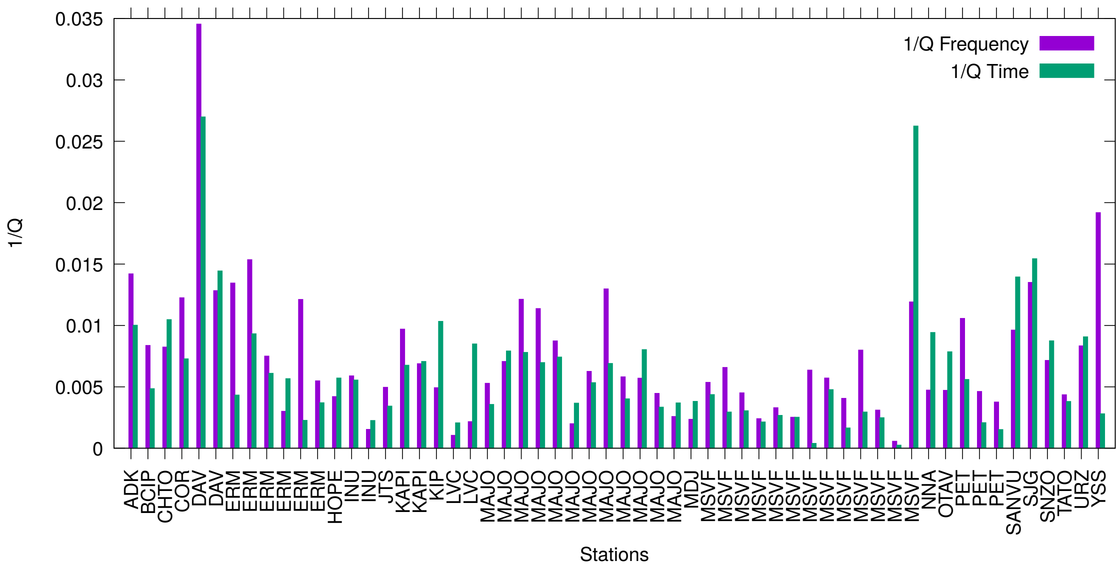

Figure 9: Comparison of the Attenuation values calculated in the time and frequenciy domains for all the event station pairs after quality control of results.

To decide which of the components and instruments attenuation values were more valid than others and to remove anomalies from interpretation a semi-automatic routine was conducted. Results which met the following three criteria were considered valid: (1) Results with Q values less than 0 were considered invalid (ie. waves had somehow gained energy relative to the geometrical spreading factor). This was normally found to be caused by the simultaneous arrival of other phases producing an increase in high frequency content relative to low or possibly effects of foccussing. (2) Results must have a travel time difference, t_r, of between 920s and 950s. From observing many seismograms any event-station pair which did not meet this criteria did not show clean/visible ScS and ScSScS phases. (3) Measured geometrical spreading has to be between 0 and 1. Equation 6 shows that the y-intercept of Figure 6 gives us: $-ln(G)$ where G is geometrical spreading factor. Geometrical spreading geater than 1, or less than 0 is considered an invalid solution. If G is greater than 1 it implies geometrical spreading focused energy. If G is less than 0 it implies that spreading dissipated all the seismic energy.

Often for an event station pair all three components (North, East and Transverse) would pass these criteria, at which point the transverse component would be chosen. The transverse component combines the energies of both the North and East components and provides a more accurate value of attenuation. If the transverse component did not pass the above criteria then the North and East components would be checked by eye and the noisier data disregarded. This is similar to Kanamori and Rivera (2015) who only rotated data when the signal to noise ratio was acceptable.

Finally all the remaining event-station pairs are checked by eye to ensure they have an acceptable noise level and are not corrupted by other signals. Figure 10 shows the standard output produced after all the above processing for one event station pair. This process results in 58 valid event-station pairs out of the 320 Event-Station pairs collected. This is a pass rate of less than 16% and is due mostly to the pollution of the ScS and ScSScS time windows with other signals of the same frequency band. Appendix Tables A1 and A2 provide the event-station information and corresponding results respectively. Appendix Figures A57 to A58 provide figures of the data and calculation for all event-station pairs as shown in Figure 10.

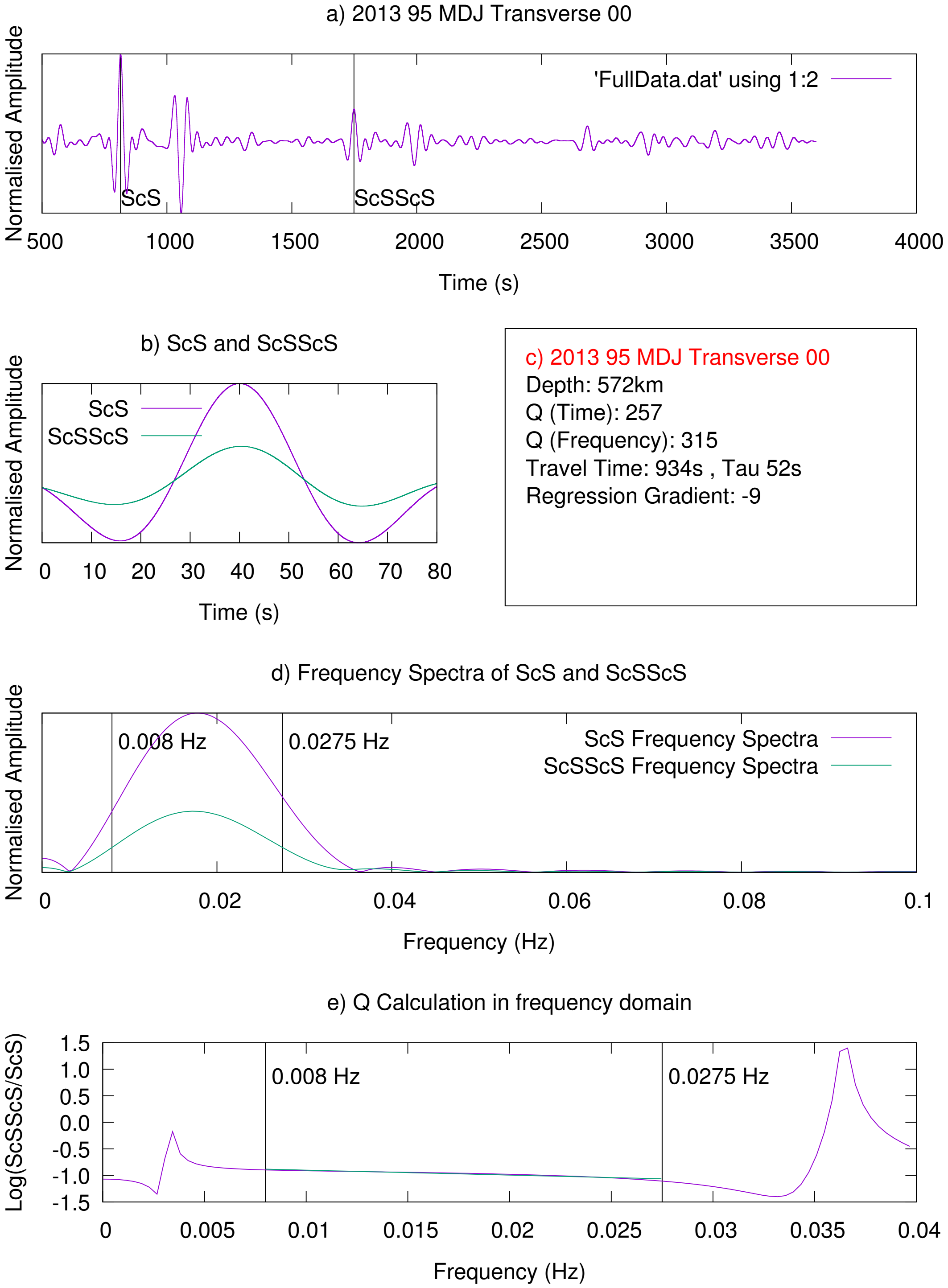

Figure 10: a) Seismogram after butterworth filtering and the locations of the ScS and ScSScS arrivals. b) 80 second ScS and ScSScS time windows plotted on top of eachother. c) Year and Day number (Normal Date: 05/04/2013), Station Name, Component, Instrument, Event depth, Q(time), Q(Frequency), time difference between ScS and ScSScS and the value of the frequency spectra gradient. d) The frequency spectra of the ScS and ScSScS phases and e) Graph upon which spectral gradient is calculated. The green line shows the line fitted through the data. The corresponding figure for all 58 event-station pairs which passed quality control is provided by Appendix Figures A57 to A58.

3.1 Global Results

Figure 11 shows the distributions of the stations used in this study that produced valid results. The condition that seismic events have to be within 5° epicentral distance of the stations resulted in the majority of event-station pairs being concentrated along known seismically active regions. Subducting plate margins and volcanic islands are especially well sampled. Figure 12 shows a map of all our measurements of $1/Q$ (larger values of $1/Q$ mean increased energy loss / high attenuation, Equation 1) and Figure 13 shows the travel time difference between ScS and ScSScS for our measurements.

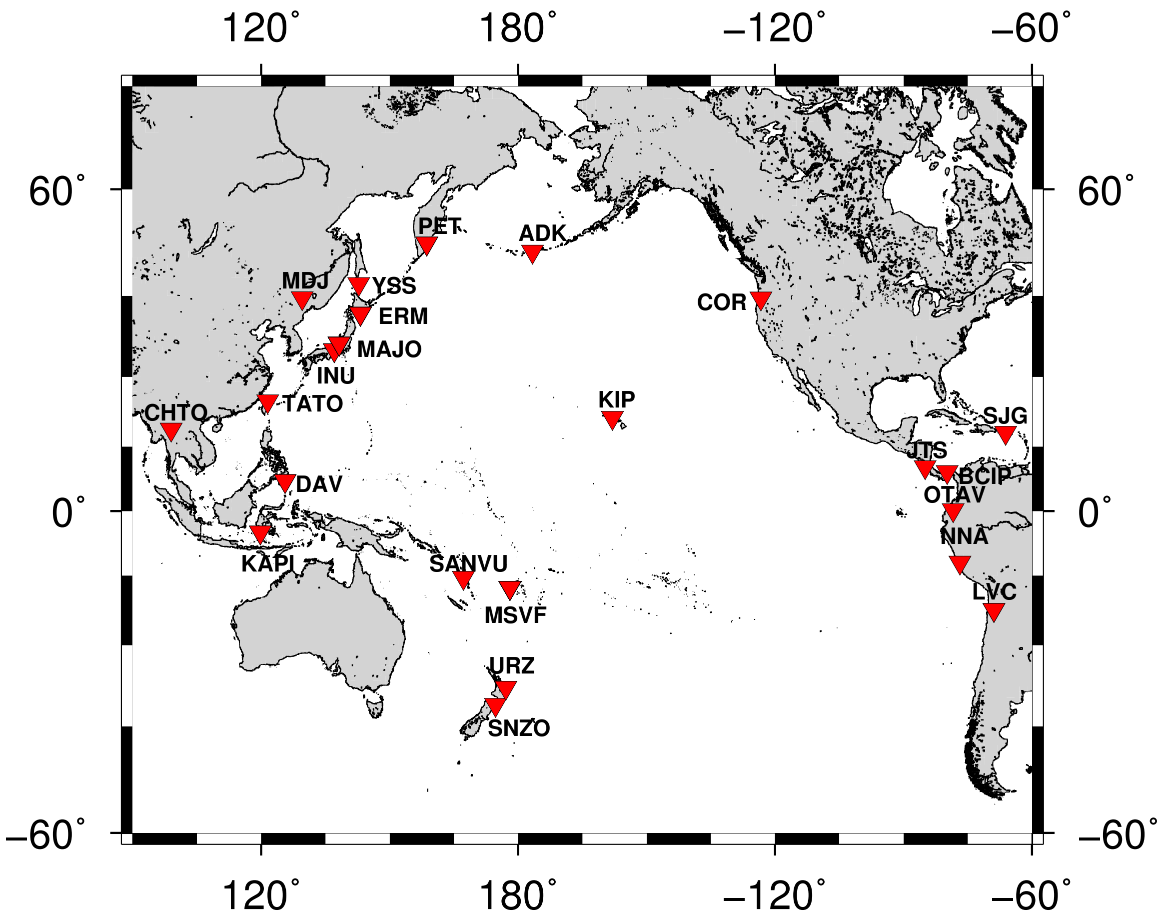

Figure 11: Location and name of all stations used

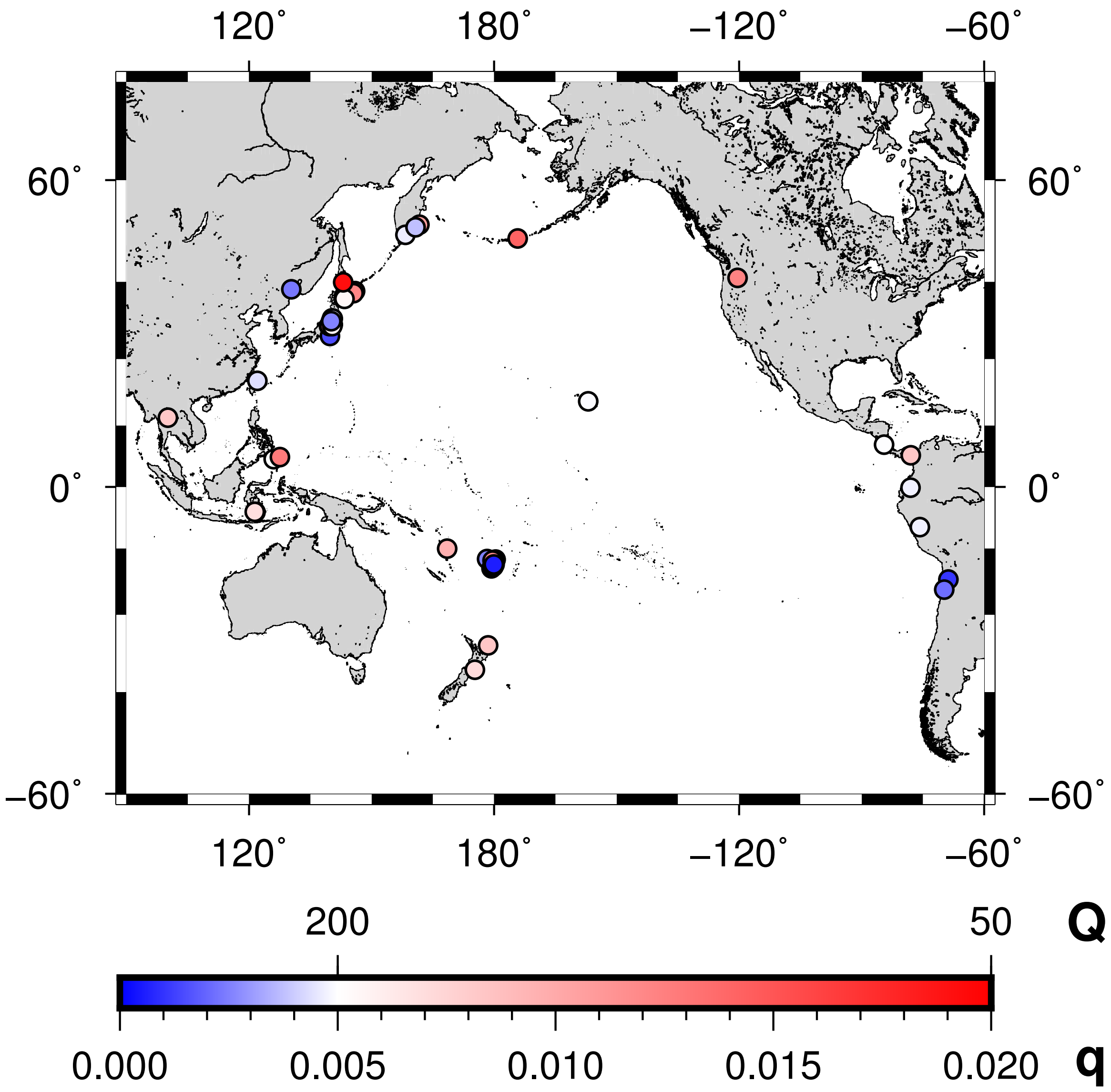

Figure 12: Measurements of attenuation plotted globally. Attenuation values are plotted at the halfway point between station and earthquake.

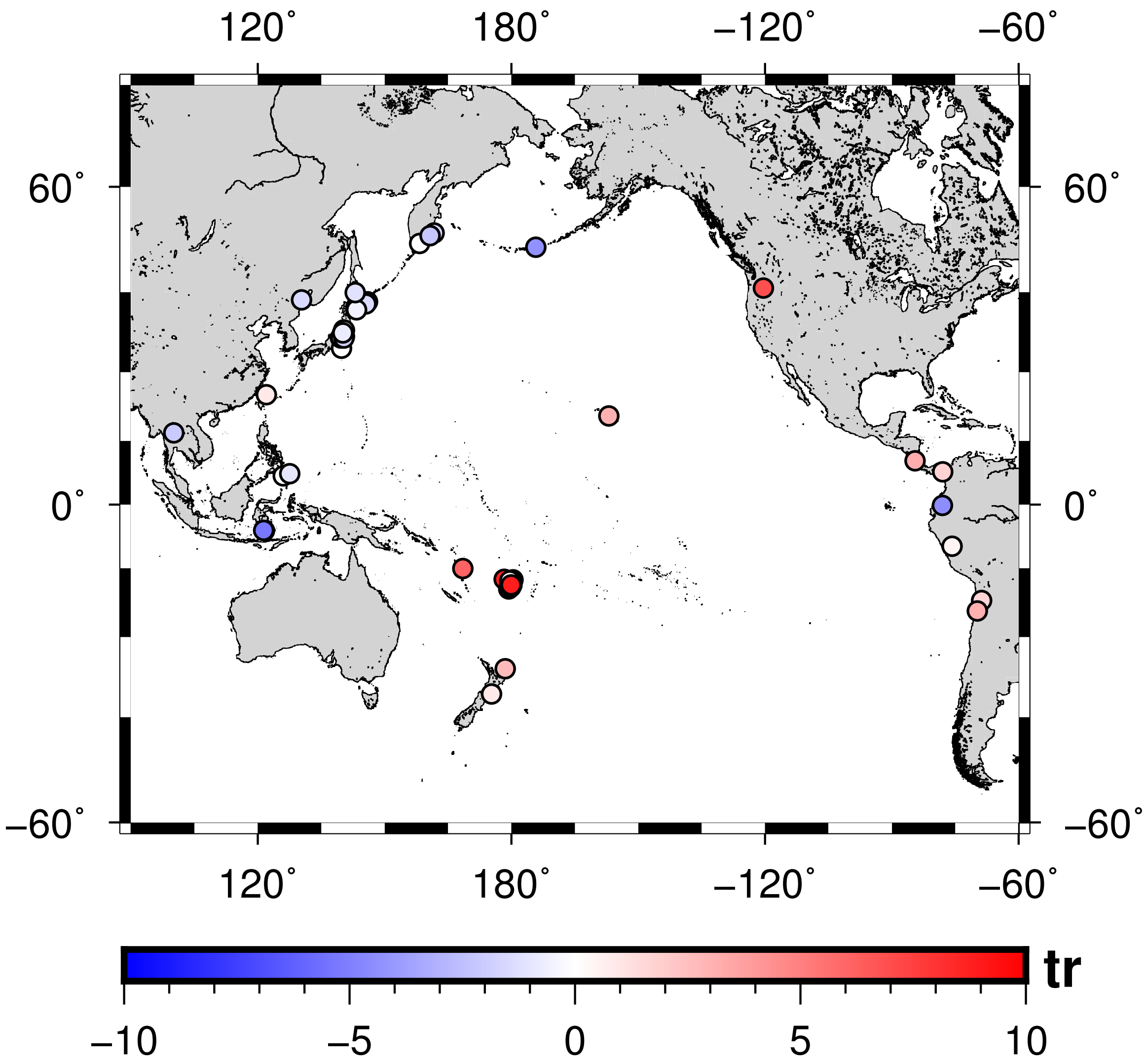

Figure 13: Travel time anomalies between ScS and ScSScS relative to AK135 across the globe. To take into account different epicentral distances t_r is calculated as the the measured value minus the value from the AK135 travel time models. Thus positive values occur in regions of lower shear wave velocity and negative values in regions of higher shear wave velocity.

3.2 Interpreting Attenuation Measurements

To understand and interpret our results we must consider the properties of the mantle that affect attenuation. There are three mantle properties which profoundly influence attenuation: (1) Temperature has been shown from multiple studies and laboratory experiments to have a strong anti-correlation with attenuation (Faul and Jackson (2005), (Anderson, 1967), Dalton et al. (2009), Romanowicz and Mitchell (2015)). (2) Partial melt influences attenuation but not as strongly as temperature and both the magnitude and sign of the effect is dependent on the melt mechanism. A melt-squirt mechanism reduces seismic velocities without affecting attenuation. Hammond and Humphreys (2000) measured this affect using a combined laboratory and numerical modelling method. In contrast, a grain-boundary sliding mechanism will cause a significant increase in attenuation Faul et al. (2004). (3) Water content has been shown to strongly increase attenuation (Karato and Jung, 1998).

Previous research has consistently found that temperature anomalies provide the first order control on mantle attenuation structure (Romanowicz and Mitchell (2015), Dalton et al. (2008), Revenaugh and Jordan (1991a)). To investigate the effect of temperature anomalies on our results we compared attenuation to travel time measurements (Figures 13 and 14). Higher temperatures result in lower shear wave velocity and as such travel time between the ScS and ScSScS phases should be greater in regions of higher temperature. To allow comparison between event-station pairs with different epicentral distances the difference between the measured travel time and that predicted by the AK135 travel time model (Kennett et al., 1995) is determined. This means positive values represent lower V_s-higher temperature and negative values higher V_s-lower temperature structure. Plotting this travel-time difference against the measured attenuation provides Figure 14. From Figure 14 no clear correlation can be seen. Perhaps the most striking observation is that Fiji (Station MSVF) is a very slow region with a $t_r = 5-10s$ slower than predicted by the AK135 model, yet with average or just above average attenuation. Japan on the other hand has the largest range of attenuation with an average or fast velocity. This lack of correlation between travel time and attenuation was also found by Kanamori and Rivera (2015).

The lack of correlation may be understood when considering the affects of slow and fast regions on travel times. A slow region in the mantle will result in a delayed arrival but if there is an equally fast region then the result will have no overall affect on the travel time. This is not the case with attenuation: once energy is lost in a high attenuating region then it cannot be regained in a low attenuating region. Thus regions can show high attenuation but normal travel times. In other words: The travel time represents whole mantle velocity structure while our attenuation measurements are strongly influenced by high attenuation regions only.

To take this difference into account we collect values of shear wave velocity perturbation from the S20RTS tomographic model (Ritsema and van Heijst, 2000). If we assume that our measured values of attenuation are dominated by the strongly attenuating regions in the mantle we can use the tomographic models to determine the velocity perturbation in these regions (assuming the strongly attenuating regions correspond to regions of strong velocity perturbation). To explain further we shall look at three regions in detail with tomographic models and from these measure the velocity perturbation from the strongest anomalous region.

3.3 Regional Studies: Japan

Japan is an interesting region to study attenuation as it has formed due to subduction zone volcanism and this can result in high temperature variations, volatiles and partial melt affecting attenuation measurements. Figure 15 shows the measured values of $1/Q$ around Japan.

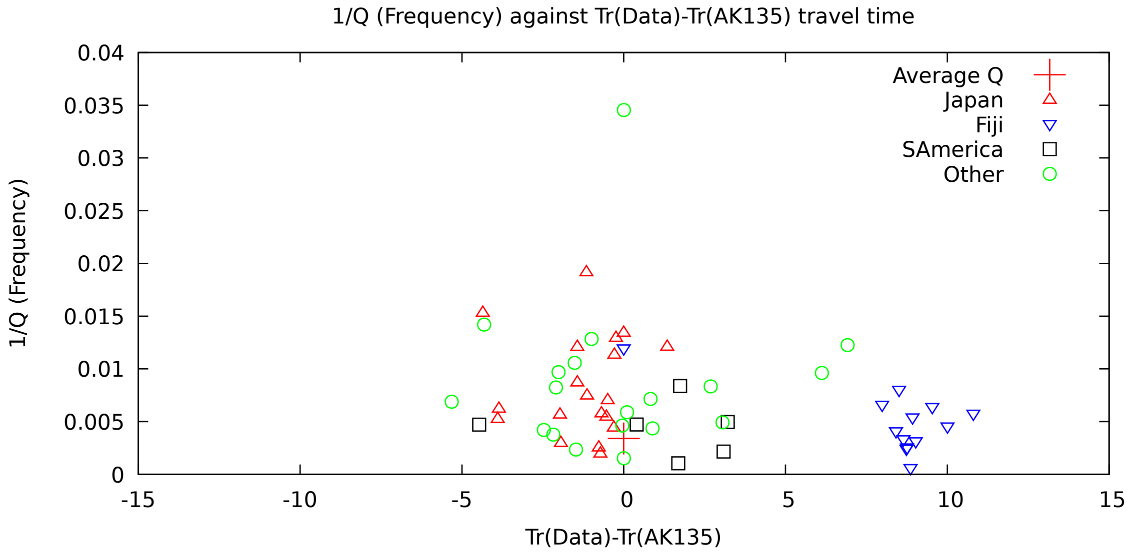

Figure 14: Values of 1/Q (frequency) compared to travel time difference between ScSScS and ScS. To take into account different epicentral distances the travel time difference is calculated as the measured value minus the value from the AK135 travel time models. Thus positive values occur in regions of lower shear wave velocity and negative values in regions of higher shear wave velocity. Red cross shows location of mantle average attenuation and travel time.

It can be seen that attenuation is mostly higher than mantle average ($Q = 220, q = 0.005$) but that there is no clear geographic pattern and that there are large variations over small distances. The average attenuation, q for station ERM is 0.01, while for station MAJO it is 0.008. Comparison to travel time differences shown in Figure 16 do not reveal an obvious correlation.

To try and identify specific regions of high attenuation under Japan and to more reliably recognise regions of temperature anomaly we analyse shear wave velocity perturbations underneath Japan from the S20RTS tomographic model (Ritsema and van Heijst, 2000). Figure 17 shows that Japan has a faster region to the south and a slower region to the north between 50-100km depth. The magnitude of this difference is large with $dVs = -2.4ms^{-1}$ in the north around station ERM and no significant negative velocity perturbation in the south near station MAJO. To a first order this is consistent with our predictions: a strong negative velocity anomaly corresponds to higher attenuation.

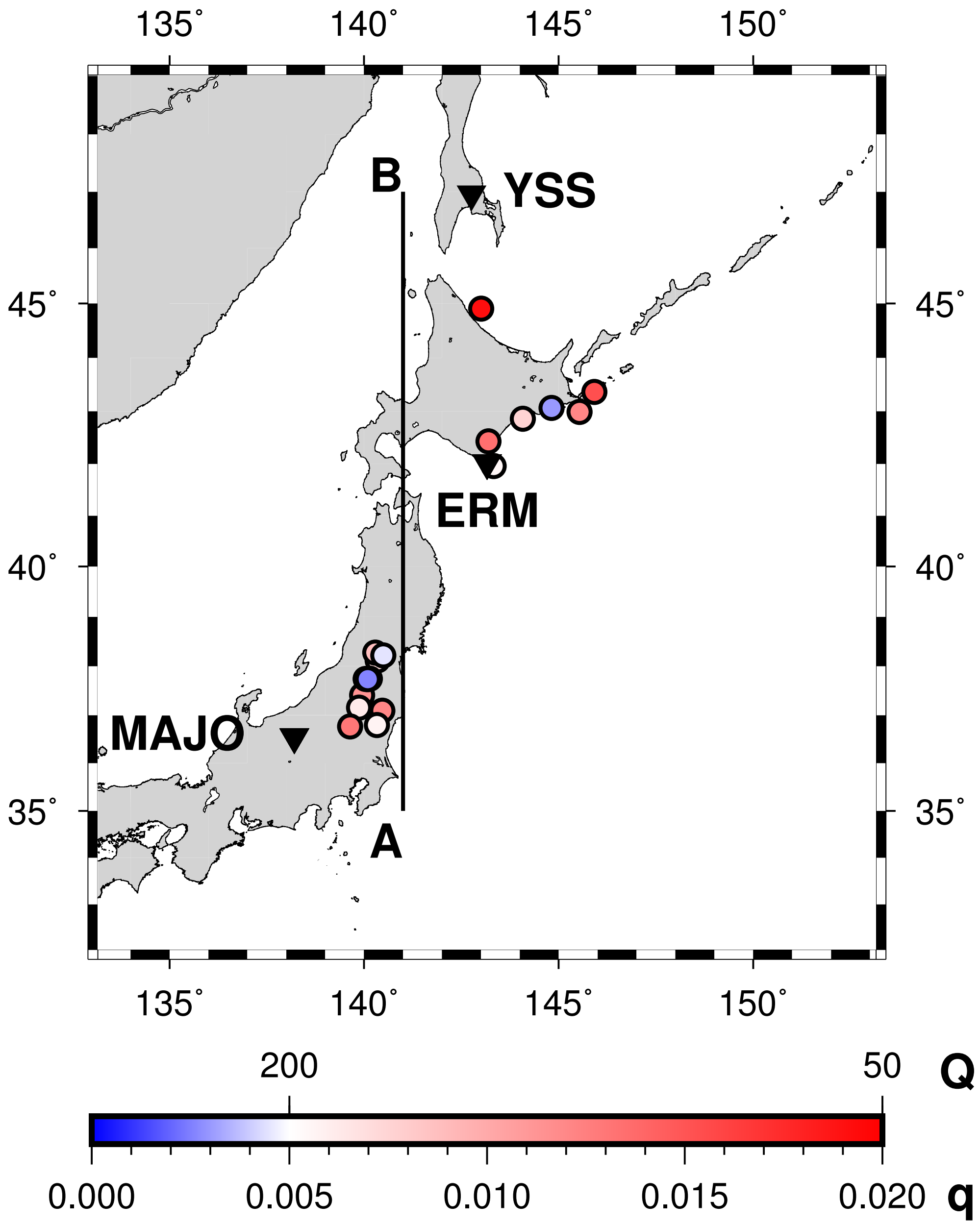

Figure 15: Measurements of Attenuation for Japan. black triangles are stations where earthquakes were recorded. Circles represent the Q-values with the locations being the midpoint between station and Earthquake. Black line shows the direction of tomographic cross section in Figure 17.

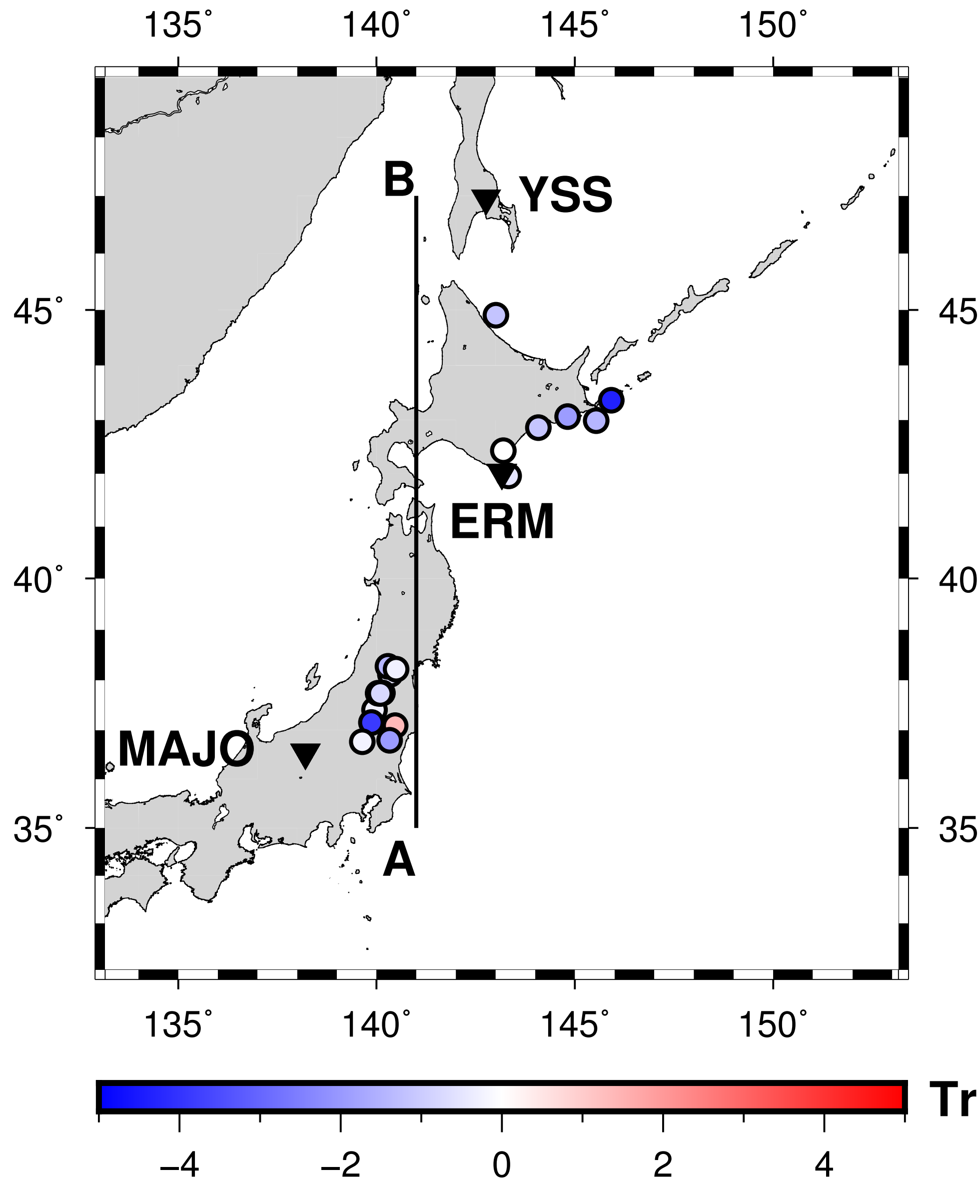

Figure 16: Travel time anomalies between ScS and ScSScS relative to AK135 for the Japan region. To take into account different epicentral distances t_r is calculated as the the measured value minus the value from the AK135 travel time models. Thus positive values occur in regions of lower shear wave velocity and negative values in regions of higher shear wave velocity. Black triangles show location of stations and the black line shows the direction of tomographic cross section in Figure 17.

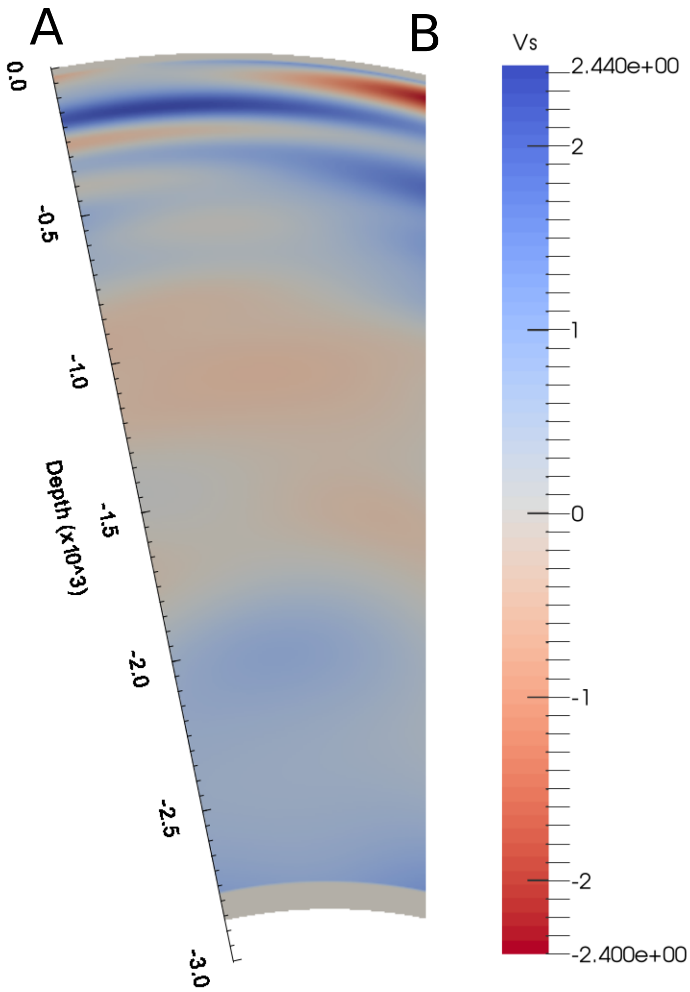

Figure 17: S20RTS Tomogrpahic model underneath Japan from 35°N to 47°N at longitude 141°E down to 3000km depth showing shear wave velocity perturbations. (Ritsema and van Heijst, 2000).

3.4 Regional Studies: Fiji

Fiji sits in the back-arc of a subduction zone consisting of many volcanic islands. Potentially attenuation could be effected much more by volcanism and partial melting compared to Japan due to a higher density of volcanoes (indicative of large volumes of partial melt). Furthermore, a large amount of data from Fiji proved excellent for ScS investigations of attenuation structure. Figure 18 shows our attenuation measurements. The average measured attenuation from Fiji is $q = 0.005$, or nearly precisely mantle average for Q_{ScS} ($Q \geq 220, q \leq 0.0045$). This is in contrast to Japan, while Japan is located relatively close to the subduction zone that formed it, Fiji is located in the backarc. When analysing the tomographic model beneath Fiji (Figure 20) It can be seen that Fiji has an overall positive shear wave velocity with a very strong negative shear wave velocity ($dVs = -6ms^{-1}$) region near the surface (50-100km). If this negative anomaly was due to temperature than we would expect much higher absolute values of attenuation.

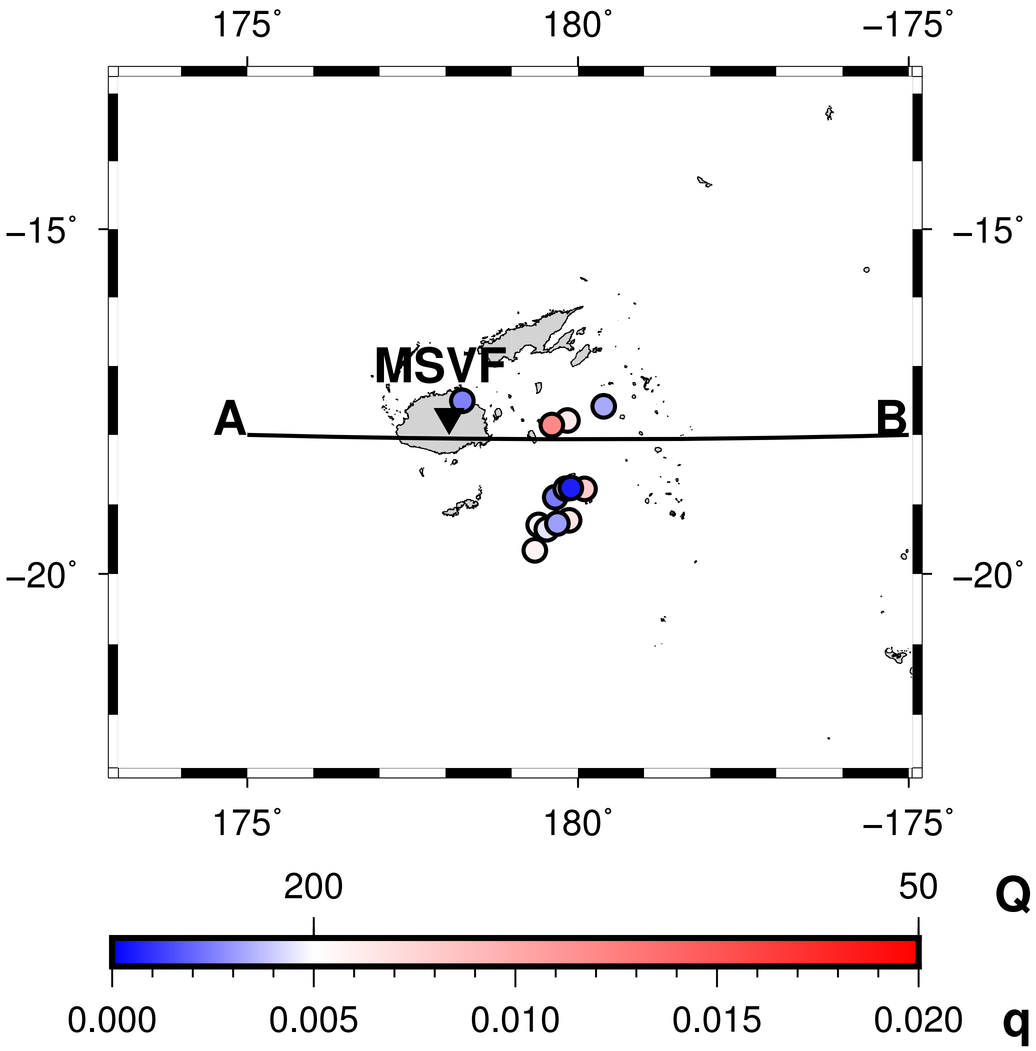

Figure 18: Measurements of attenuation for the Fiji region. Black triangle is location of station MSVF and the black line shows the alignment of the tomographic cross section shown in Figure 20.

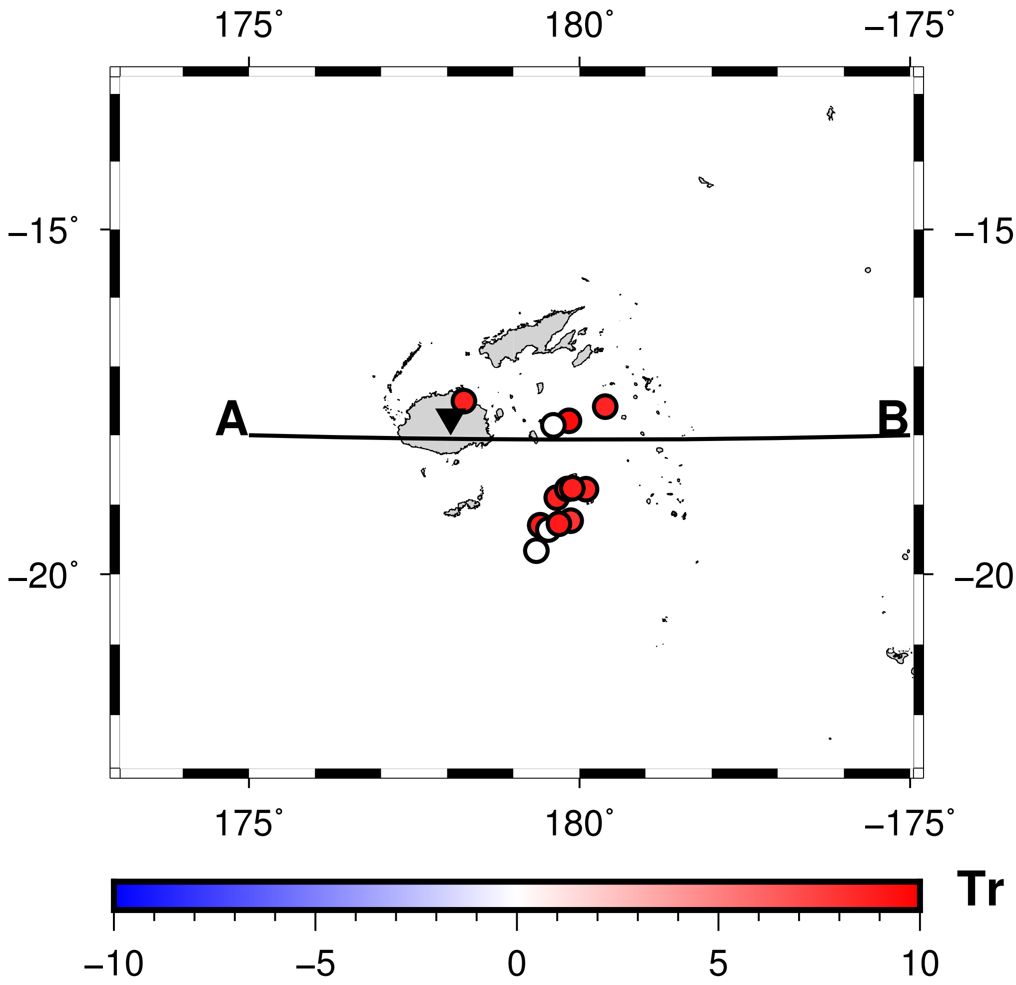

Figure 19: Travel time anomalies between ScS and ScSScS relative to AK135 for Fiji. To take into account different epicentral distances t_r is calculated as the the measured value minus the value from the AK135 travel time models. Thus positive values occur in regions of lower shear wave velocity and negative values in regions of higher shear wave velocity. Black triangles show location of stations and the black line shows the direction of tomographic cross section in Figure 20.

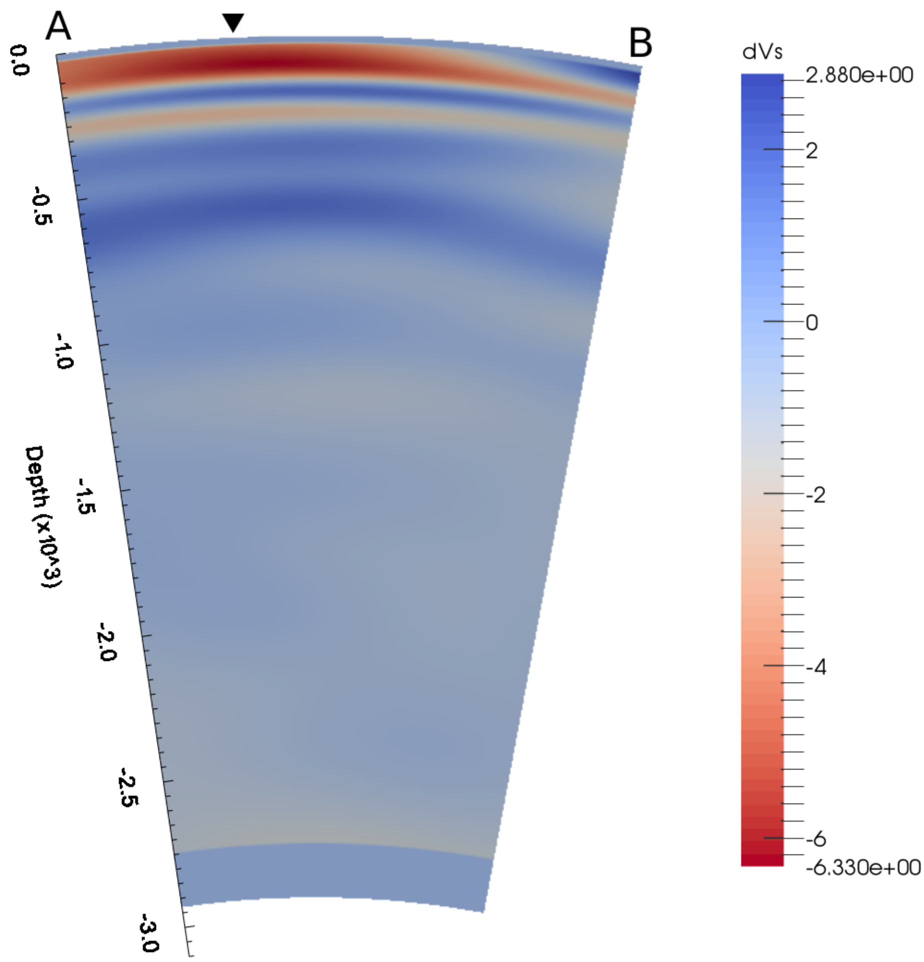

Figure 20: S20RTS Tomogrpahic model of Fiji from 175°E to 185°E at latitude -18° down to 3000km depth showing shear wave velocity perturbations. (Ritsema and van Heijst, 2000).

3.5 Regional Studies: South America

South America is also a subduction zone but unlike Japan and Fiji the over-riding plate is continental crust. This made many event-station pairs noisey in comparison to data from other regions due to increased scattering from a thicker crust. However there were still 6 event-station pairs across 5 stations over a large region which produced clean data (see Figures 21 and 22).

There is no direct correlation between travel time and attenuation (Figures 14 and 13) but there is something of a correlation when comparing the attenuation map to the tomographic models shown on Figure 23. It is clear to see that the northern region contains more regions of slow velocity than the southern and the southern region corresponds to the lowest attenuation. Between 100-200km in the southern region the shear wave velocity perturbation is $dVs = +2ms^{-1}$, while in the north there is a negative velocity perturbation of $dVs = -1ms^{-1}$ at 250km. The average attenuation for the stations in the North (NNA, OTAV, BCIP and JTS) is $q = 0.006$ which is slightly higher than mantle average. Average attenuation to the south (station LVC) is $q = 0.002$, which is lower than mantle average. To a first order the observations can be explained by temperature anomalies: To the North a strongly attenuating region corresponds to a negative velocity anomaly while in the South weak attenuation is observed along with a positive velocity anomaly.

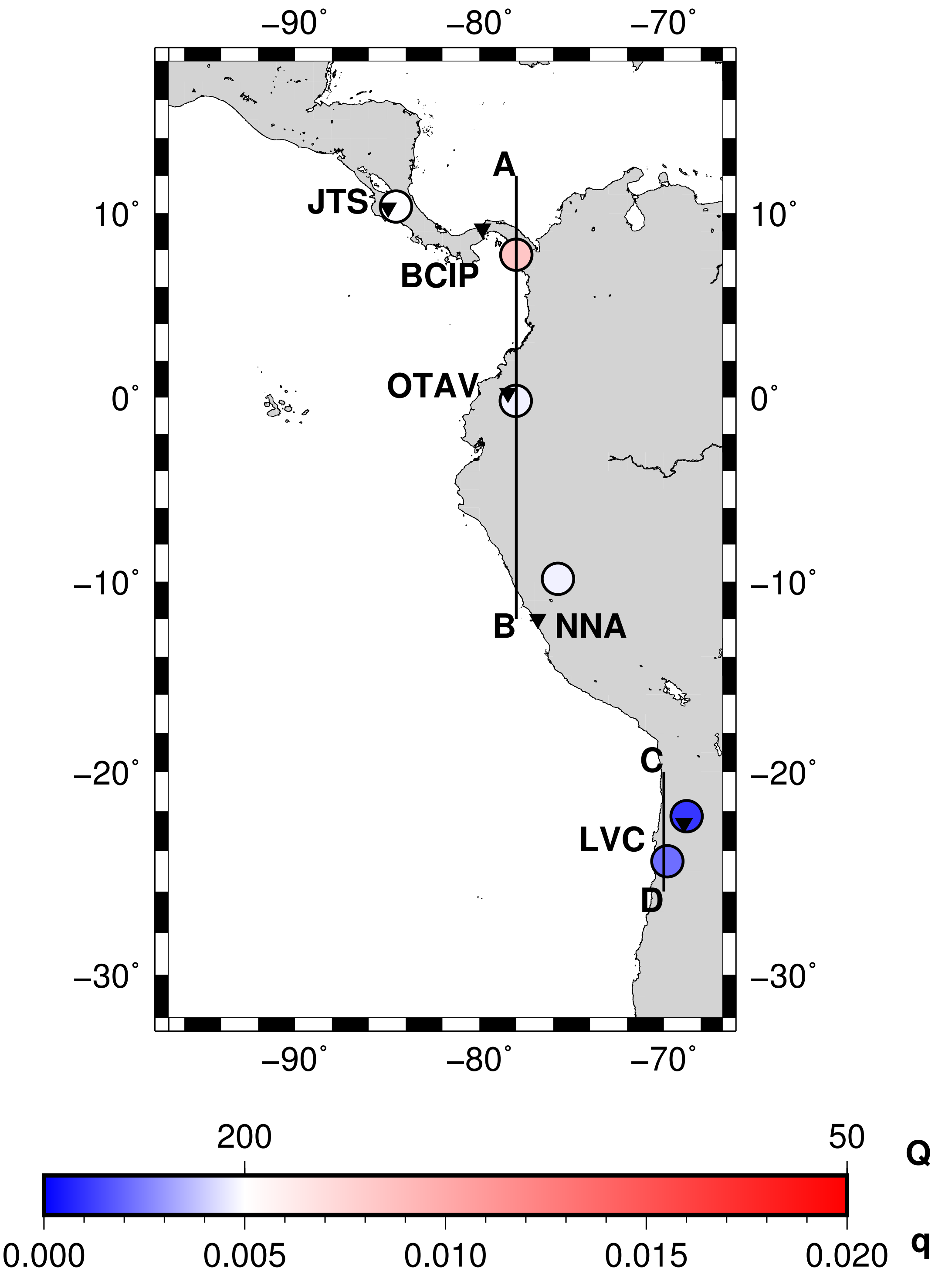

Figure 21: Measurements of attenuation for South America region. Black triangles show location of stations and the black lines shows the alignment of two tomographic cross sections shown in Figure 23.

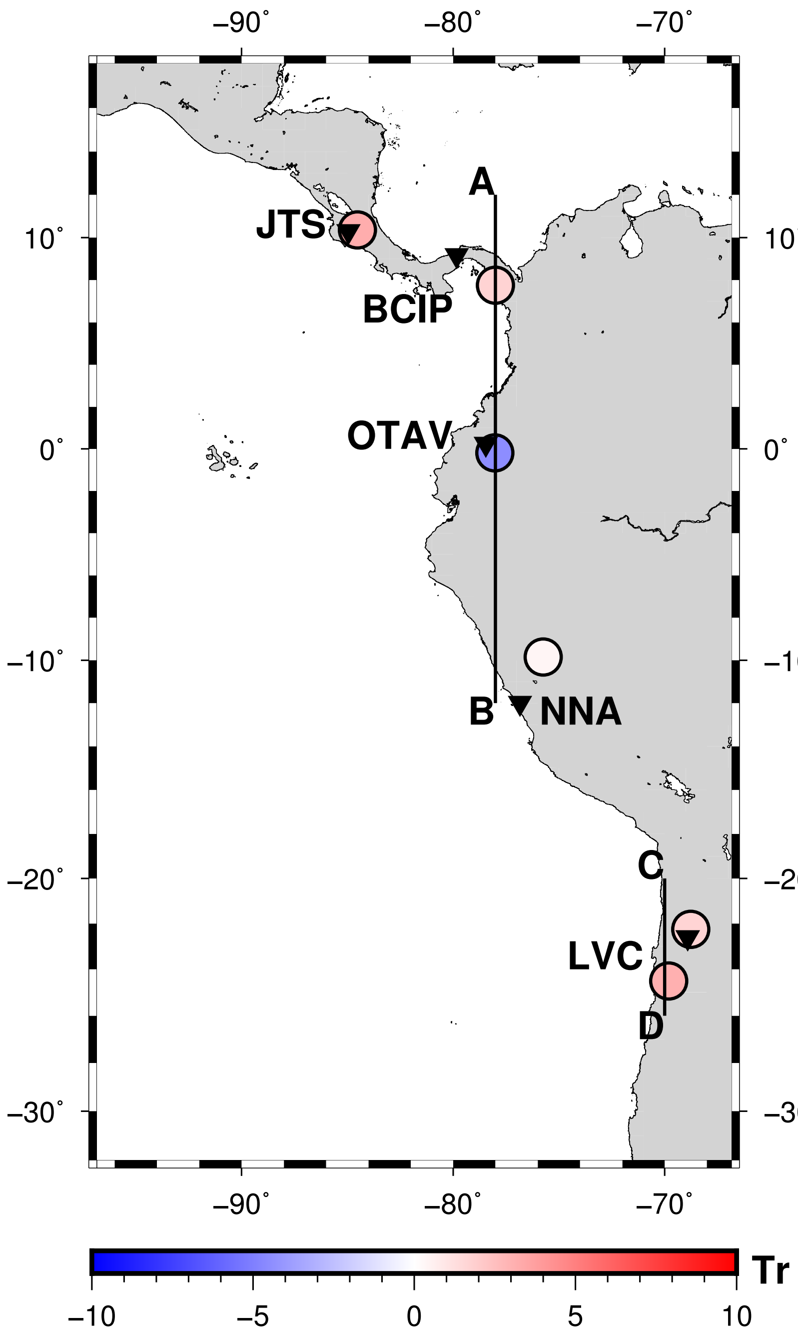

Figure 22: Travel time anomalies between ScS and ScSScS relative to AK135 for South America. To take into account different epicentral distances t_r is calculated as the the measured value minus the value from the AK135 travel time models. Thus positive values occur in regions of lower shear wave velocity and negative values in regions of higher shear wave velocity. Black triangles show location of stations and the black lines shows the alignment of two tomographic cross sections shown in Figure 23.

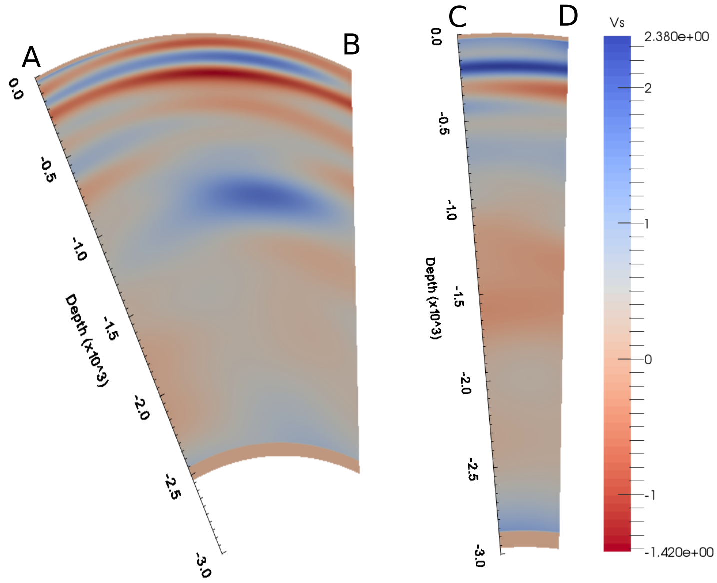

Figure 23: S20RTS Tomogrpahic models of South America. A-B is at longitude -78, with latitudes -12 to 12 and down to 3000km depth while C-D is at longitude -70 with latitudes -20 to -26 also down to 3000km. Both are showing shear wave velocity perturbations. (Ritsema and van Heijst, 2000).

3.6 Comparison to Laboratory Experiments

We can compare measured attenuation and shear wave velocity perturbations for the upper mantle to empirically derived relations between attenuation, temperature, water and partial melt. However to allow comparision we must calculate the difference in our measured attenuation against mantle average, $dq = q_{measured} - 0.005$, and plot this difference against values of shear wave velocity perturbation which results in Figure 24. For the regions of Fiji, Japan and South America values of average attenuation and attenuation difference (dq) and velocity perturbation are provided in Table 1. Looking at Figure 24 there is no clear correlation between attenuation and shear-wave velocity/temperature. This means that our attenuation observations cannot be explained purely by temperature anomalies, but must require mechanisms such as partial melting and water to account for our observations.

Station(s)	Region	dVs (0-200km)	Average q	dq
MSVF	Fiji	-6.0	0.005	0
ERM	Japan	-2.0	0.010	0.005
MAJO	Japan	0.0	0.008	0.003
JTS-BCIP-OTAV-NNA	NSAmerica	-1.5	0.006	0.001
LVC	SSamerica	2.0	0.002	-0.003

Table 1: Comparison of average attenuation anomaly (relative to mantle average) and shear wave velocity perturbation between 0-200km depth for regions with large amounts of data.

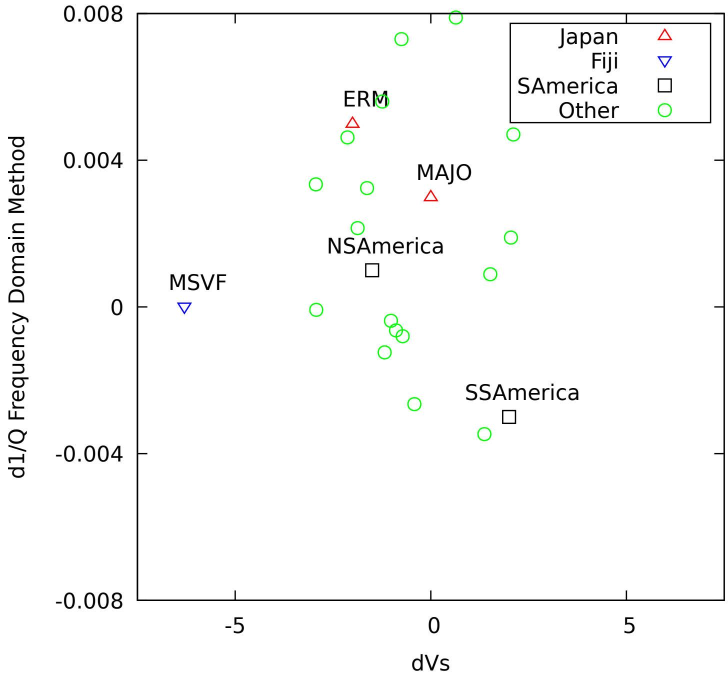

Figure 24: Comparison between shear-wave velocity perturbations and attenuation relative to mantle average. For data in South America, Japan and Fiji the shear wave velocity perturbation comes from the top 200km and corresponds to the strongest anomaly. Furthermore in these regions the attenuation is averaged attenuation across many values. For other data individual attenuation measurements were used and the the velocity purturbation at 150km depth underneath the mid-point between source and reciever was used.

In the last two decades there has been an increase in the measurements of attenuation and velocity in high pressure-temperature experiments in labs. This has allowed empirical relations to be derived between attenuation and velocity relative to temperature (Faul and Jackson, 2005), water (Karato and Jung, 1998) and partial melting through a melt squirt mechanism (Hammond and Humphreys, 2000) and through grain boundary sliding (Jackson et al. (2004), Faul et al. (2004)). It is important to make a clear distinction between these two partial melt mechanisms as they affect attenuation measurements differently. Dalton et al. (2009) combined the above derived relationships to interpret a global attenuation model (based on surface waves) and produced Figure 25. Dalton et al. (2009) also makes particular use of measurements from Faul and Jackson (2005) who find that there is high sensitivity to temperature variations in dry, melt free olivine. From this Faul and Jackson (2005) conclude that most attenuation perturbations that we observe can be accounted for by temperature anomalies.

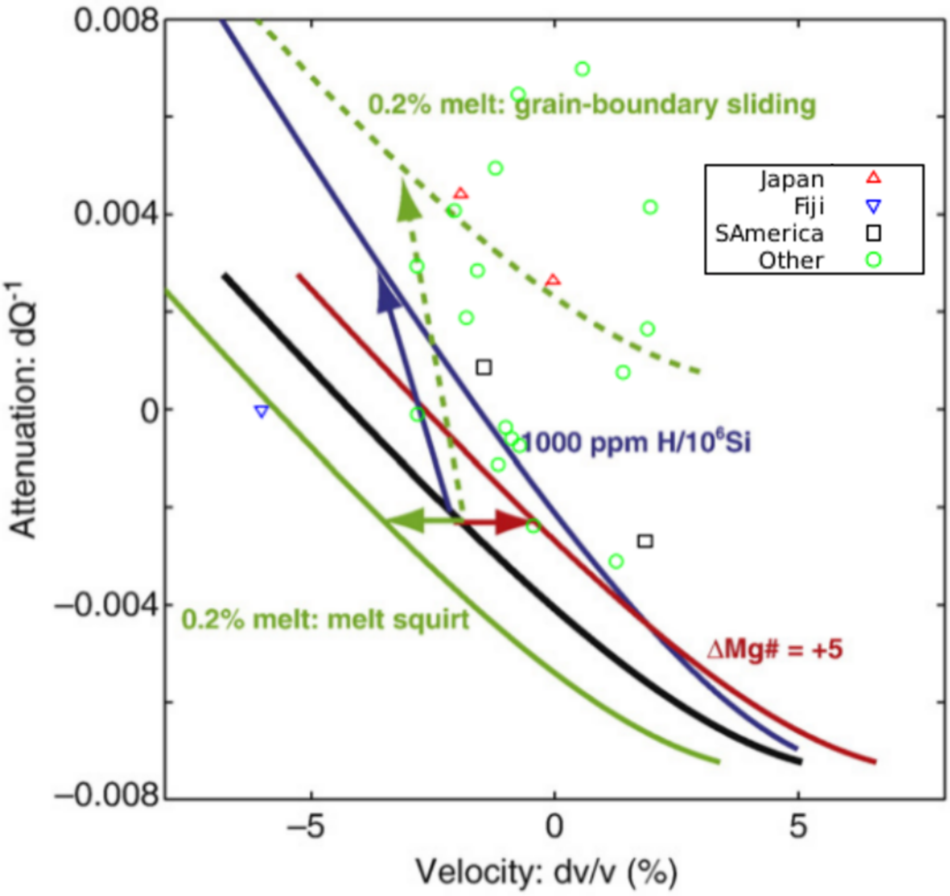

Figure 25: Figure 1 from Dalton et al. (2009) adapted with our results plotted. the lines show the relationships between attenuation, tempreature, water content and partial melt with measured values of 1/Q (frequency) and shear wave velocity perturbations collected from the S20RTS tomographic model. Measured values of 1/Q (frequency) are relative to mantle average: $1/Q = 0.005$ and shear wave velocity perturbations collected from the S20RTS tomographic model (Ritsema and van Heijst, 2000) are at the location between the station and source at 150km depth (with exception of Fiji which has a much stronger negative anomaly at 100km depth). Attenuation values for stations ERM(Japan) ,MAJO (Japan), MSVF (Fiji) and the stations in Northern-South America and Southern-South America are averaged due to the high density of results in these regions. Red-triangles: Japan, Black-squares: South America, Blue triangle: Fiji.

It was possible to plot our results from Figure 24 on top of the figure produced by Dalton et al. (2009), which can be seen as the symbols on Figure 25. This allows us to more quantitatively interpret our results, for example, it can be seen that when combining Fiji's attenuation measurements with its velocity anomaly a 0.2% partial melt squirt mechanism best explains the data. Japan on the other hand shows a gradient between the northern (more attenuating region) and the southern (less attenuating region). From Figure 25 it can be seen that the gradient can be explained by the temperature anomalies but the higher absolute values of attenuation are best explained by a 0.2% grain boundary sliding partial melt mechanism. Finally South America is found to be more anomalous: like Japan there is a gradient of lower attenuation from North to South, which can be explained by the temperature differences, but that the absolute values are being increased by other mechanisms, potentially water content, or grain boundary sliding partial melt: or perhaps a combination? These are cautious interpretations of our results but show how a combined method of seismic observations with experimentally derived relations might be able to distinguish between different properties in the Earth.

3.7 Synthetics and the Effect of Focussing and Defocussing

Synthetic seismograms provide an insight into the effects of focussing and de-focussing on attenuation calculations. The synthetic seismograms are collected simultaneously with the data and are produced using the *SPECFEM3D* by Tromp et al. (2010). The synthetics use the 3D tomographic mantle model S362ANI (Kustowski et al., 2008) and take only radial attenuation into account by using values derived by Durek and Ekström (1996). Durek and Ekström (1996) find that shear wave $Q = 220 \pm 20$ for the whole mantle and no 3D variations in Q. This makes the synthetics perfect to compare to our results as any deviation of Q measured from synthetic seismograms from this whole mantle average value must be due to the effects of 3D velocity structure, i.e. focussing and de-focusing.

Figure 26a compares t_r between data and synthetics. The synthetics and the data are comparable (approximately) when there is a fast arrival (relative to AK135), however, the data on average arrives later than the synthetics in slow regions. This suggests that synthetic seismograms are less accurate at modelling slow regions.

Figure 26b compares the attenuation values of synthetic seismograms and data. It is seen that in regions of low attenuation the synthetics and data are comparable but in highly attenuating regions the synthetics under estimate the data's attenuation. Finally to see if a link between the two can be established Figure 27 is provided. This shows the difference in Tr and attenuation between synthetics and data. More results are needed to confirm this, but it seems to show that the regions where attenuation in the data is higher than in the synthetics are the same regions which have slow arrivals in the data.

Comparing attenuation measured from synthetics and that from data provides insight into the effects of focussing caused by velocity structure. When attenuation measured from synthetics deviate from $Q = 220, 1/Q = 0.0045$ then it is due to modelled velocity structure. When the data and synthetics have similar values of attenuation and do not have values of: $Q = 220, 1/Q = 0.0045$, suggests that what appears to be attenuation measured from the data is at least partly apparent attenuation influenced by focussing. It also shows that strongly attenuating regions are not as effected by focussing as weakly attenuating ones. Quantifying this effect is one of the major challenges in mantle attenuation studies.

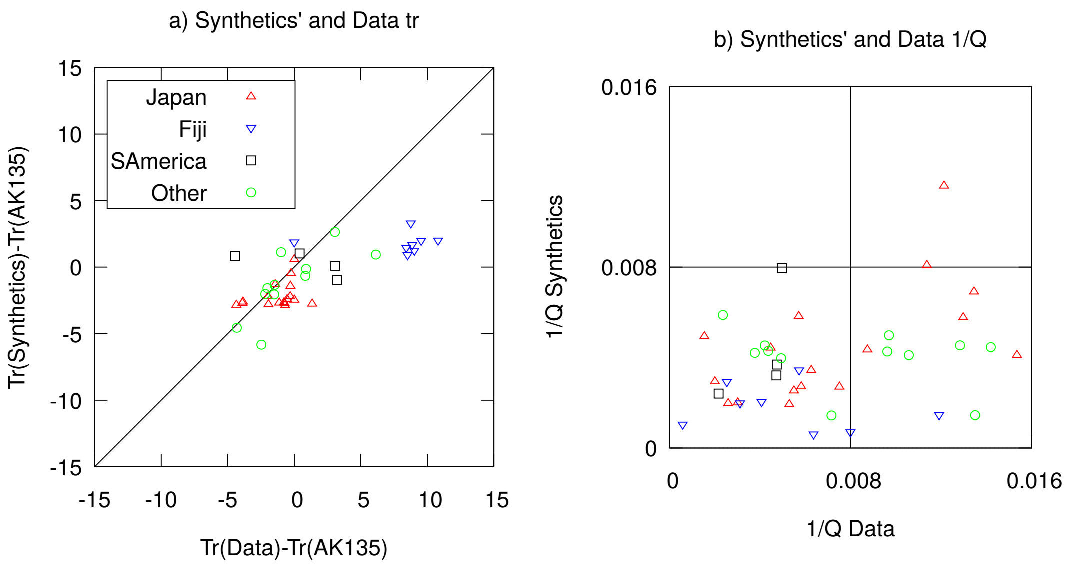

Figure 26: a) Comparison of the measured travel times from synthetic seismograms and data. Travel time takes into account epicentral distances b) Comparison of the attenuation (frequency) between synthetic seismograms and data.

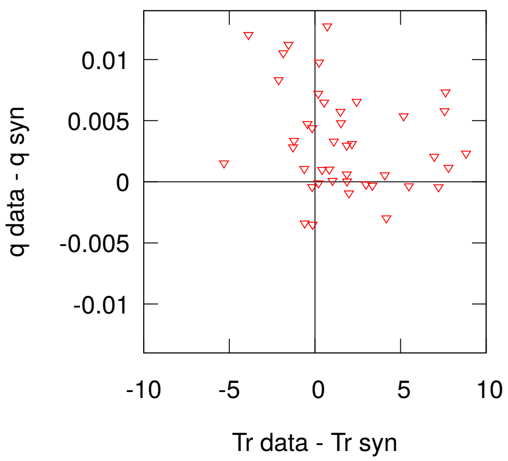

Figure 27: Comparison of the difference between attenuation measured between synthetics and data to the difference in travel time between synthetics and data.

3.8 sScS and 650 Reverberations

There are a range of other horizontally polarised shear wave reverberations which can also be seen in our data. The sScS and sScSScS phases occur when there is an initial reflection from the Earth's surface, the raypath is shown in Figure 28. If the depth of an earthquake is 500km or greater then the sScS and sScSScS phases can be clearly distinguished on a seismogram from the ScS and ScSScS phases as shown in Figure 29. An event depth of 500km equates to a time difference of approximately 300s on our seismograms.

We found that of our 59 event station pairs 9 also had clear sScS arrivals from which we could measure a reliable value of attenuation. Conducting the same frequency domain attenuation calculations on event-station pairs which show clear sScS and sScSScS phases we find that the attenuation value tends to be slightly higher than the ScS phases. While the dataset must be much larger to draw reliable conclusions we find that of the 9 event station pairs 6 show an increased attenuation in the sScS phase compared to ScS. Taking the same data as used in Figure 29 as an example we find that Q is 390 for the ScS-ScSScS phases and 365 for the sScS-sScSScS phases. The simplest explaination for this difference is that the sScS phases sample the upper mantle more than the lower mantle (relative to the ScS phases) and as such have sampled higher attenuating material more. Results are found in Appendix Table A3.

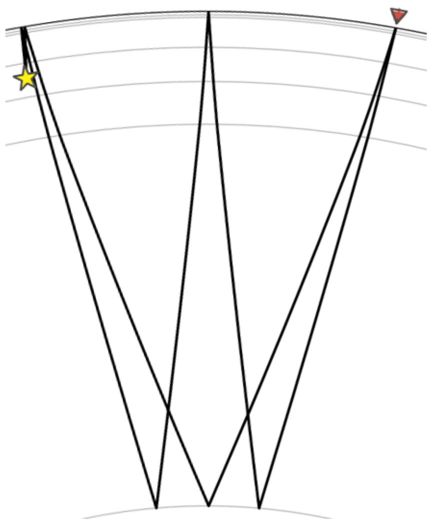

Figure 28: The paths taken by sScS and sScSScS phases, epicentral distance has been exagerated to $\theta = 20°$ for clarity. Figure Generated using ObsPy and Taup.

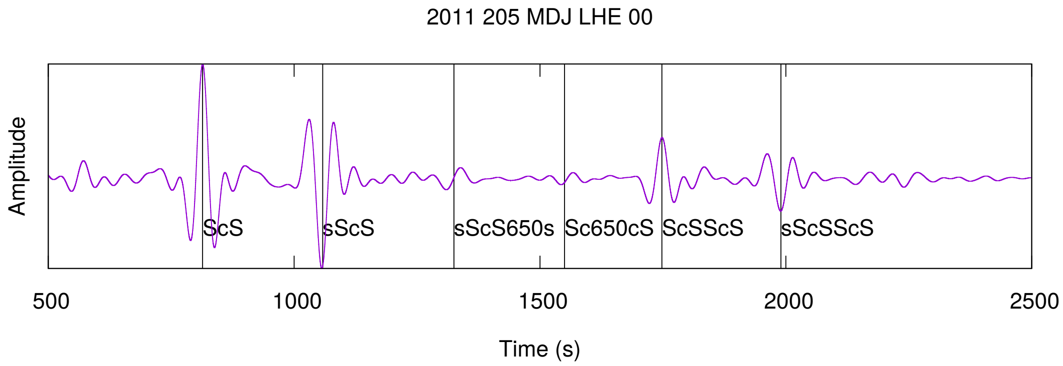

Figure 29: The shear wave phases sScS and sScSScS, along with the ScS and ScSScS phases and the Sc650cS precursor. Data comes from station: MDJ, year: 2013, julian day: 95, instrument: 00, component: LH2/East.

There are also ScS phases which reflect off the mantle transition zone discontinuities. In Figure 30 we can see the path taken by the S650ScS and S650ScSScS phases. The arrivals of these phases can be seen on Figure 31. It can be seen that the S650ScS arrival has a much lower amplitude than the ScS and ScSScS phases. This is due to the low reflection coefficient (R) of the 650km boundary. For ScS and ScSScS it was a reasonable assumption to say that R is -1 as the CMB and Surface represent solid-liquid phase changes. This means that all the seismic energy is reflected from the CMB and surface, however the 650km boundary is a phase transition in olivine (Liu, 1979) and thus has a lower reflection coefficient. This can be seen from the S650ScSScS phase which does not have an amplitude much greater than background noise. Despite this we were abe to measure attenuation values for 7 event-station pairs for the S650ScS phases. Looking at Appendix Table A5 it can be seen that attenuation is between 2 and 8 times greater for the S650ScS phases than the ScS. This could partly be due to the increased sampling of the upper mantle but is more likely to be due to the low reflection coefficient of the 650km boundary.

A Sc650cS phase was also identified on a 2 seismograms as shown in Figure 31. This is a phase which reflects from the underside of the 650km boundary (Figure 32). While there was not enough time to fully investigate the Sc650cS phase future research might be able to investigate the reflectivity properties of the 650km phase transition using this precursor and from this better constrain lower mantle attenuation.

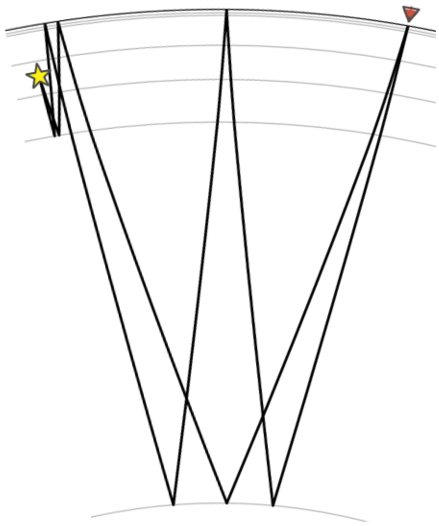

Figure 30: The paths taken by S650ScS and S650ScSScS, epicentral distance has been exagerated to $\theta = 20°$ for clarity. Figure Generated using ObsPy and Taup.

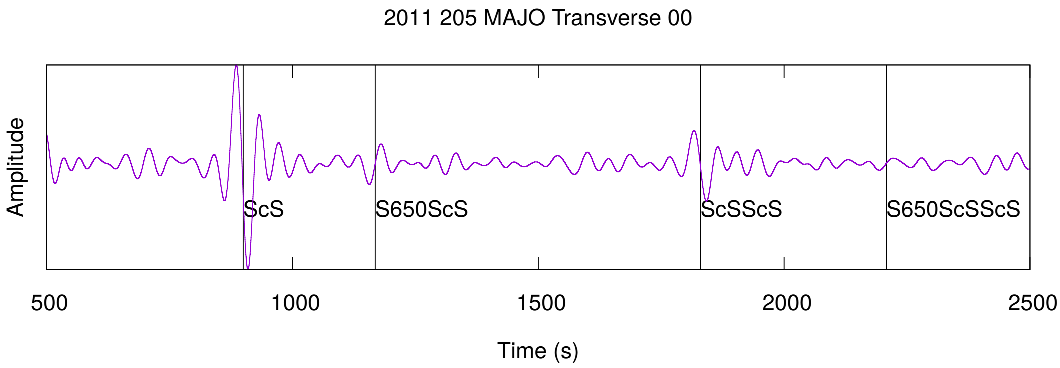

Figure 31: The shear wave phases S650ScS and S650ScSScS, along with the ScS and ScSScS phases. Data comes from station: MAJO, year: 2011, julian day: 205, instrument: 00, component: Transverse.

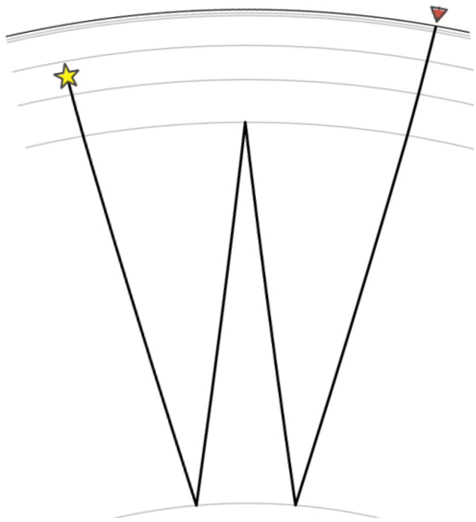

Figure 32: The paths taken by the Sc650cS precursor, epicentral distance has been exagerated to $\theta = 20°$ for clarity. Figure Generated using ObsPy and Taup.

4 Discussion

We have looked at the relationship between travel time and attenuation, compared the measurements of attenuation between real data and synthetic seismograms and looked in detail at specific regions. However it is important to question the reliability of these results and discuss the results as a whole. The following section will discuss: (1) The possibility of relating anomalies in the measured geometrical spreading to focussing and de-focussing. (2) An explaination of the assumptions and identification of systematic errors in this research. (3) Interpret the results as a whole and attempt to identify possible connections between our results and properties such as volatile content, temperature and partial melting.

4.1 Geometrical Spreading

Looking at Equation 6 it can be seen that G (Geometrical spreading factor) can be measured from the y-intercept which is equal to $-ln(G)$

Comparing G to the analytical geometrical spreading factor given by Equation 3 an interesting difference was observed: Data which passed the selection criteria showed the two values could vary by ± 0.6. Furthermore, when comparing these values to the $1/Q$ calculated (Figure 33) there seems to be a correlation towards higher geometrical spreading factor (ie. less spreading) and higher attenuation. This is perplexing: why does the measured Geometrical spreading and that predicted analytically differ so much? And why does there seem to be correlation between less energy loss from geometrical spreading and increased attenuation? The difference between measured and analyitcal geometrical spreading could once again be

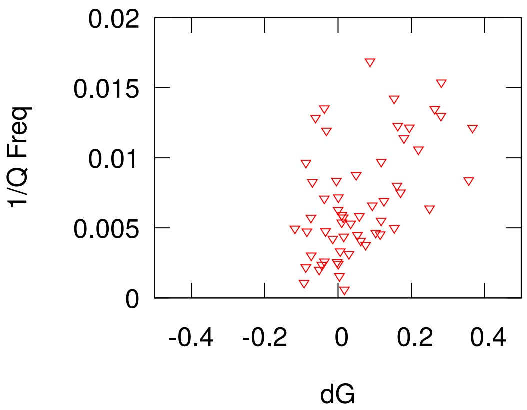

Figure 33: 1/Q compared to dG, difference between Geometrical spreading in the data and that calculated analytically.

caused by the focusing and de-focusing problem. If energy from both ScS and ScSScS is de-focussed on to a particular seismogram by velocity structure it could appear that geometrical spreading was higher. Focussing seems to be a key source of error and one which could account for the large discrepencies seen between results.

4.2 Assumptions

Calculating attenuation from body waves is notoriously difficult and it has been shown in previous studies that there are systematic errors (Romanowicz and Mitchell, 2015). To counter these systematic errors and produce reliable results I conduct a tough data-selection method combined with a more reliable frequency domain approach to attenuation calculation.

The largest errors in body wave attenuation calculations are thought to be from noise, focussing and de-focussing effects. As stated before focussing is a major unknown when attempting to measure attenuation. It is known that energy can be transferred from different regions by velocity structure but it is also impossible to measure how much is focussed from a single seismogram. This could explain why 22 event-station pairs appeared to produce "negative attenuation values" ie. the higher frequencies of the ScS and ScSScS reverberations attenuated less than the lower frequencies. This is counter to the understanding that attenuation is frequency dependent, but if energy was focused in the area of the seismometer then it could appear that energy had not attenuated. We have attempted to measure the extent of focussing in regions by comparing our attenuation results to those measured from synthetics. In effect this allows us to identify regions where known velocity structure results in focussing and to say that higher attenuating regions appear to not be effected by focussing. However this does not account for unknown velocity structure and is at best a guess at the effects of focussing on our data.

It is assumed that the ScS and ScSScS travel the same path through the mantle and sample the same attenuation structure. As can be seen on figure 1 for these small epicentral distances the assumption is valid. Furthermore, it can be shown from looking at sScS and sScSScS arrivals phases (Raypath shown by Figure 28) that the Q values remain approximately the same despite a change in ray path.

It is also assumed that seismic energy is perfectly reflected off the surface and CMB. Reflectivity is a measure of the amount of energy reflected and as the surface and CMB are changes in state (from sold to liquid) then the reflectivity should be close to 1. However, if this is not the case then attenuation may seem higher due to energy loss from imperfect reflections. Furthermore, measurements from phases from the 650km discontinuity are likely to appear much more attenuated due to the much lower reflectivity coefficient.

Finally, looking at Figure 14 it can be seen that the majority of our results are more attenuating than the mantle average of $Q = 200, q = 0.005$ (Romanowicz and Mitchell, 2015). This might be because of the bias of our data towards regions with volcanic islands and subduction zones, which is due to the low epicentral distance required to ensure the ScS and ScSScS reverberations sample the same volume of mantle. Thus, it is not appropriate to draw conclusions on global mantle attenuation structure from our method.

That concludes the assumptions for the seismic methodology, but there were also assumptions made in the interpretation and use of the experimental relations collected by Dalton et al. (2009). For example our measured attenuation sampled the entire mantle, however, we chose to interpret this measurement along with the strongest velocity anomaly in the upper mantle. Furthermore, due to time constraints only the tomographic models of Fiji, Japan and South America were interpreted in detail, the other attenuation measurements used the velocity perturbation from the S20RTS tomogrpahic model at 150km depth. Further assumptions include the experimental studies, most of these experiments are conducted at lower temperatures and pressures than expected in the mantle on small samples and then results are extrapolated to mantle conditions. This is due to experimental constraints but it does result in uncertainty over the reliability of these derived relations. Furthermore we are interpreting our whole-mantle attenuation measurements with the context of empirical relations derived for mantle olivine at a pressure corresponding to 150km depth.

4.3 Future Research

Due to time constraints a few ideas and potentially interesting topics of study had to be set aside. With more time I would have liked to produce a semi-automatic routine to analyse the strongest velocity anomalies from a tomographic model and pick the most representative velocity of these anomalies to be interpreted alongside the attenuation measurement. This would have made collecting velocities from the tomographic models of South America, Japan and Fiji more efficient and would result in more accurate velocity anomalies for the data that tomographic models were not plotted for.

Furthermore, a future project expanding on this research should look into possible methods to increase the amount of reliable measurements. 84% of viable event-station pairs were disregarded due to pollution of the frequency spectra with other phases, if a method to remove this noise from the data could be developed then potentially their could be a higher pass rate and therefore more interpretable results.

Finally the problem of quantifying focussing and defocussing in the mantle represents a large hurdle for future attenuation research. I propose that use of data from the large US array could lead to a quantification of the affects of focussing in the region. A dense array of seismometers could map out deviations in attenuation and taking into account the geometrical spreading differences it might be possible to quantify the effects of focussing in a specific region. This would provide constraints on the magnitude of the effect of focussing and de focussing. Furthermore with the right approach it might be possible to make a joint velocity and attenuation mode to predict the effect of focussing and then deduct this affect from measurements.

5 CONCLUSION

The method of measuring attenuation using the frequency spectra of ScS reverberations provides valuble insights into regional studies. When compared to mantle tomography it provides a poweful tool to discern effects of temperature, water and partial melt. To investigate the role of temperature we compared the tomographic models of Japan, Fiji and South America (Figures 17, 20 and 23) with their average measured values of attenuation. As discussed before this showed that Japan has on average high attenuation but overall no velocity anomaly (ie. there are equal regions of high and low velocity), Fiji has an overall negative velocity anomaly due to a very slow region in the upper mantle but with average mantle attenuation and South America shows a slower region to the north which corresponds to slightly increased attenuation and a faster region to the south which has lower attenuation.

Bringing the interpretations together in the context of research by Dalton et al. (2009) we can cautiously say the following: South America and Japan show the expected behaviour from temperature dependent attenuation but require the influence of partial melting with a grain boundary mechanism or water to account for the magnitudes of their attenuation. Fiji on the other hand has slow velocities but average attenuation, this leads to the conclusion that partial melt with a melt squirt mechanism is influencing the attenuation measurements around Fiji. The method of using laboratory derived relations between mantle properties along with seismic observations has proven to be a powerful one, however the relationships between attenuation, water, temperature and partial melt requires further study using observations of attenuation in well understood regions to provide benchmarks. Also further laboratory experiments investigating relations between these properties for a wider range of partial melt mechanisms, water content, compositions and conditions must be conducted.

Comparison of our results with synthetic seismograms lead to the conclusion that focussing and defocussing can account for low attenuation ($q < 0.005$, $Q > 200$) regions but fail to accurately model highly attenuating regions. This is key to understanding the effects of focussing and de-focussing causing redistribution of energy and corrupting attenuation calculations as it implies highly attenuating regions are not affected as much by focussing or de-focussing.

6 Aknowledgements

I would like to thank Arwen Deuss for her guidance throughout this research, our enjoyable discussions were always useful when solving a problem or realizing the next step. I'd also like to thank Cedric Thieulot for his help with making the tomographic figures. A final thanks is due to the other master's students in Room 8.16 for all the tea, distractions and brain storming.

REFERENCES

D. L. Anderson. The anelasticity of the mantle. *Geophysical Journal International*, 14(1-4): 135–163, 1967.

C. A. Dalton, G. Ekström, and A. M. Dziewoński. The global attenuation structure of the upper mantle. *Journal of Geophysical Research: Solid Earth*, 113(B9), 2008.

C. A. Dalton, G. Ekström, and A. M. Dziewonski. Global seismological shear velocity and attenuation: A comparison with experimental observations. *Earth and Planetary Science Letters*, 284(1-2):65–75, 2009.

J. J. Durek and G. Ekström. A radial model of anelasticity consistent with long-period surface-wave attenuation. *Bulletin of the Seismological Society of America*, 86(1A):144–158, 1996.

U. H. Faul and I. Jackson. The seismological signature of temperature and grain size variations in the upper mantle. *Earth and Planetary Science Letters*, 234(1-2):119–134, 2005.

U. H. Faul, F. Gerald, D. John, and I. Jackson. Shear wave attenuation and dispersion in melt-bearing olivine polycrystals: 2. Microstructural interpretation and seismological implications. *Journal of Geophysical Research: Solid Earth*, 109(B6), 2004.

W. C. Hammond and E. D. Humphreys. Upper mantle seismic wave velocity: Effects of realistic partial melt geometries. *Journal of Geophysical Research: Solid Earth*, 105(B5):10975–10986, 2000.

I. Jackson, U. H. Faul, F. Gerald, D. John, and B. H. Tan. Shear wave attenuation and dispersion in melt-bearing olivine polycrystals: 1. Specimen fabrication and mechanical testing. *Journal of Geophysical Research: Solid Earth*, 109(B6), 2004.

H. Kanamori and L. Rivera. Near-vertical multiple ScS phases and vertically averaged mantle properties. *Geological Society of America Special Papers*, 514:SPE514–02, 2015.

S.-I. Karato. Mapping water content in the upper mantle. *Inside the subduction factory*, pages 135–152, 2003.

S.-i. Karato and H. Jung. Water, partial melting and the origin of the seismic low velocity and high attenuation zone in the upper mantle. *Earth and Planetary Science Letters*, 157(3-4): 193–207, 1998.

B. Kennett, E. Engdahl, and R. Buland. Constraints on seismic velocities in the Earth from traveltimes. *Geophysical Journal International*, 122(1):108–124, 1995.

R. L. Kovach and D. L. Anderson. Attenuation of shear waves in the upper and lower mantle. *Bulletin of the Seismological Society of America*, 54(6A):1855–1864, 1964.

B. Kustowski, G. Ekström, and A. Dziewoński. Anisotropic shear-wave velocity structure of the Earth's mantle: A global model. *Journal of Geophysical Research: Solid Earth*, 113(B6), 2008.

T. Lay and T. C. Wallace. Multiple ScS travel times and attenuation beneath Mexico and Central America. *Geophysical Research Letters*, 10(4):301–304, 1983.

L.-G. Liu. On the 650-km seismic discontinuity. *Earth and Planetary Science Letters*, 42(2): 202–208, 1979.

J. Revenaugh and T. H. Jordan. Observations of first-order mantle reverberations. *Bulletin of the Seismological Society of America*, 77(5):1704–1717, 1987.

J. Revenaugh and T. H. Jordan. Mantle layering from ScS reverberations: 1. Waveform inversion of zeroth-order reverberations. *Journal of Geophysical Research: Solid Earth*, 96(B12): 19749–19762, 1991a.

J. Revenaugh and T. H. Jordan. Mantle layering from ScS reverberations: 2. The Transition Zone. *Journal of Geophysical Research: Solid Earth*, 96(B12):19763–19780, 1991b.

J. Revenaugh and T. H. Jordan. Mantle layering from ScS reverberations: 3. The Upper Mantle. *Journal of Geophysical Research: Solid Earth*, 96(B12):19781–19810, 1991c.

J. Revenaugh and T. H. Jordan. Mantle layering from ScS reverberations: 2. The Lower Mantle and Core-Mantle Boundary. *Journal of Geophysical Research: Solid Earth*, 96(B12):19811–19824, 1991d.

J. Ritsema and H.-J. van Heijst. Seismic imaging of structural heterogeneity in Earth's mantle: evidence for large-scale mantle flow. *Science Progress (1933-)*, pages 243–259, 2000.

B. Romanowicz and B. Mitchell. 1.25 Deep Earth structure: Q of the Earth from Crust to Core. *Treatise on Geophysics*, pages 789–827, 2015.

S. A. Sipkin and T. H. Jordan. Regional variation of Q ScS. *Bulletin of the Seismological Society of America*, 70(4):1071–1102, 1980.

R. Tonn. The determination of the seismic quality factor Q from VSP data: A comparison of different computational methods. *Geophysical Prospecting*, 39(1):1–27, 1991.

J. Tromp, D. Komatitsch, V. Hjörleifsdóttir, Q. Liu, H. Zhu, D. Peter, E. Bozdag, D. McRitchie, P. Friberg, C. Trabant, et al. Near real-time simulations of global CMT earthquakes. *Geophysical Journal International*, 183(1):381–389, 2010.

7 Appendix

Date	Station	Country	Component	Instrument	Mag. (M_w)	Event Depth (km)	Event Lat	Event Long
24/06/2011	ADK	USA	Transverse	0	6.9	74	52.0900	-171.7700
13/11/2017	BCIP	Panama	LH2	0	0.0	19	9.5147	-84.4865
24/08/2016	CHTO	Thailand	Transverse	10	6.8	82	20.9224	94.5687
08/12/2016	COR	USA	LH1	10	6.5	12	40.4753	-126.1528
23/09/2016	DAV	Phillipines	Transverse	0	6.3	65	6.5717	126.4918
10/01/2017	DAV	Phillipines	Transverse	0	7.3	613	4.4634	122.5750
02/02/2013	ERM	Japan	LH1	0	6.9	105	42.8500	143.2400
20/07/2014	ERM	Japan	Transverse	0	6.3	61	44.6419	148.7838
16/02/2015	ERM	Japan	Transverse	0	6.7	23	39.8558	142.8808
12/05/2015	ERM	Japan	Transverse	0	6.8	35	38.9056	142.0317
07/07/2015	ERM	Japan	LH1	0	6.3	49	43.9097	147.9748
14/01/2016	ERM	Japan	LH2	10	6.7	46	41.9723	142.7810
19/08/2016	HOPE	South Georgia Island	Transverse	10	7.4	10	-55.2793	-31.8740
16/08/2005	INU	Japan	Transverse	N/A	6.5	37	38.2400	142.0500
13/03/2014	INU	Japan	LHE	0	6.3	83	33.6200	131.8200
24/10/2012	JTS	Costa Rica	LH2	0	6.0	22	9.7100	-85.6000
05/12/2016	KAPI	Indonesia	Transverse	0	6.3	526	-7.3158	123.3802
24/10/2017	KAPI	Indonesia	Transverse	10	6.7	549	-7.2364	123.0401
15/10/2006	KIP	USA	Transverse	0	6.7	48	19.8300	-155.9400
20/06/2011	LVC	Chile	Transverse	0	6.0	131	-18.5212	-69.6411
10/10/2017	LVC	Chile	LH1	0	6.3	82	-21.8900	-68.6300
04/07/2010	MAJO	Japan	LH2	10	6.3	30	37.0052	142.4525
14/03/2010	MAJO	Japan	Transverse	0	6.5	40	39.8558	142.8808
12/03/2011	MAJO	Japan	LH1	0	6.5	25	37.5898	142.7512
22/06/2011	MAJO	Japan	Transverse	0	6.7	32	39.6611	142.5792
24/07/2011	MAJO	Japan	Transverse	0	6.3	41	39.9763	142.4621
23/07/2011	MAJO	Japan	Transverse	10	6.3	46	38.9056	142.0317
30/07/2011	MAJO	Japan	LH2	10	6.4	48	37.7839	141.6548

Table A1 continued from previous page

Date	Station	Country	Component	Instrument	Mag. (M_w)	Event Depth (km)	Event Lat	Event Long
07/04/2011	MAJO	Japan	Transverse	10	7.1	53	37.7399	141.5594
17/06/2012	MAJO	Japan	Transverse	0	6.3	47	38.9140	141.9221
11/07/2014	MAJO	Japan	LH2	10	6.6	20	38.9200	142.1500
16/02/2015	MAJO	Japan	Transverse	10	6.7	23	36.9645	141.0774
12/05/2015	MAJO	Japan	Transverse	0	6.8	35	38.2513	141.7296
05/04/2013	MDJ	China	Transverse	10	6.2	572	42.7700	131.0200
17/01/1995	MSVF	Fiji	LH2	0	6.3	623	-17.3987	-177.2828
05/08/1996	MSVF	Fiji	LH1	0	7.3	531	-19.8023	-177.8334
04/10/2002	MSVF	Fiji	LH1	0	6.3	628	-17.8225	-178.3704
17/11/2004	MSVF	Fiji	LH1	0	6.5	592	-20.7195	-178.2906
19/07/2008	MSVF	Fiji	LH2	0	6.4	389	-17.9609	-178.8406
22/11/2009	MSVF	Fiji	LH2	0	6.3	527	-20.8101	-178.6481
09/11/2009	MSVF	Fiji	LH1	0	7.3	591	-17.2674	178.4528
15/09/2011	MSVF	Fiji	LH2	0	7.3	629	-20.0526	-178.7163
01/11/2014	MSVF	Fiji	LH2	10	7.1	435	-19.7819	-178.2443
21/07/2014	MSVF	Fiji	LH1	0	6.9	615	-19.8015	-178.4001
27/05/2016	MSVF	Fiji	LH1	0	6.4	567	-20.8588	-179.2129
24/09/2016	MSVF	Fiji	LH1	0	6.9	596	-20.9802	-178.9677
19/08/2017	MSVF	Fiji	LH1	10	6.4	544	-21.5930	-179.3240
24/08/2011	NNA	Peru	LH1	10	6.8	144	-7.6800	-74.6600
18/05/2016	OTAV	Equador	LH2	10	6.9	30	0.4947	-79.6160
16/11/2012	PET	Russia	Transverse	0	6.5	41	54.2940	162.8129
20/03/2016	PET	Russia	Transverse	0	6.4	30	49.2200	155.8700
30/01/2016	PET	Russia	Transverse	0	7.2	163	54.0057	158.5128
05/03/2014	SANVU	Vanuatu	Transverse	0	6.4	661	-14.6400	169.8000
13/01/2014	SJG	Puerto Rico	Transverse	10	6.3	22	-19.2200	-66.8200
20/01/2014	SNZO	New Zealand	LH1	0	6.2	25	-40.6700	175.8000

Table A1 continued from previous page

Date	Station	Country	Component	Instrument	Mag. (M_w)	Event Depth (km)	Event Lat	Event Long
31/05/2016	TATO	Taiwan	LH2	0	6.4	246	25.5615	122.5458
18/04/2011	URZ	New Zealand	LH2	10	6.2	100	-34.4000	179.8300
02/02/2013	YSS	Japan	LHN	0	6.4	105	42.8500	143.2400

Table A1: Station and Event information: Date, Station Name, Station Country, Component, Instrument, Event Magnitude, Event Depth.

Date	Station	Tr-Data (s)	Tr-AK135 (s)	QFreq	1/QFreq	Q	1/Q	G
24/06/2011	ADK	931.1	935.4	70	0.0142	100	0.0100	0.65
13/11/2017	BCIP	936.6	934.9	119	0.0084	206	0.0049	0.86
24/08/2016	CHTO	932.7	934.8	121	0.0082	95	0.0105	0.43
08/12/2016	COR	941.8	934.8	82	0.0123	137	0.0073	0.66
23/09/2016	DAV	935.7	935.7	29	0.0345	37	0.0270	0.79
10/01/2017	DAV	934.1	935.1	78	0.0128	69	0.0144	0.41
02/02/2013	ERM	935.8	935.8	74	0.0135	231	0.0043	0.76
20/07/2014	ERM	930.4	934.7	65	0.0154	107	0.0093	0.78
16/02/2015	ERM	934.4	935.6	133	0.0075	164	0.0061	0.67
12/05/2015	ERM	933.4	935.3	333	0.0030	177	0.0057	0.43
07/07/2015	ERM	933.6	935.1	83	0.0121	441	0.0023	0.87
14/01/2016	ERM	935.3	935.8	182	0.0055	270	0.0037	0.62
19/08/2016	HOPE	932.9	935.4	238	0.0042	175	0.0057	0.49
16/08/2005	INU	934.8	934.7	170	0.0059	180	0.0056	0.51
13/03/2014	INU	934.8	934.8	654	0.0015	443	0.0023	0.50
24/10/2012	JTS	939.0	935.8	202	0.0050	292	0.0034	0.65
05/12/2016	KAPI	932.9	934.9	103	0.0097	148	0.0068	0.59
24/10/2017	KAPI	929.7	935.0	145	0.0069	142	0.0071	0.60
15/10/2006	KIP	938.6	935.5	203	0.0049	97	0.0103	0.38
20/06/2011	LVC	937.4	935.8	951	0.0011	485	0.0021	0.40
10/10/2017	LVC	938.1	935.0	463	0.0022	118	0.0085	0.41
04/07/2010	MAJO	934.3	934.8	141	0.0071	126	0.0079	0.46
14/03/2010	MAJO	931.5	935.4	189	0.0053	281	0.0036	0.53
12/03/2011	MAJO	936.5	935.1	82	0.0121	128	0.0078	0.69
22/06/2011	MAJO	933.3	934.8	114	0.0087	135	0.0074	0.55
24/07/2011	MAJO	931.6	935.4	160	0.0063	187	0.0053	0.50
23/07/2011	MAJO	934.4	935.1	501	0.0020	273	0.0037	0.45
30/07/2011	MAJO	935.3	935.5	77	0.0130	145	0.0069	0.78
07/04/2011	MAJO	935.0	935.3	88	0.0114	143	0.0070	0.68
17/06/2012	MAJO	934.4	935.1	172	0.0058	249	0.0040	0.56
11/07/2014	MAJO	933.3	935.3	175	0.0057	125	0.0080	0.43
16/02/2015	MAJO	934.4	934.7	224	0.0045	299	0.0033	0.55
12/05/2015	MAJO	934.4	935.1	388	0.0026	271	0.0037	0.46
05/04/2013	MDJ	934.1	935.6	425	0.0024	262	0.0038	0.43
17/01/1995	MSVF	943.9	935.0	186	0.0054	229	0.0044	0.48
05/08/1996	MSVF	942.8	934.8	152	0.0066	339	0.0029	0.57
04/10/2002	MSVF	944.9	934.9	222	0.0045	328	0.0031	0.59
17/11/2004	MSVF	943.8	935.1	416	0.0024	468	0.0021	0.47
19/07/2008	MSVF	943.5	934.9	303	0.0033	374	0.0027	0.49
22/11/2009	MSVF	944.8	935.2	157	0.0064	2544	0.0004	0.73
09/11/2009	MSVF	944.5	935.8	396	0.0025	396	0.0025	0.47

Table A2 continued from previous page

Date	Station	Tr-Data (s)	Tr-AK135 (s)	QFreq	1/QFreq	Q	1/Q	G
15/09/2011	MSVF	945.6	934.8	175	0.0057	210	0.0048	0.49
01/11/2014	MSVF	943.4	934.9	125	0.0080	339	0.0029	0.64
21/07/2014	MSVF	943.5	935.1	246	0.0041	606	0.0016	0.53
27/05/2016	MSVF	943.9	934.9	322	0.0031	403	0.0025	0.50
24/09/2016	MSVF	943.9	935.0	1758	0.0006	4084	0.0002	0.49
19/08/2017	MSVF	935.4	935.4	84	0.0119	38	0.0262	0.44
24/08/2011	NNA	935.2	934.8	211	0.0047	106	0.0094	0.46
18/05/2016	OTAV	931.3	935.7	212	0.0047	127	0.0079	0.41
16/11/2012	PET	933.5	935.0	95	0.0106	179	0.0056	0.72
20/03/2016	PET	933.3	935.5	266	0.0038	659	0.0015	0.57
30/01/2016	PET	935.7	935.7	216	0.0046	480	0.0021	0.60
05/03/2014	SANVU	941.6	935.5	104	0.0096	72	0.0140	0.38
13/01/2014	SJG	928.8	882.9	74	0.0135	65	0.0154	0.46
20/01/2014	SNZO	936.6	935.7	140	0.0072	114	0.0087	0.50
31/05/2016	TATO	936.6	935.7	230	0.0044	263	0.0038	0.50
18/04/2011	URZ	937.6	934.9	120	0.0083	110	0.0091	0.49
02/02/2013	YSS	933.9	935.0	52	0.0192	357	0.0028	1.00

Table A2: Results for Event-Station pairs: Travel Time between ScS and ScSScS measured from data and from AK135 Travel Time model, Q Frequency Domain, 1/Q Frequency Domain, Q Time Domain, 1/Q Time Domain, Geometrical Spreading Factor

Date	Station	Instrument	Component	EVDP	1/Q Frequency, sScS	1/Q Frequency, ScS
10/01/2017	DAV	10	Transverse	613	0.0048	0.0128
29/12/2016	KAPI	0	LH1	79	0.0081	0.0097
05/04/2013	MDJ	0	Transverse	572	0.0028	0.0024
17/11/2004	MSVF	0	LH1	592	0.0111	0.0024
15/09/2011	MSVF	0	LH1	629	0.0167	0.0057
21/07/2014	MSVF	10	LH2	615	0.0101	0.0041
27/05/2016	MSVF	0	LH2	567	0.0053	0.0031
24/09/2016	MSVF	0	LH1	596	0.0082	0.0006
05/03/2014	SANVU	0	Transverse	661	0.0070	0.0096

Table A3: Comparison of sScS 1/Q and ScS 1/Q along with station and event information.

Table A4: My caption

Date	Station	Component	EVDP	1/Q Frequency, S650ScS	1/Q Frequency, ScS
12/05/2015	ERM	Transverse	35	0.0113	0.0030
16/08/2005	INU	Transverse	37	0.0078	0.0059
24/08/2011	NNA	LH1	144	0.0147	0.0047
24/07/2011	MAJO	Transverse	41	0.0235	0.0063
14/03/2010	MAJO	Transverse	40	0.0113	0.0053
22/06/2011	MAJO	Transverse	32	0.0784	0.0087
31/05/2016	TATO	LH2	246	0.0075	0.0044

Table A5: Comparison of S650ScS 1/Q and ScS 1/Q along with station and event information.

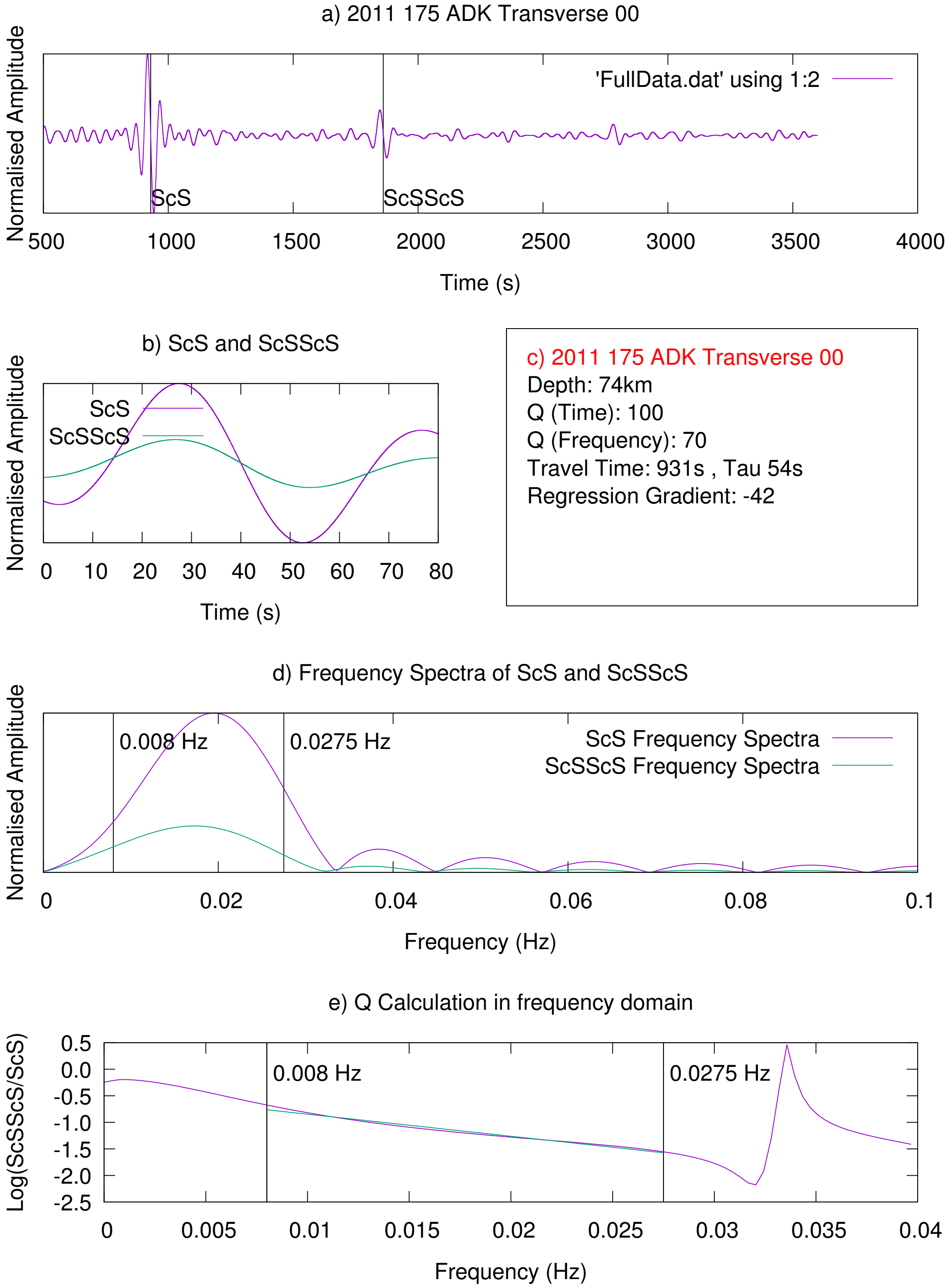

Figure A1: a) Seismogram after butterworth filtering and the locations of the ScS and ScSScS arrivals. b) 80 second ScS and ScSScS time windows plotted on top of eachother. c) Year and Day number (Normal Date: 24/06/2011), Station Name, Component, Instrument, Event depth, Q(time), Q(Frequency), time difference between ScS and ScSScS and the value of the frequency spectra gradient. d) The frequency spectra of the ScS and ScSScS phases and e) Graph upon which spectral gradient is calculated. The green line shows the line fitted through the data.

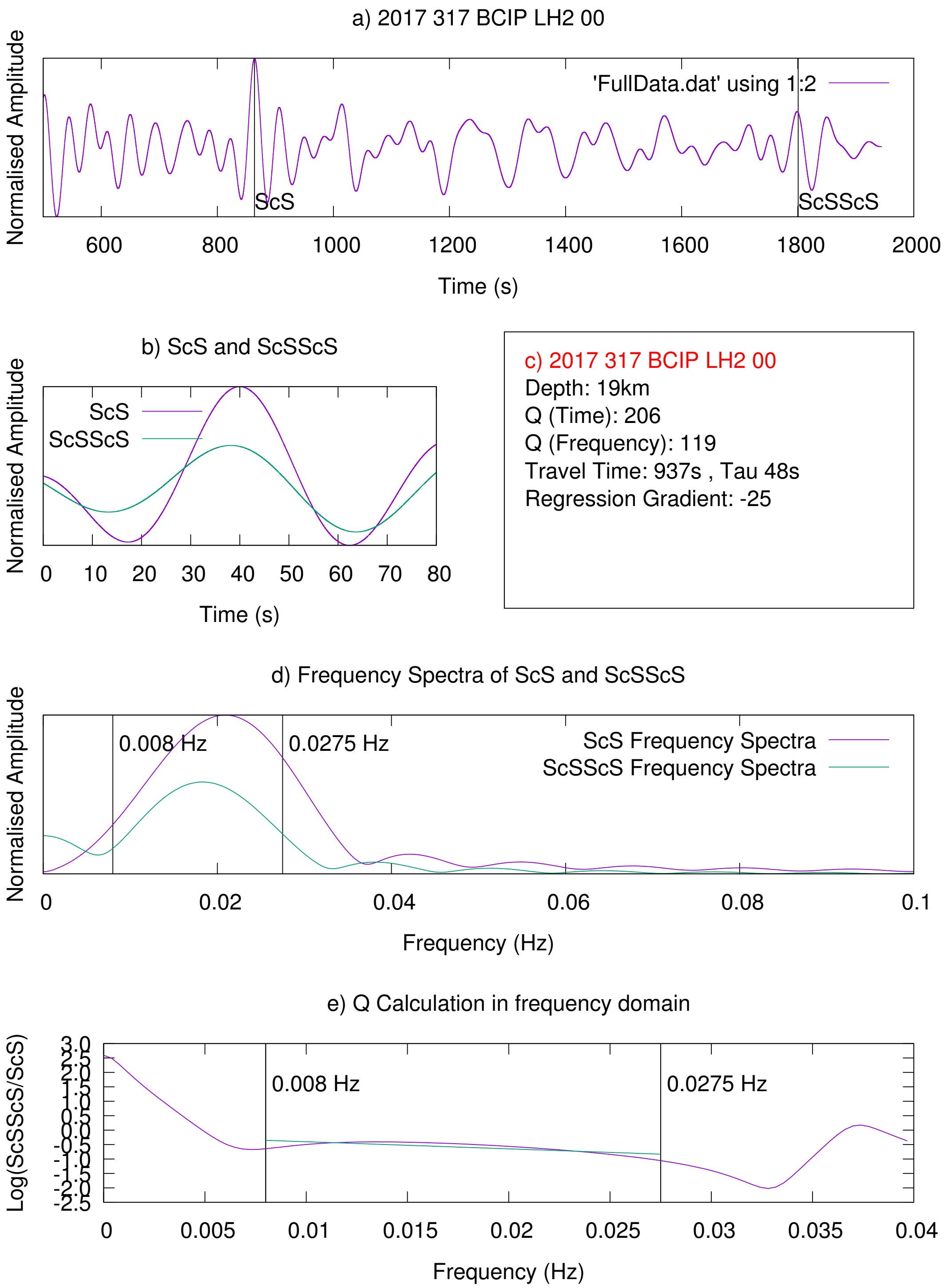

Figure A2: a) Seismogram after butterworth filtering and the locations of the ScS and ScSScS arrivals. b) 80 second ScS and ScSScS time windows plotted on top of eachother. c) Year and Day number (Normal Date: 13/11/2017), Station Name, Component, Instrument, Event depth, Q(time), Q(Frequency), time difference between ScS and ScSScS and the value of the frequency spectra gradient. d) The frequency spectra of the ScS and ScSScS phases and e) Graph upon which spectral gradient is calculated. The green line shows the line fitted through the data.

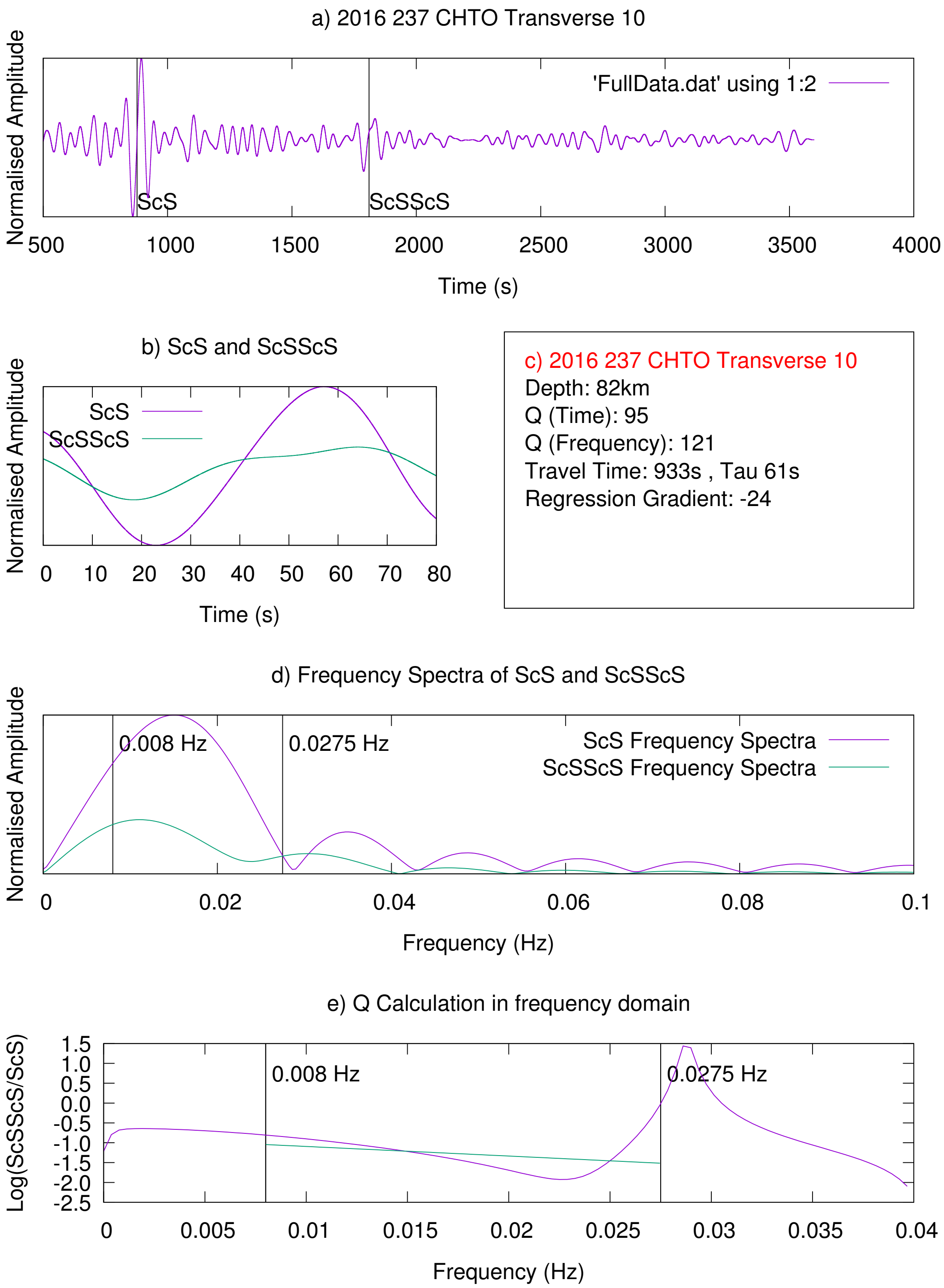

Figure A3: a) Seismogram after butterworth filtering and the locations of the ScS and ScSScS arrivals. b) 80 second ScS and ScSScS time windows plotted on top of eachother. c) Year and Day number (Normal Date: 24/08/2016), Station Name, Component, Instrument, Event depth, Q(time), Q(Frequency), time difference between ScS and ScSScS and the value of the frequency spectra gradient. d) The frequency spectra of the ScS and ScSScS phases and e) Graph upon which spectral gradient is calculated. The green line shows the line fitted through the data.

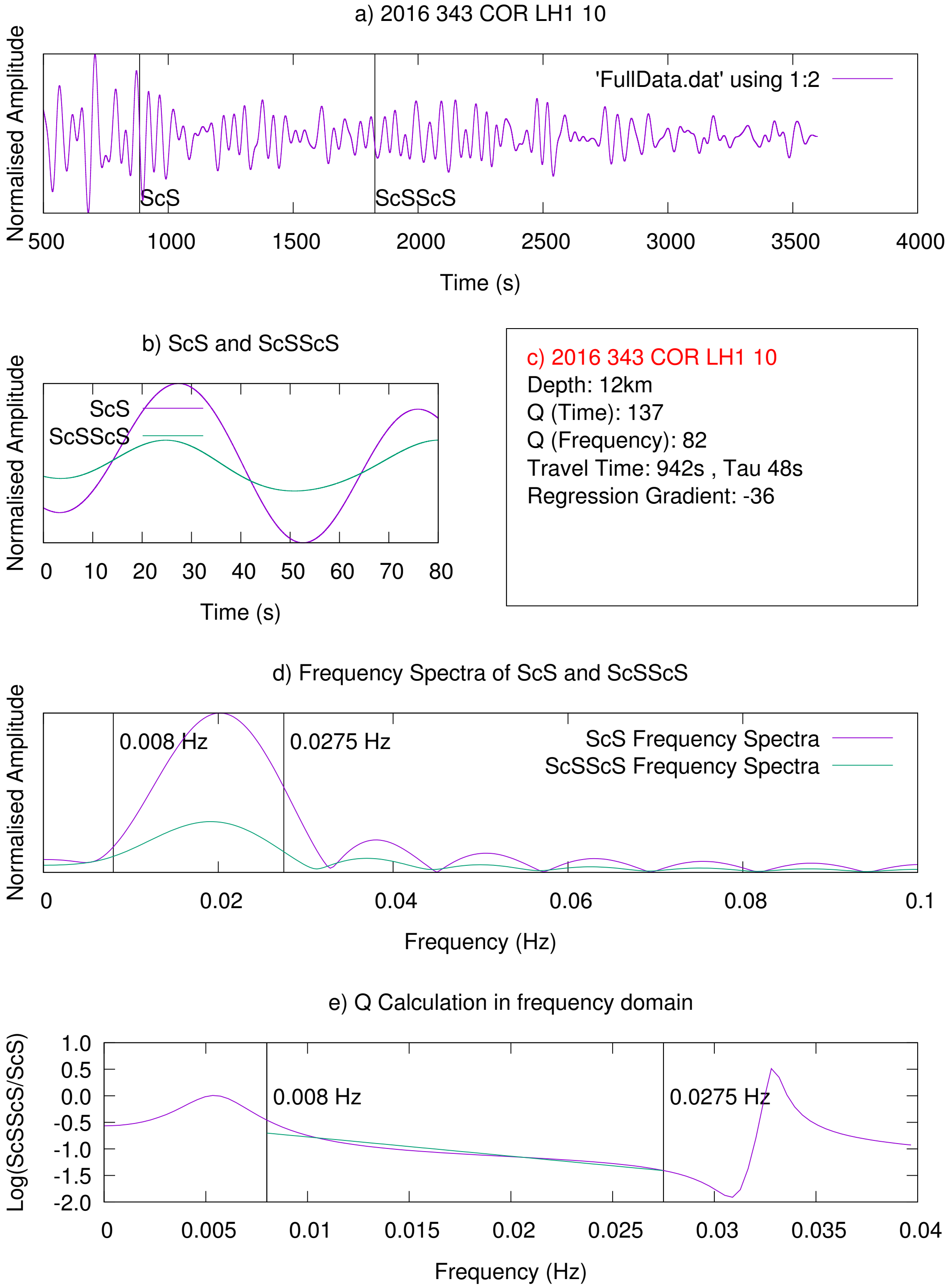

Figure A4: a) Seismogram after butterworth filtering and the locations of the ScS and ScSScS arrivals. b) 80 second ScS and ScSScS time windows plotted on top of eachother. c) Year and Day number (Normal Date: 08/12/2016), Station Name, Component, Instrument, Event depth, Q(time), Q(Frequency), time difference between ScS and ScSScS and the value of the frequency spectra gradient. d) The frequency spectra of the ScS and ScSScS phases and e) Graph upon which spectral gradient is calculated. The green line shows the line fitted through the data.

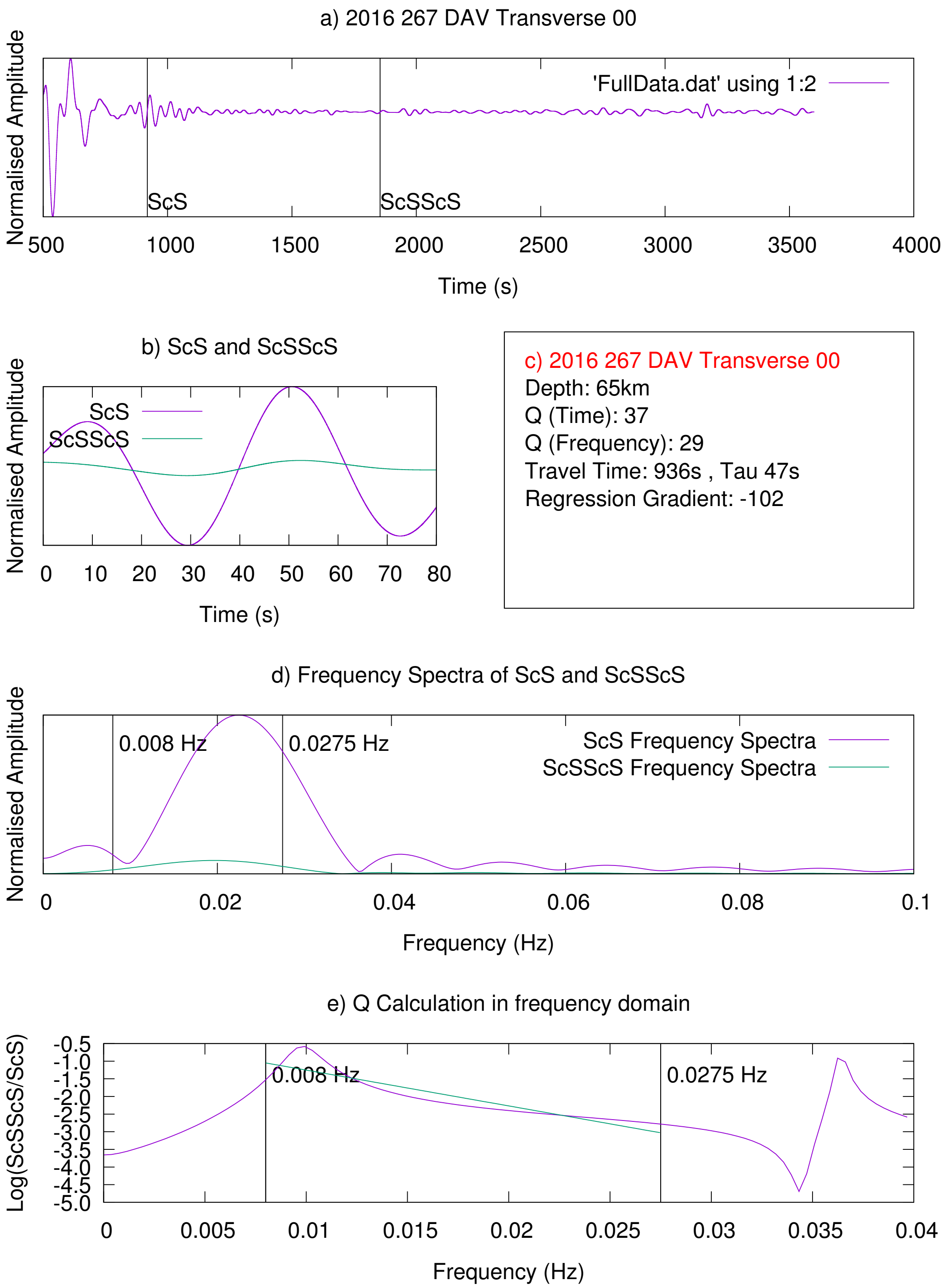

Figure A5: a) Seismogram after butterworth filtering and the locations of the ScS and ScSScS arrivals. b) 80 second ScS and ScSScS time windows plotted on top of eachother. c) Year and Day number (Normal Date: 23/09/2016), Station Name, Component, Instrument, Event depth, Q(time), Q(Frequency), time difference between ScS and ScSScS and the value of the frequency spectra gradient. d) The frequency spectra of the ScS and ScSScS phases and e) Graph upon which spectral gradient is calculated. The green line shows the line fitted through the data.

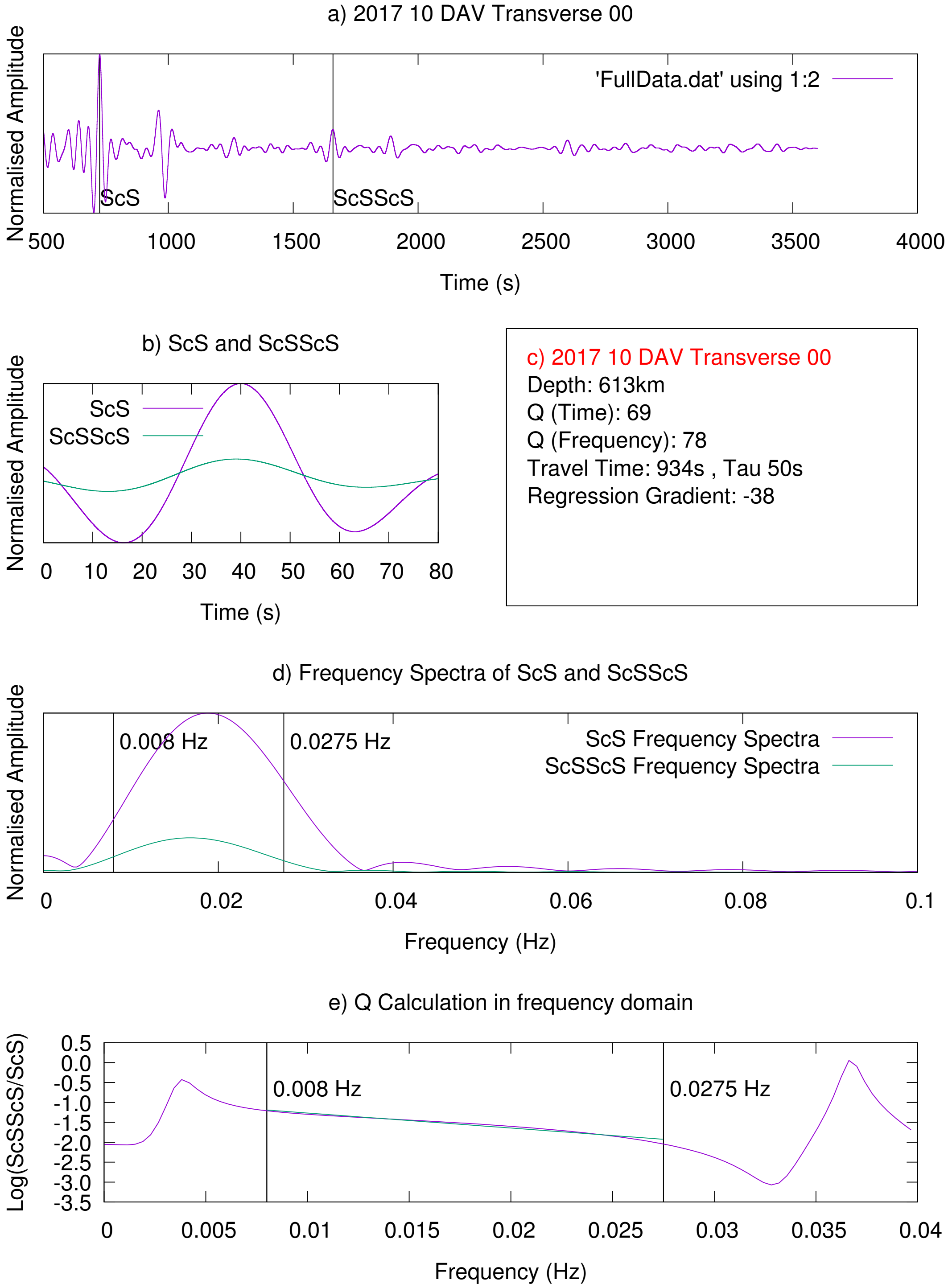

Figure A6: a) Seismogram after butterworth filtering and the locations of the ScS and ScSScS arrivals. b) 80 second ScS and ScSScS time windows plotted on top of eachother. c) Year and Day number (Normal Date: 10/01/2017), Station Name, Component, Instrument, Event depth, Q(time), Q(Frequency), time difference between ScS and ScSScS and the value of the frequency spectra gradient. d) The frequency spectra of the ScS and ScSScS phases and e) Graph upon which spectral gradient is calculated. The green line shows the line fitted through the data.

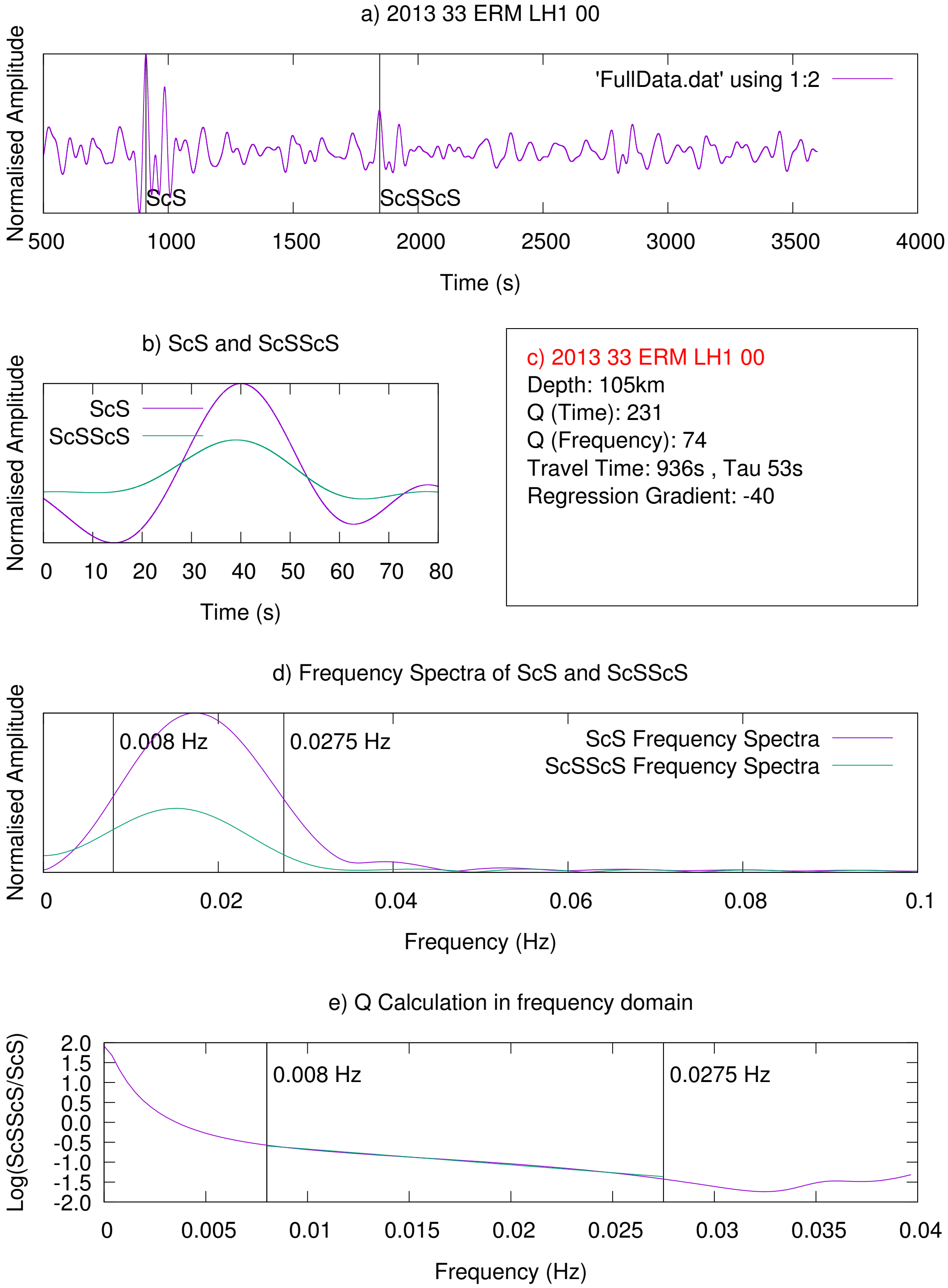

Figure A7: a) Seismogram after butterworth filtering and the locations of the ScS and ScSScS arrivals. b) 80 second ScS and ScSScS time windows plotted on top of eachother. c) Year and Day number (Normal Date: 02/02/2013), Station Name, Component, Instrument, Event depth, Q(time), Q(Frequency), time difference between ScS and ScSScS and the value of the frequency spectra gradient. d) The frequency spectra of the ScS and ScSScS phases and e) Graph upon which spectral gradient is calculated. The green line shows the line fitted through the data.

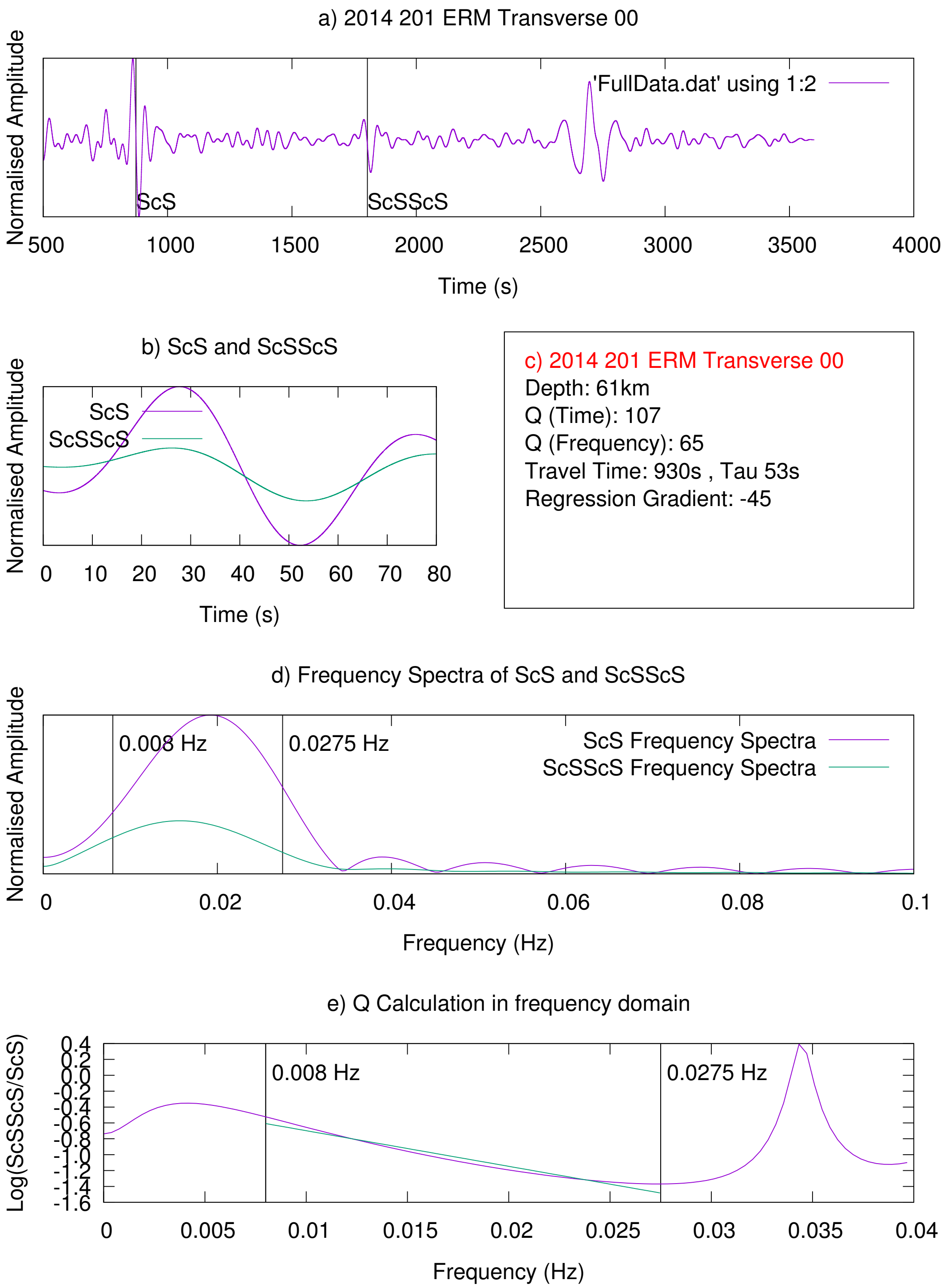

Figure A8: a) Seismogram after butterworth filtering and the locations of the ScS and ScSScS arrivals. b) 80 second ScS and ScSScS time windows plotted on top of eachother. c) Year and Day number (Normal Date: 20/07/2014), Station Name, Component, Instrument, Event depth, Q(time), Q(Frequency), time difference between ScS and ScSScS and the value of the frequency spectra gradient. d) The frequency spectra of the ScS and ScSScS phases and e) Graph upon which spectral gradient is calculated. The green line shows the line fitted through the data.

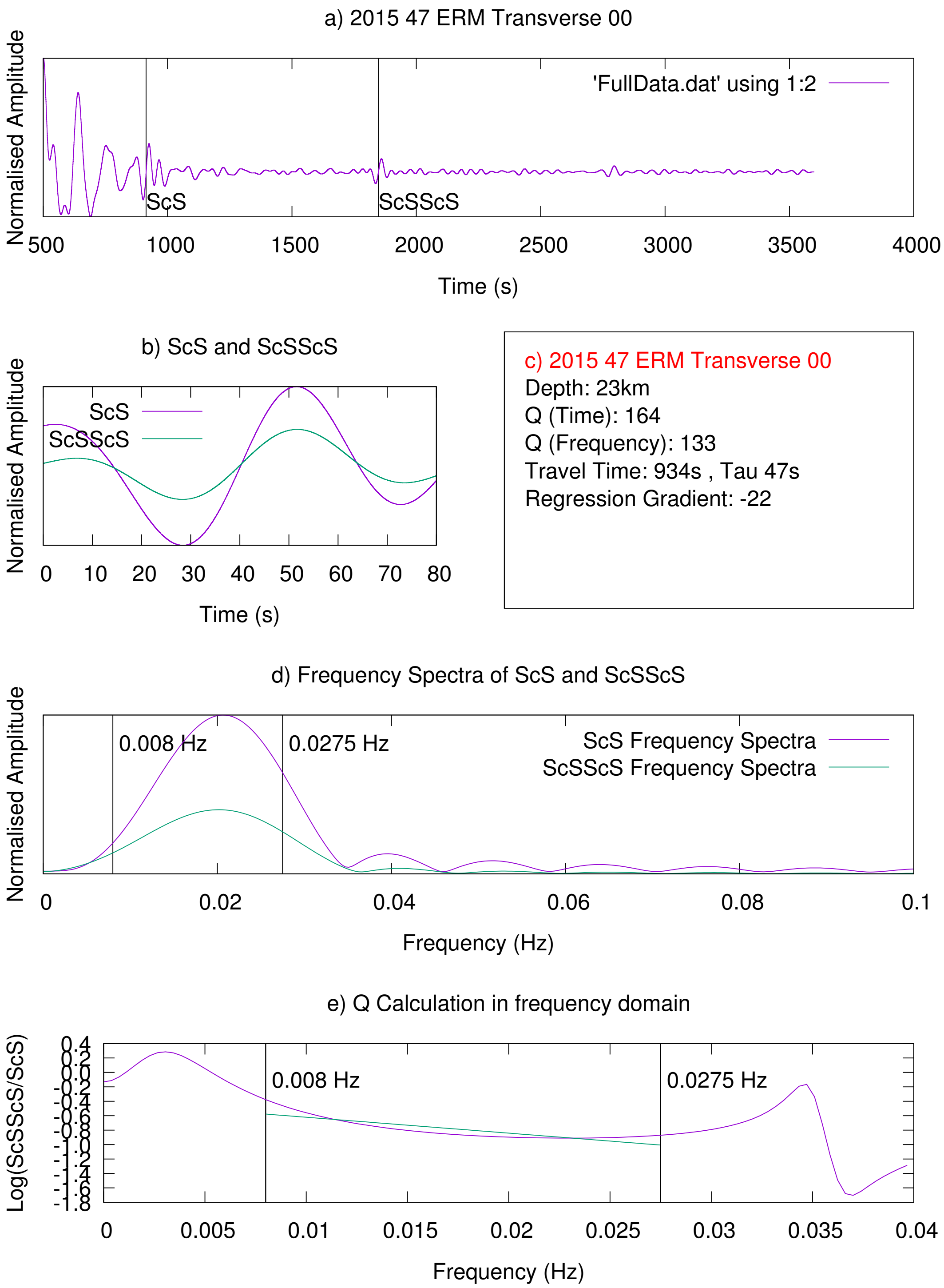

Figure A9: a) Seismogram after butterworth filtering and the locations of the ScS and ScSScS arrivals. b) 80 second ScS and ScSScS time windows plotted on top of eachother. c) Year and Day number (Normal Date: 16/02/2015), Station Name, Component, Instrument, Event depth, Q(time), Q(Frequency), time difference between ScS and ScSScS and the value of the frequency spectra gradient. d) The frequency spectra of the ScS and ScSScS phases and e) Graph upon which spectral gradient is calculated. The green line shows the line fitted through the data.

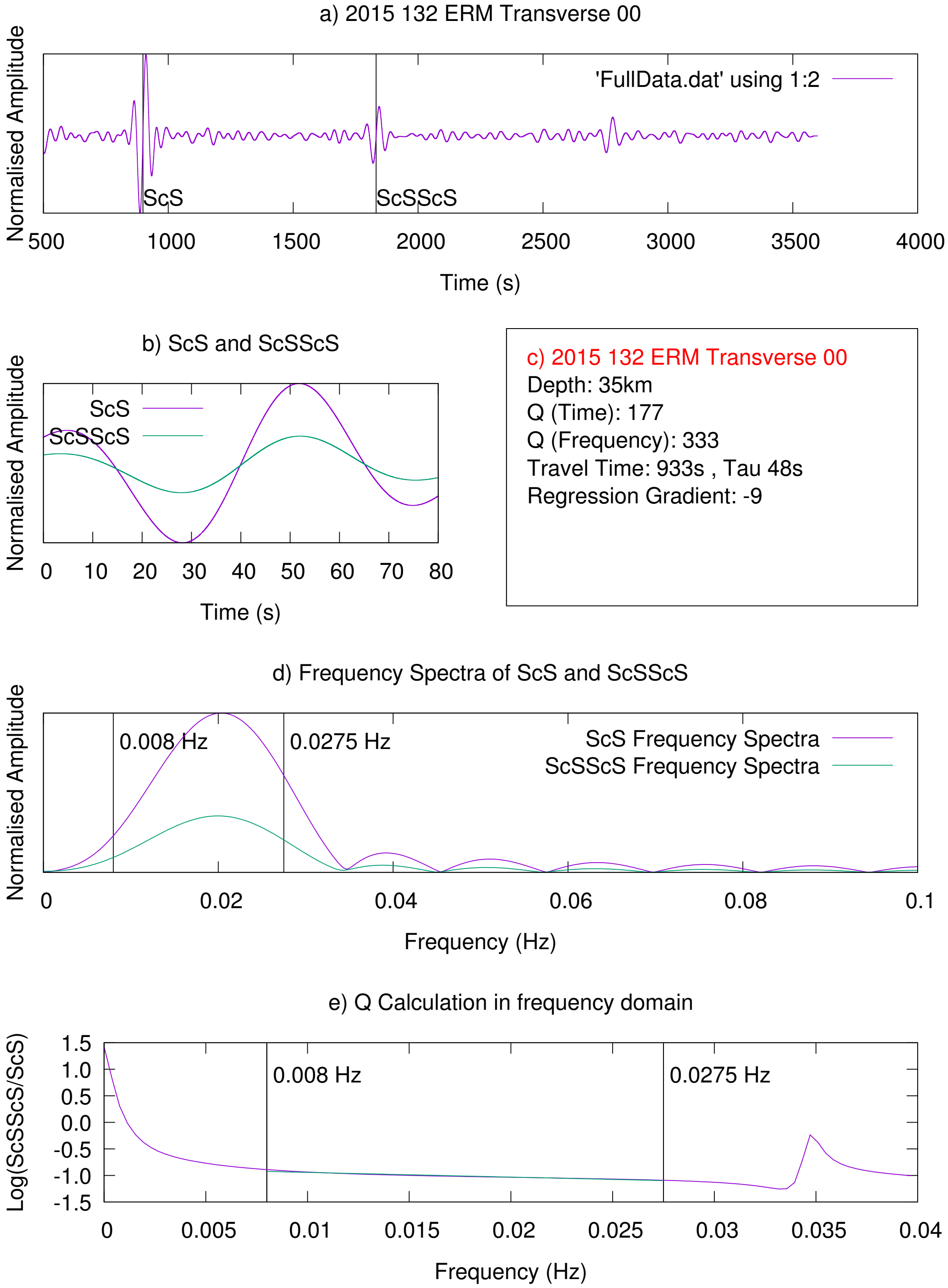

Figure A10: a) Seismogram after butterworth filtering and the locations of the ScS and ScSScS arrivals. b) 80 second ScS and ScSScS time windows plotted on top of eachother. c) Year and Day number (Normal Date: 12/05/2015), Station Name, Component, Instrument, Event depth, Q(time), Q(Frequency), time difference between ScS and ScSScS and the value of the frequency spectra gradient. d) The frequency spectra of the ScS and ScSScS phases and e) Graph upon which spectral gradient is calculated. The green line shows the line fitted through the data.

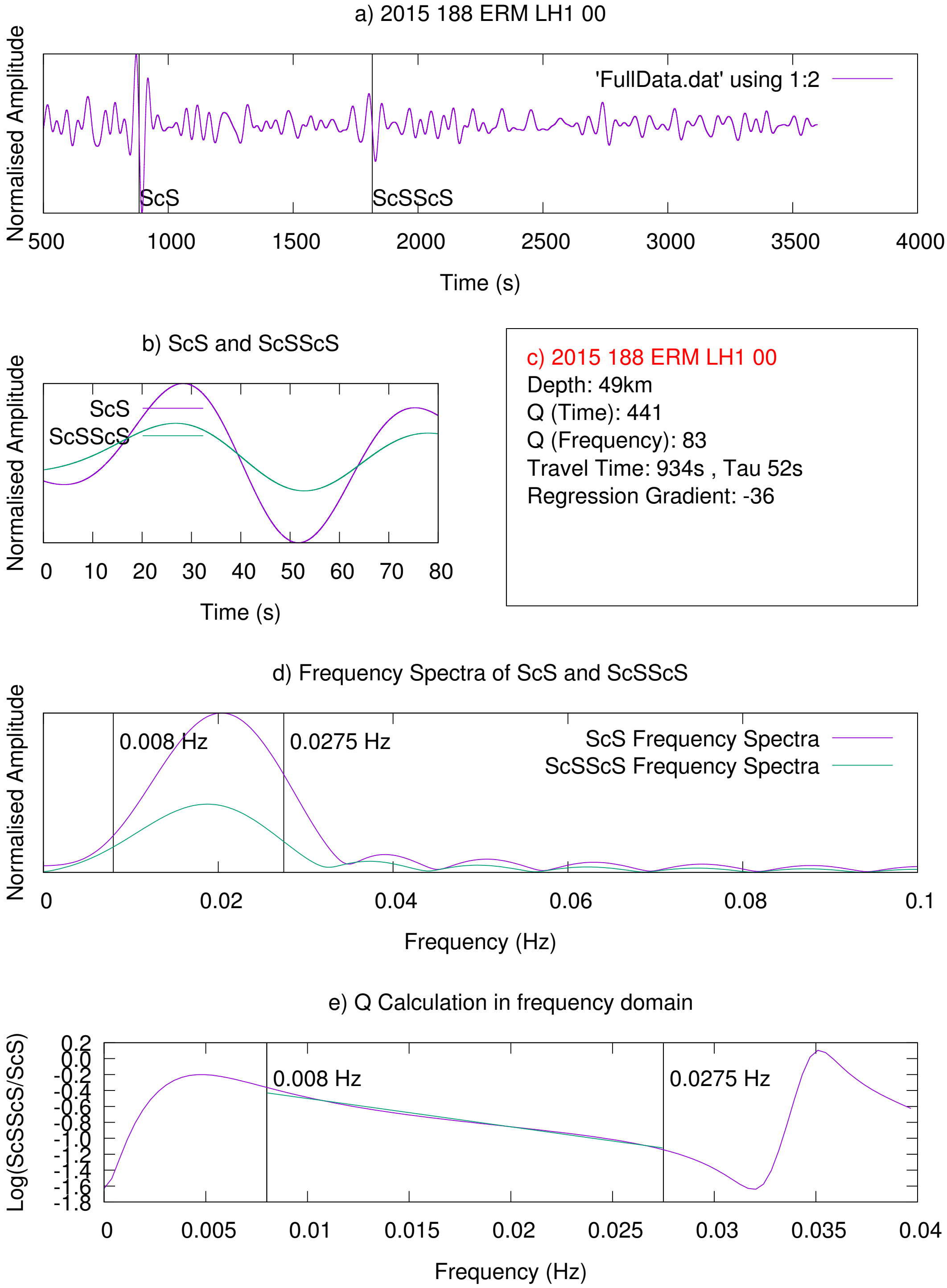

Figure A11: a) Seismogram after butterworth filtering and the locations of the ScS and ScSScS arrivals. b) 80 second ScS and ScSScS time windows plotted on top of eachother. c) Year and Day number (Normal Date: 07/07/2015), Station Name, Component, Instrument, Event depth, Q(time), Q(Frequency), time difference between ScS and ScSScS and the value of the frequency spectra gradient. d) The frequency spectra of the ScS and ScSScS phases and e) Graph upon which spectral gradient is calculated. The green line shows the line fitted through the data.

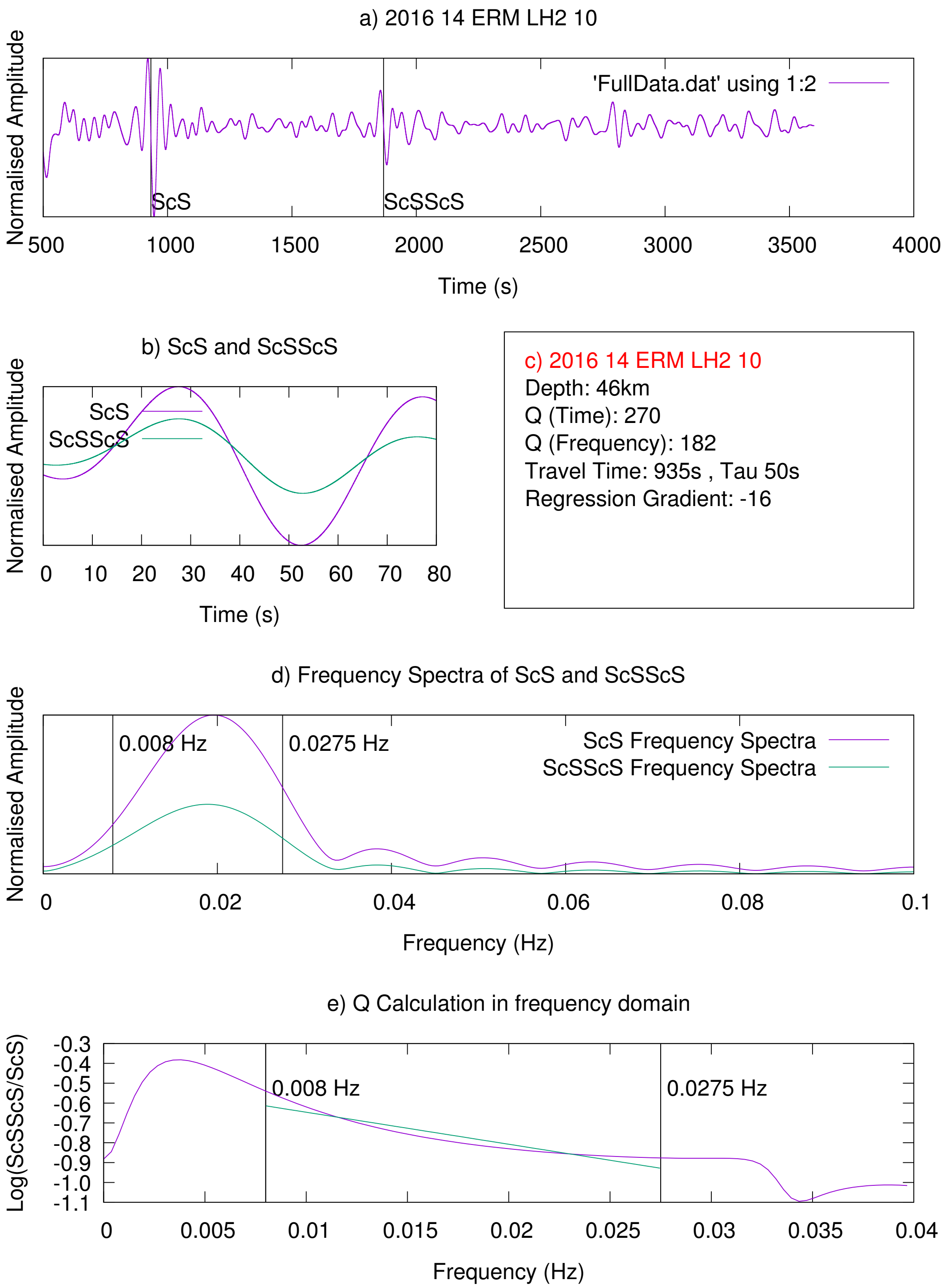

Figure A12: a) Seismogram after butterworth filtering and the locations of the ScS and ScSScS arrivals. b) 80 second ScS and ScSScS time windows plotted on top of eachother. c) Year and Day number (Normal Date: 14/01/2016), Station Name, Component, Instrument, Event depth, Q(time), Q(Frequency), time difference between ScS and ScSScS and the value of the frequency spectra gradient. d) The frequency spectra of the ScS and ScSScS phases and e) Graph upon which spectral gradient is calculated. The green line shows the line fitted through the data.

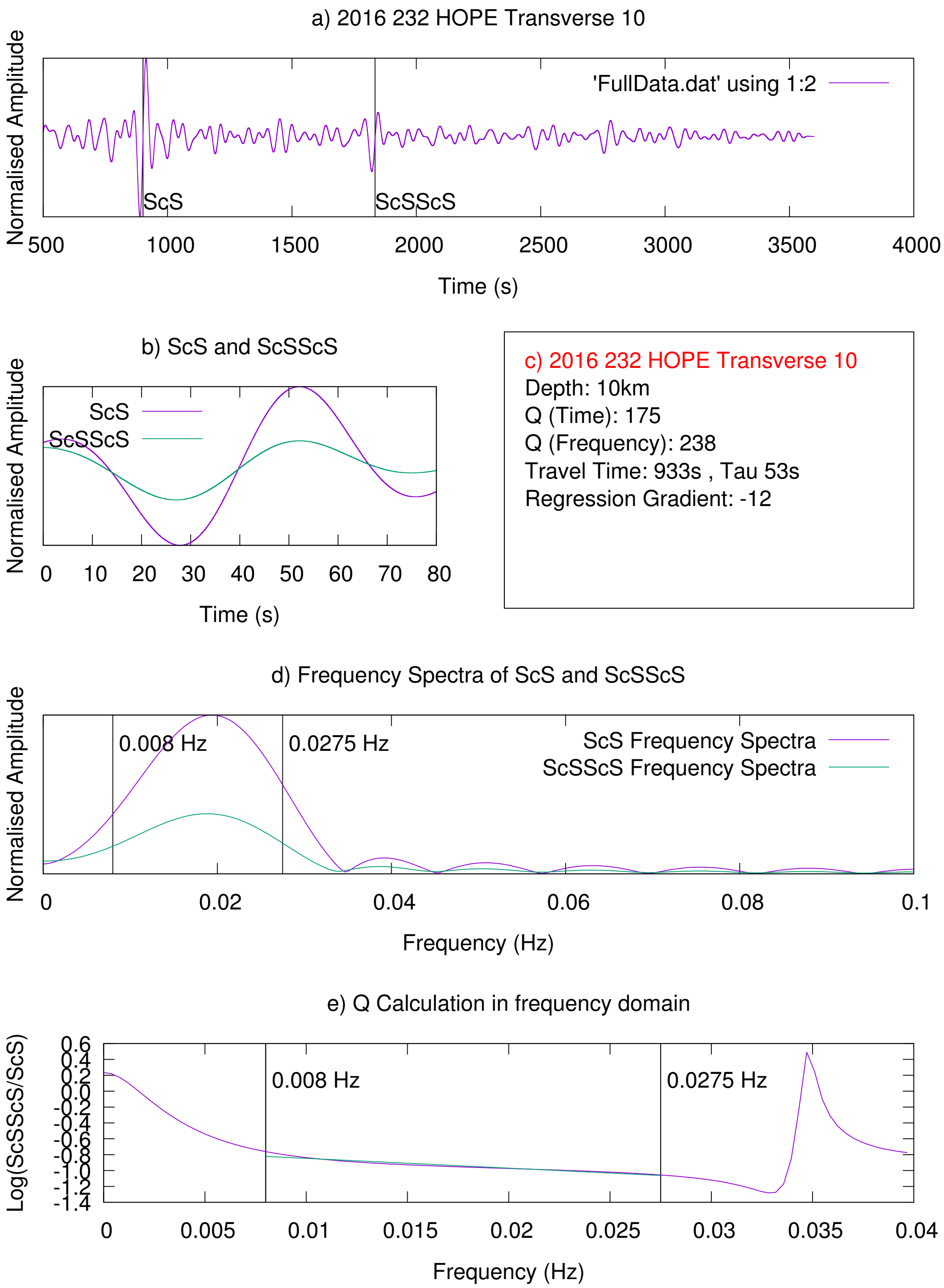

Figure A13: a) Seismogram after butterworth filtering and the locations of the ScS and ScSScS arrivals. b) 80 second ScS and ScSScS time windows plotted on top of eachother. c) Year and Day number (Normal Date: 19/08/2016), Station Name, Component, Instrument, Event depth, Q(time), Q(Frequency), time difference between ScS and ScSScS and the value of the frequency spectra gradient. d) The frequency spectra of the ScS and ScSScS phases and e) Graph upon which spectral gradient is calculated. The green line shows the line fitted through the data.

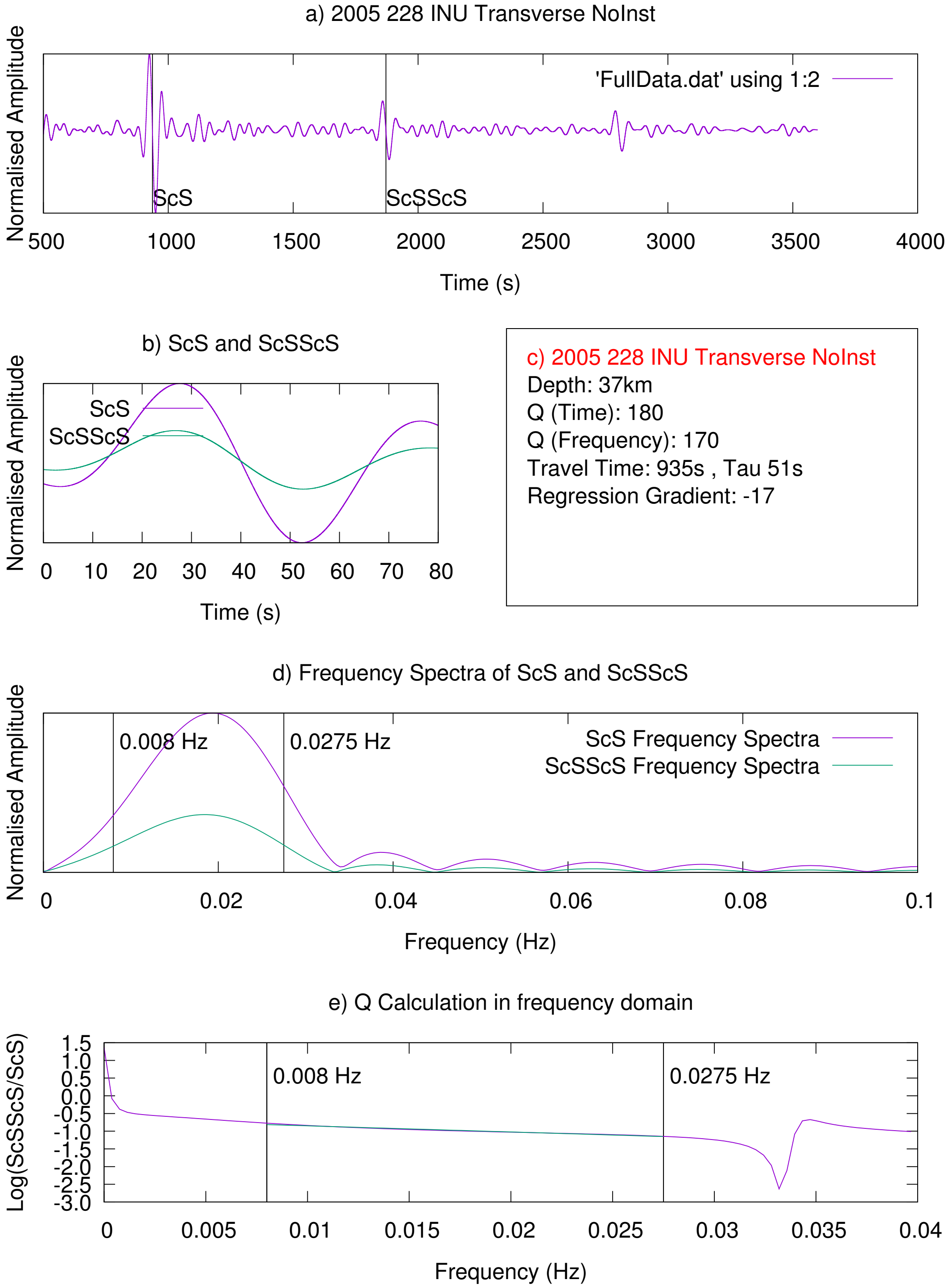

Figure A14: a) Seismogram after butterworth filtering and the locations of the ScS and ScSScS arrivals. b) 80 second ScS and ScSScS time windows plotted on top of eachother. c) Year and Day number (Normal Date: 16/08/2005), Station Name, Component, Instrument, Event depth, Q(time), Q(Frequency), time difference between ScS and ScSScS and the value of the frequency spectra gradient. d) The frequency spectra of the ScS and ScSScS phases and e) Graph upon which spectral gradient is calculated. The green line shows the line fitted through the data.

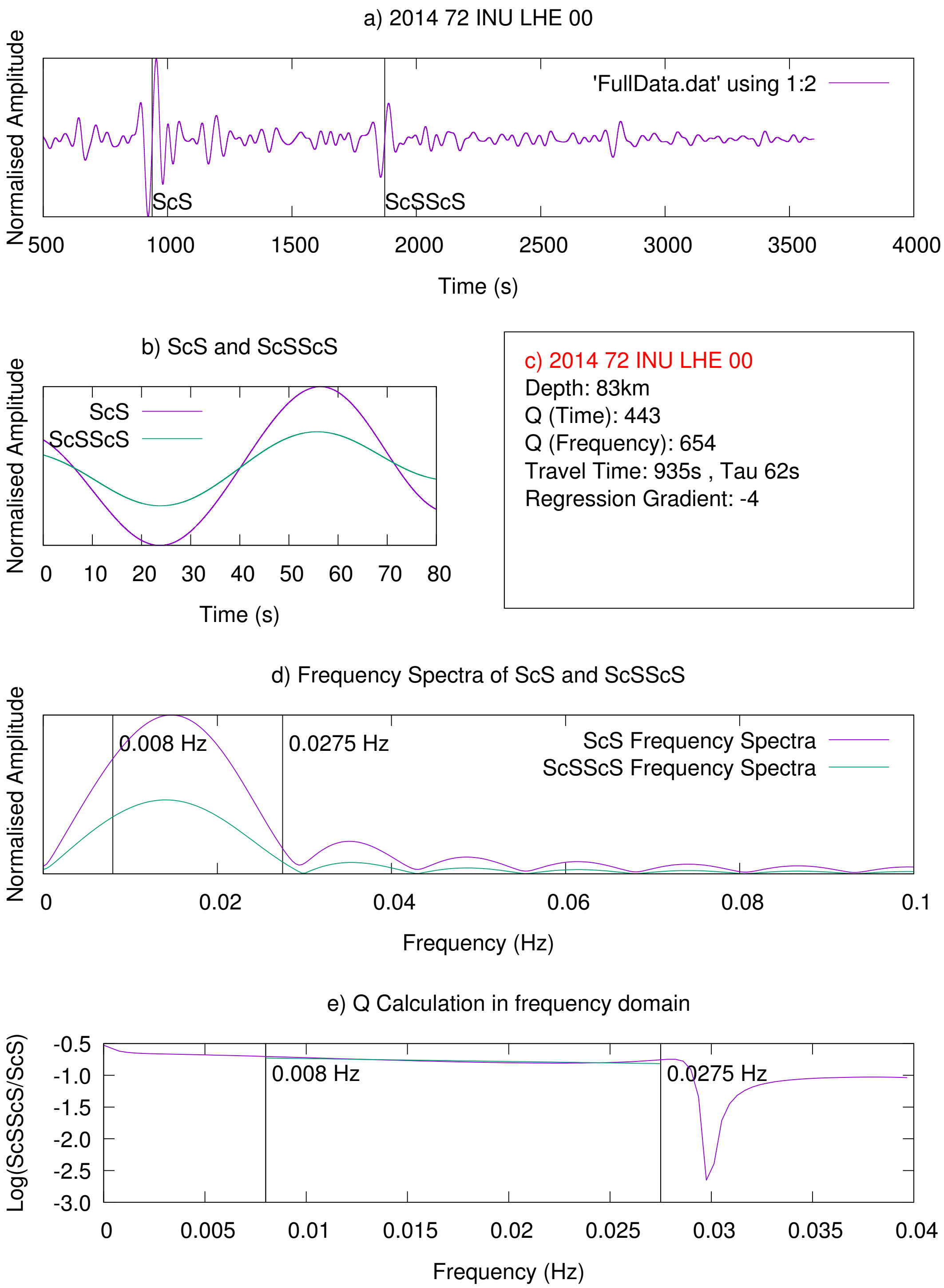

Figure A15: a) Seismogram after butterworth filtering and the locations of the ScS and ScSScS arrivals. b) 80 second ScS and ScSScS time windows plotted on top of eachother. c) Year and Day number (Normal Date: 13/03/2014), Station Name, Component, Instrument, Event depth, Q(time), Q(Frequency), time difference between ScS and ScSScS and the value of the frequency spectra gradient. d) The frequency spectra of the ScS and ScSScS phases and e) Graph upon which spectral gradient is calculated. The green line shows the line fitted through the data.

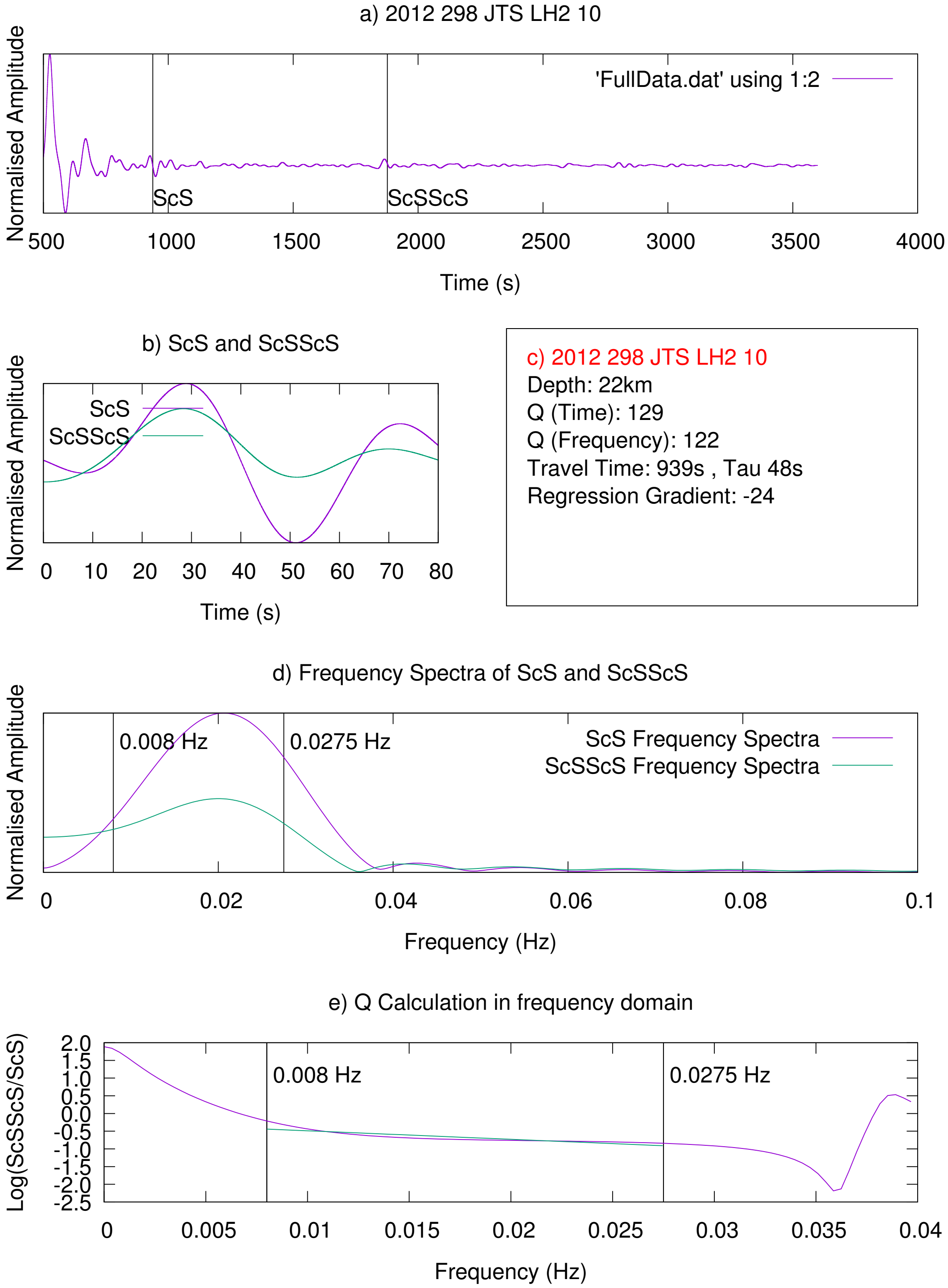

Figure A16: a) Seismogram after butterworth filtering and the locations of the ScS and ScSScS arrivals. b) 80 second ScS and ScSScS time windows plotted on top of eachother. c) Year and Day number (Normal Date: 24/10/2012), Station Name, Component, Instrument, Event depth, Q(time), Q(Frequency), time difference between ScS and ScSScS and the value of the frequency spectra gradient. d) The frequency spectra of the ScS and ScSScS phases and e) Graph upon which spectral gradient is calculated. The green line shows the line fitted through the data.

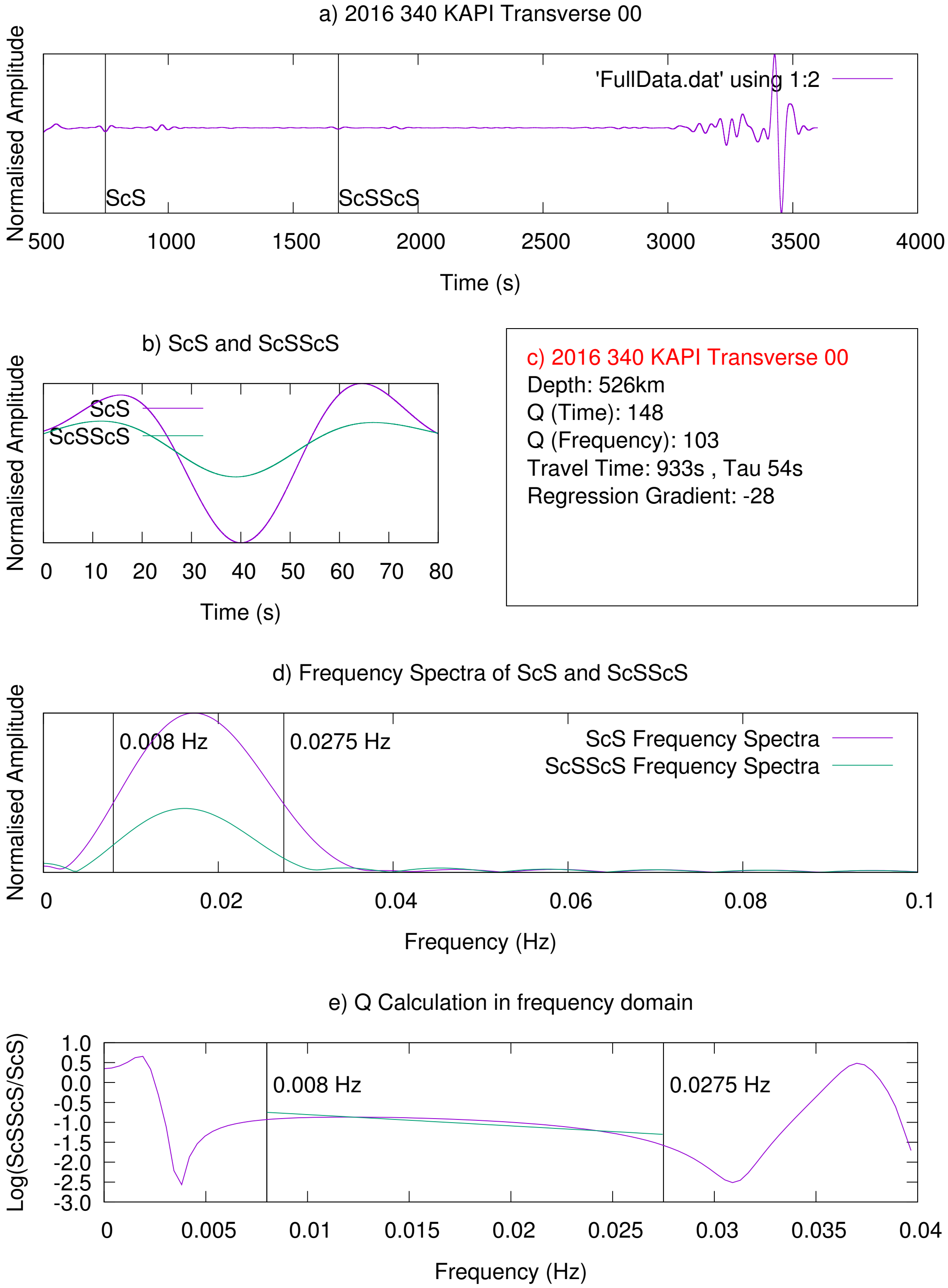

Figure A17: a) Seismogram after butterworth filtering and the locations of the ScS and ScSScS arrivals. b) 80 second ScS and ScSScS time windows plotted on top of eachother. c) Year and Day number (Normal Date: 05/12/2016), Station Name, Component, Instrument, Event depth, Q(time), Q(Frequency), time difference between ScS and ScSScS and the value of the frequency spectra gradient. d) The frequency spectra of the ScS and ScSScS phases and e) Graph upon which spectral gradient is calculated. The green line shows the line fitted through the data.

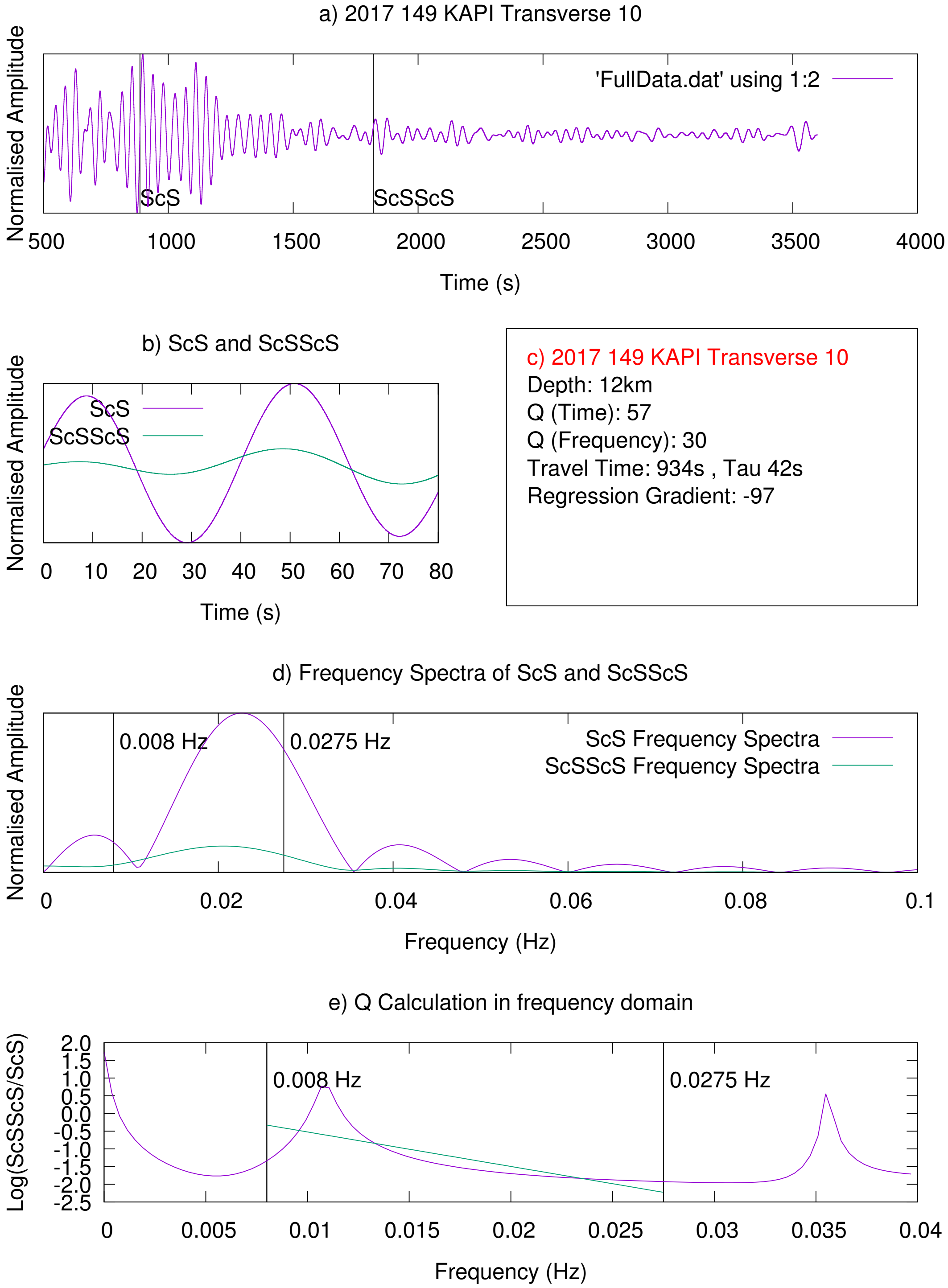

Figure A18: a) Seismogram after butterworth filtering and the locations of the ScS and ScSScS arrivals. b) 80 second ScS and ScSScS time windows plotted on top of eachother. c) Year and Day number (Normal Date: 24/10/2017), Station Name, Component, Instrument, Event depth, Q(time), Q(Frequency), time difference between ScS and ScSScS and the value of the frequency spectra gradient. d) The frequency spectra of the ScS and ScSScS phases and e) Graph upon which spectral gradient is calculated. The green line shows the line fitted through the data.

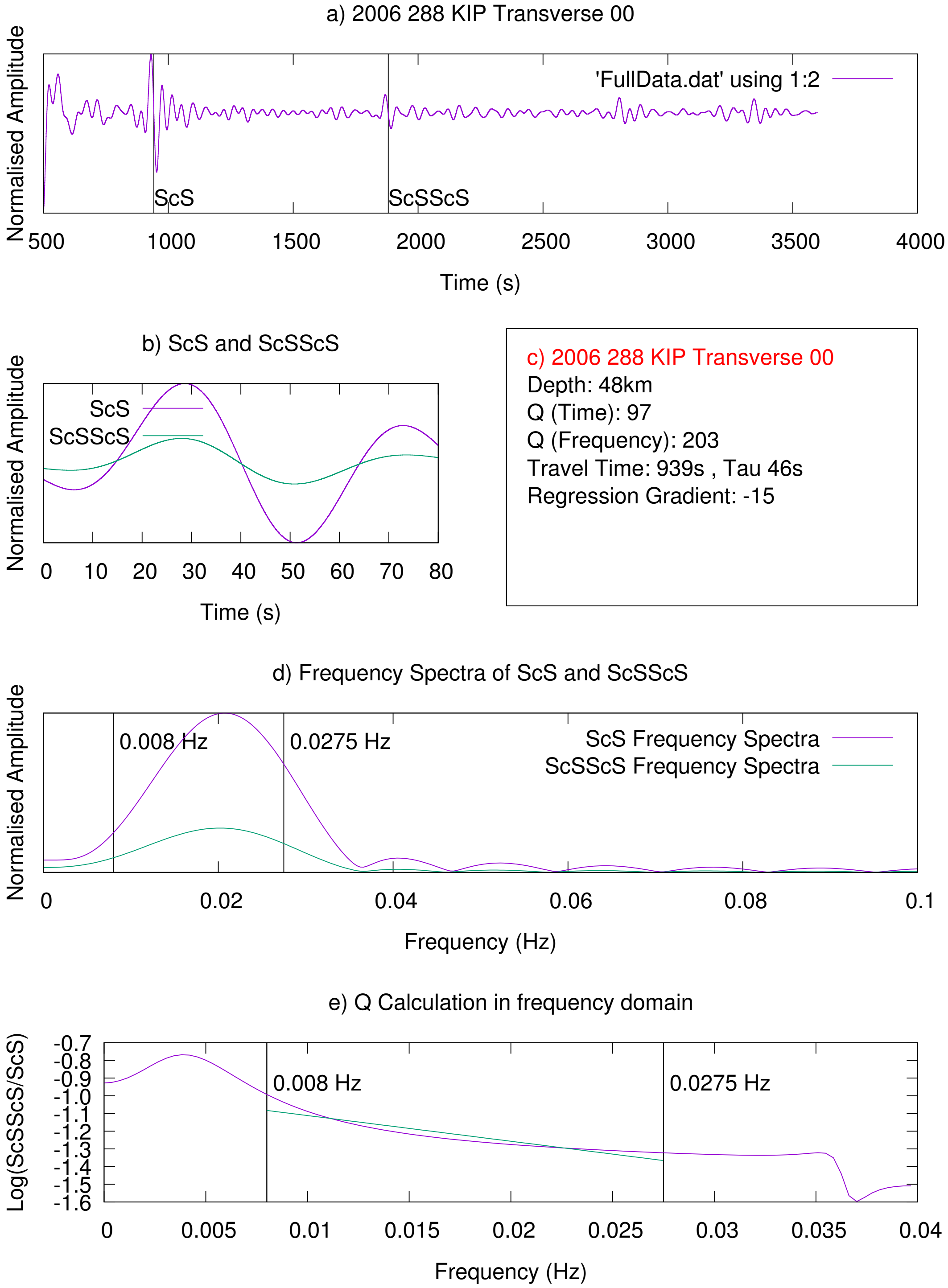

Figure A19: a) Seismogram after butterworth filtering and the locations of the ScS and ScSScS arrivals. b) 80 second ScS and ScSScS time windows plotted on top of eachother. c) Year and Day number (Normal Date: 15/10/2006), Station Name, Component, Instrument, Event depth, Q(time), Q(Frequency), time difference between ScS and ScSScS and the value of the frequency spectra gradient. d) The frequency spectra of the ScS and ScSScS phases and e) Graph upon which spectral gradient is calculated. The green line shows the line fitted through the data.

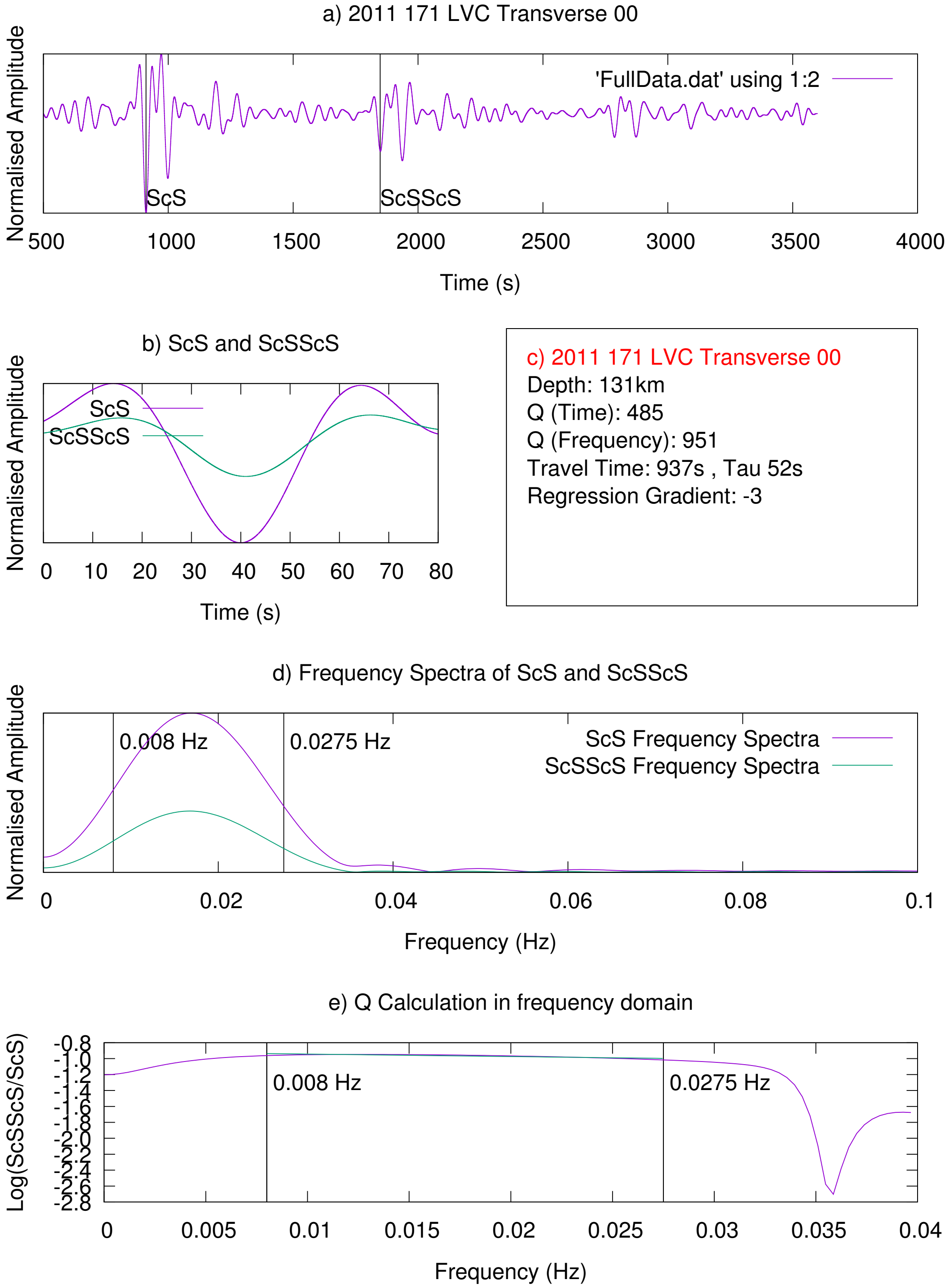

Figure A20: a) Seismogram after butterworth filtering and the locations of the ScS and ScSScS arrivals. b) 80 second ScS and ScSScS time windows plotted on top of eachother. c) Year and Day number (Normal Date: 20/06/2011), Station Name, Component, Instrument, Event depth, Q(time), Q(Frequency), time difference between ScS and ScSScS and the value of the frequency spectra gradient. d) The frequency spectra of the ScS and ScSScS phases and e) Graph upon which spectral gradient is calculated. The green line shows the line fitted through the data.

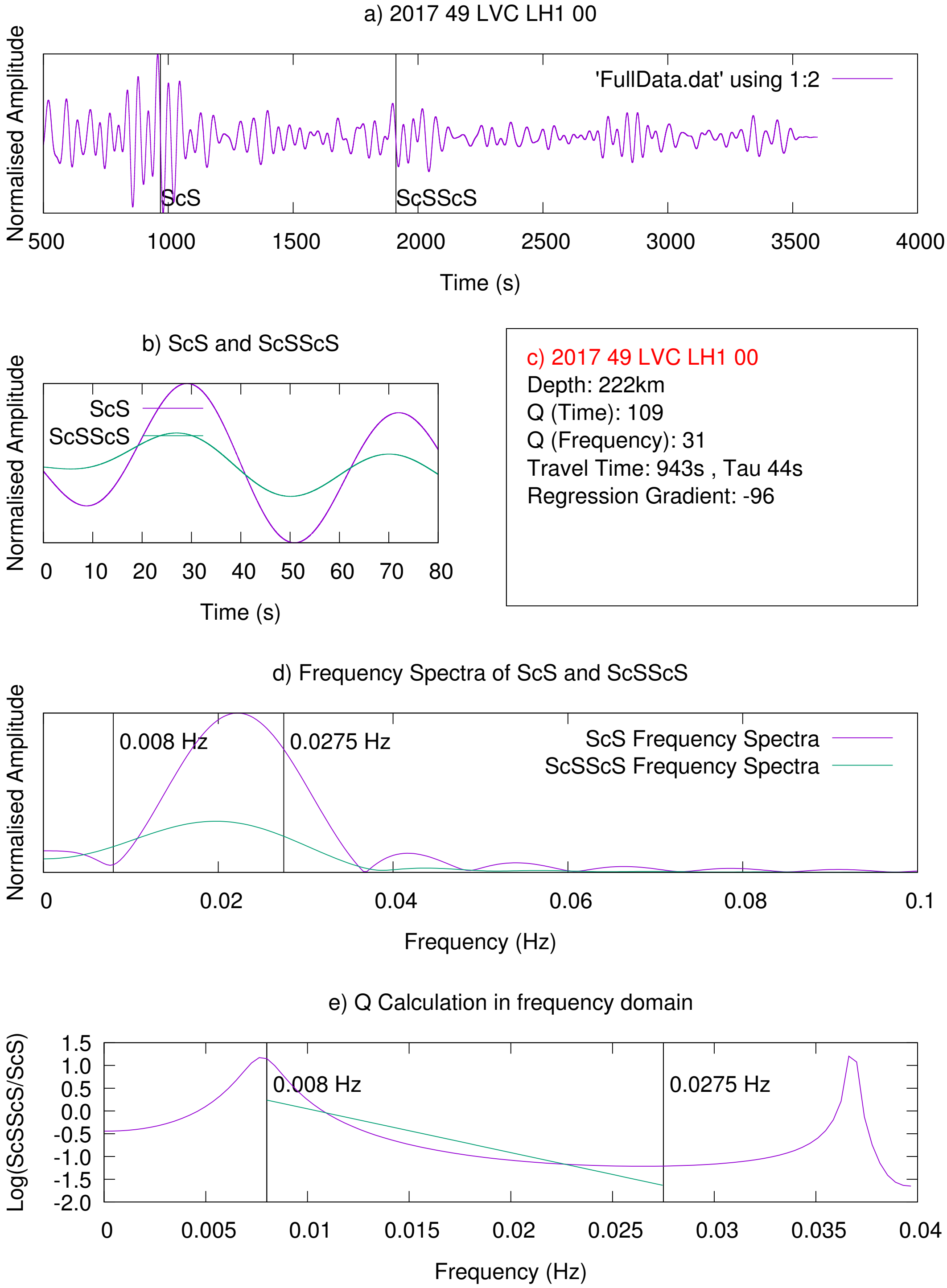

Figure A21: a) Seismogram after butterworth filtering and the locations of the ScS and ScSScS arrivals. b) 80 second ScS and ScSScS time windows plotted on top of eachother. c) Year and Day number (Normal Date: 10/10/2017), Station Name, Component, Instrument, Event depth, Q(time), Q(Frequency), time difference between ScS and ScSScS and the value of the frequency spectra gradient. d) The frequency spectra of the ScS and ScSScS phases and e) Graph upon which spectral gradient is calculated. The green line shows the line fitted through the data.

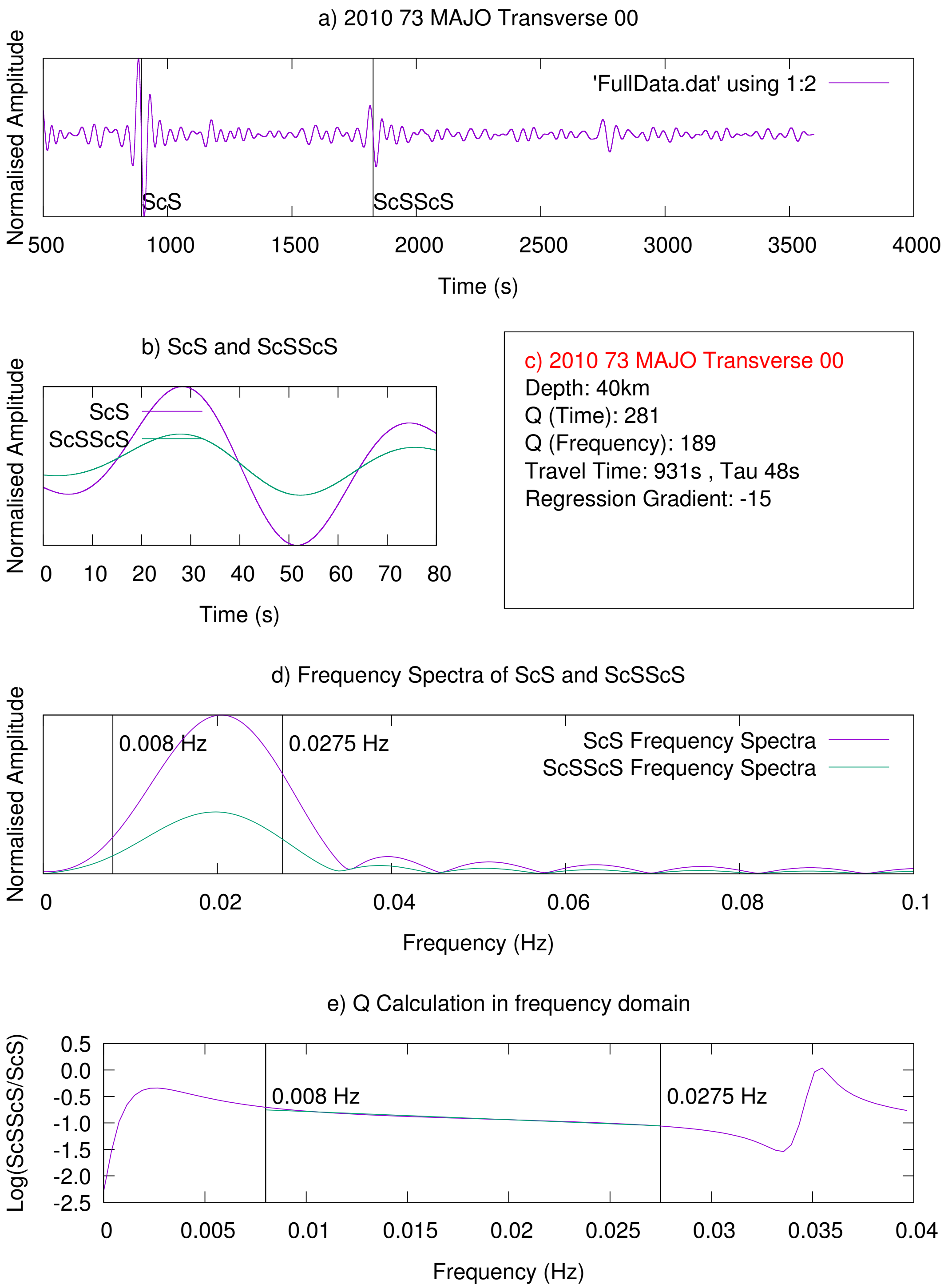

Figure A22: a) Seismogram after butterworth filtering and the locations of the ScS and ScSScS arrivals. b) 80 second ScS and ScSScS time windows plotted on top of eachother. c) Year and Day number (Normal Date: 14/03/2010), Station Name, Component, Instrument, Event depth, Q(time), Q(Frequency), time difference between ScS and ScSScS and the value of the frequency spectra gradient. d) The frequency spectra of the ScS and ScSScS phases and e) Graph upon which spectral gradient is calculated. The green line shows the line fitted through the data.

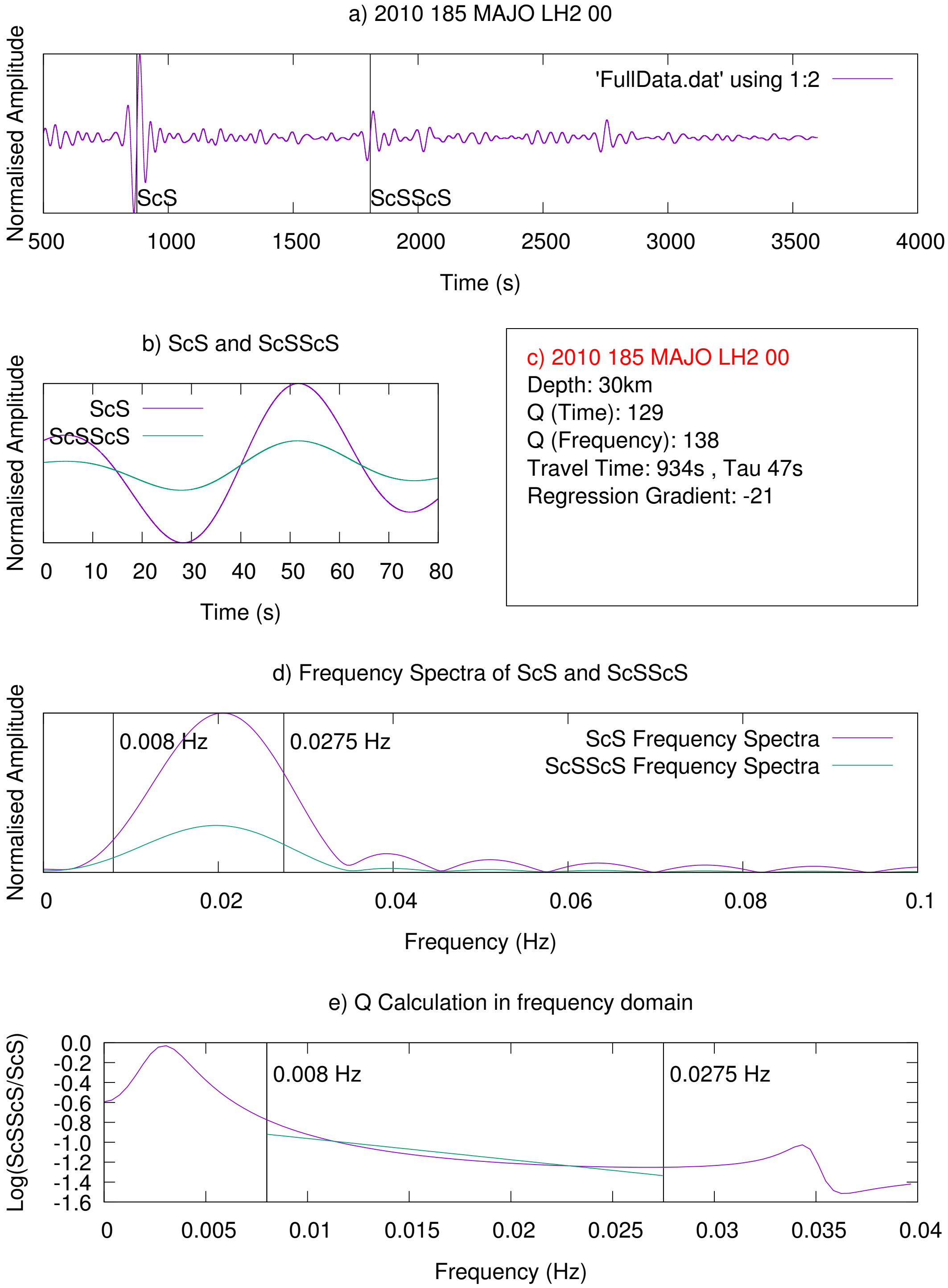

Figure A23: a) Seismogram after butterworth filtering and the locations of the ScS and ScSScS arrivals. b) 80 second ScS and ScSScS time windows plotted on top of eachother. c) Year and Day number (Normal Date: 04/07/2010), Station Name, Component, Instrument, Event depth, Q(time), Q(Frequency), time difference between ScS and ScSScS and the value of the frequency spectra gradient. d) The frequency spectra of the ScS and ScSScS phases and e) Graph upon which spectral gradient is calculated. The green line shows the line fitted through the data.

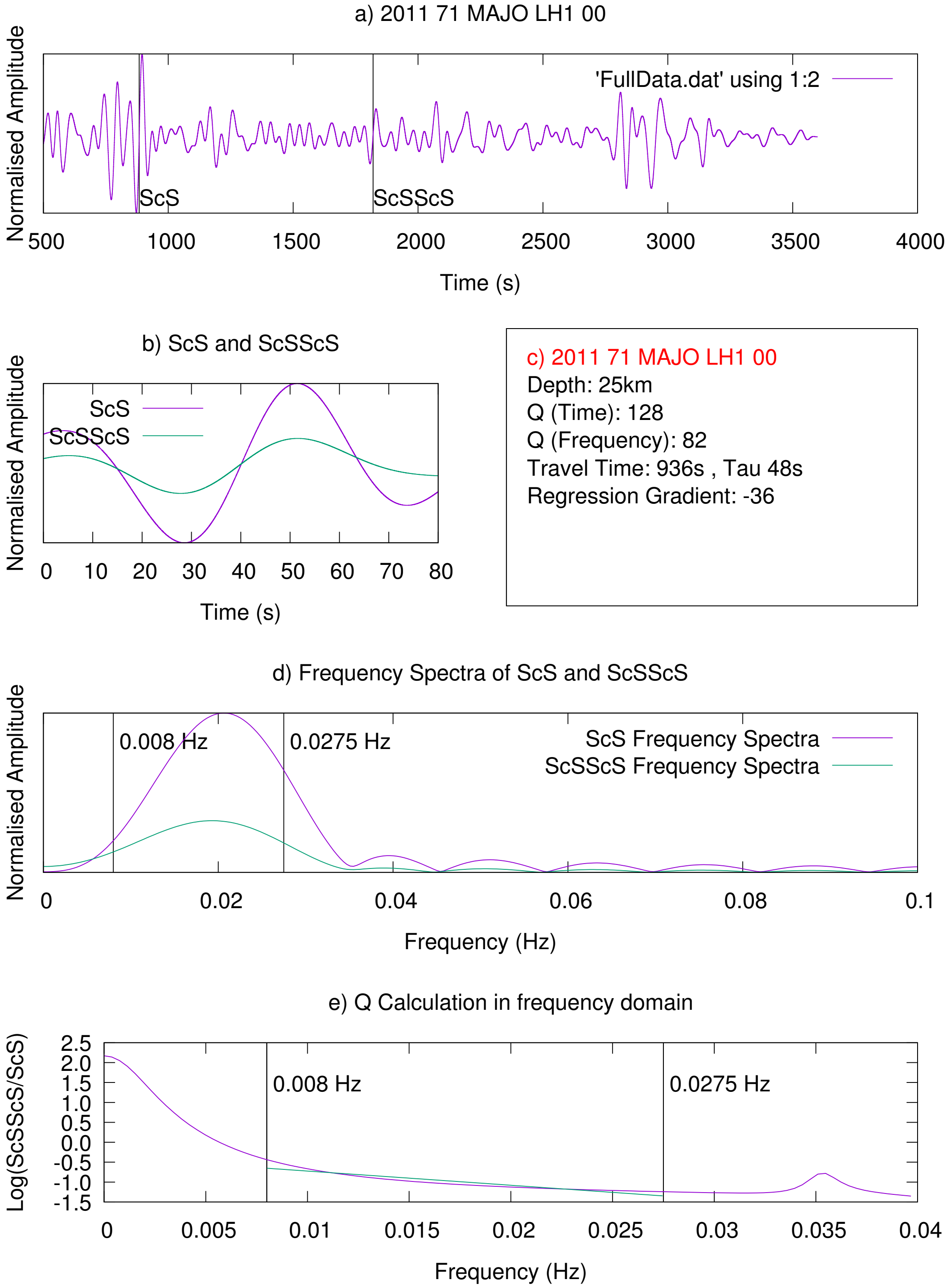

Figure A24: a) Seismogram after butterworth filtering and the locations of the ScS and ScSScS arrivals. b) 80 second ScS and ScSScS time windows plotted on top of eachother. c) Year and Day number (Normal Date: 12/03/2011), Station Name, Component, Instrument, Event depth, Q(time), Q(Frequency), time difference between ScS and ScSScS and the value of the frequency spectra gradient. d) The frequency spectra of the ScS and ScSScS phases and e) Graph upon which spectral gradient is calculated. The green line shows the line fitted through the data.

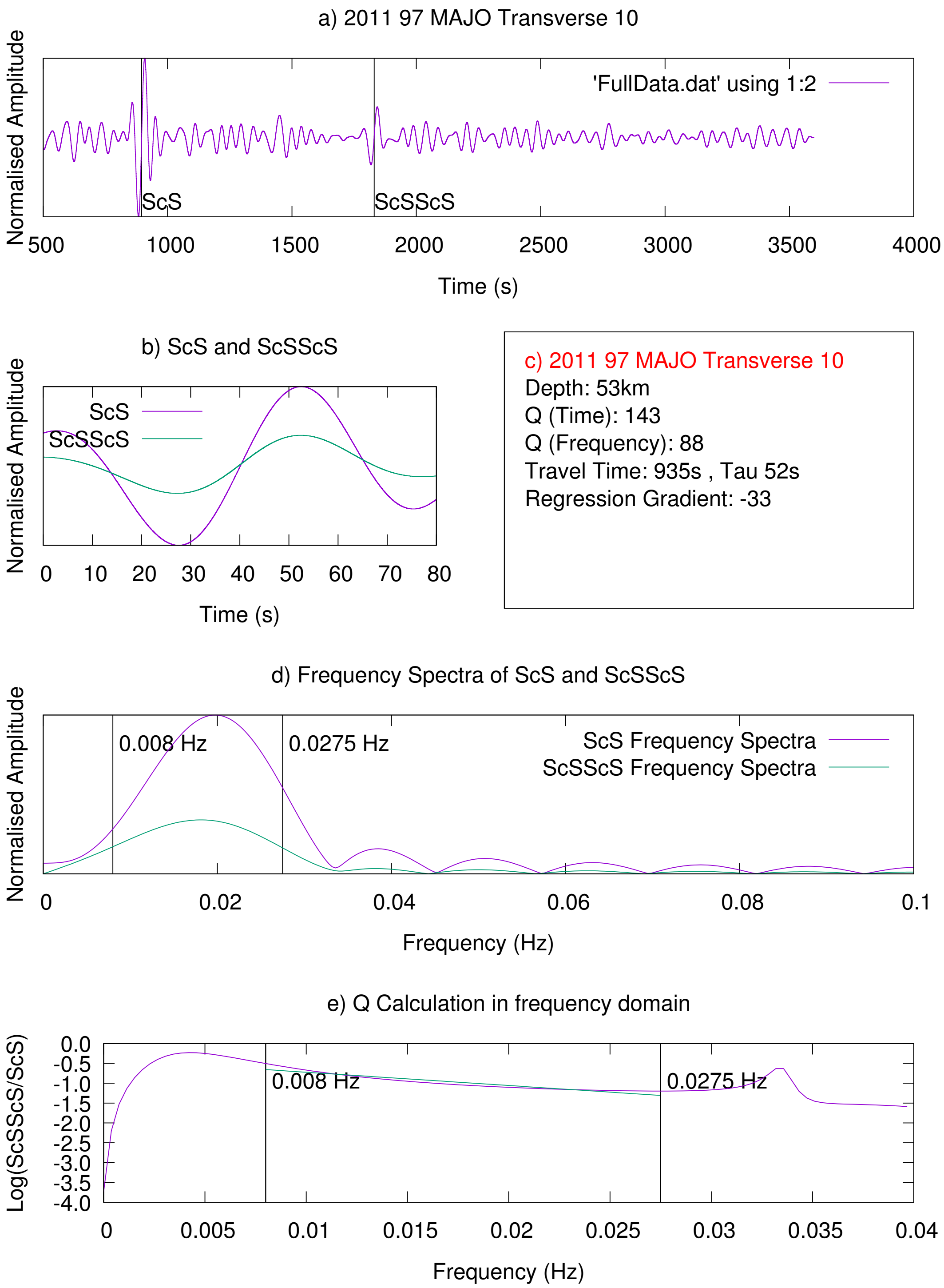

Figure A25: a) Seismogram after butterworth filtering and the locations of the ScS and ScSScS arrivals. b) 80 second ScS and ScSScS time windows plotted on top of eachother. c) Year and Day number (Normal Date: 07/04/2011), Station Name, Component, Instrument, Event depth, Q(time), Q(Frequency), time difference between ScS and ScSScS and the value of the frequency spectra gradient. d) The frequency spectra of the ScS and ScSScS phases and e) Graph upon which spectral gradient is calculated. The green line shows the line fitted through the data.

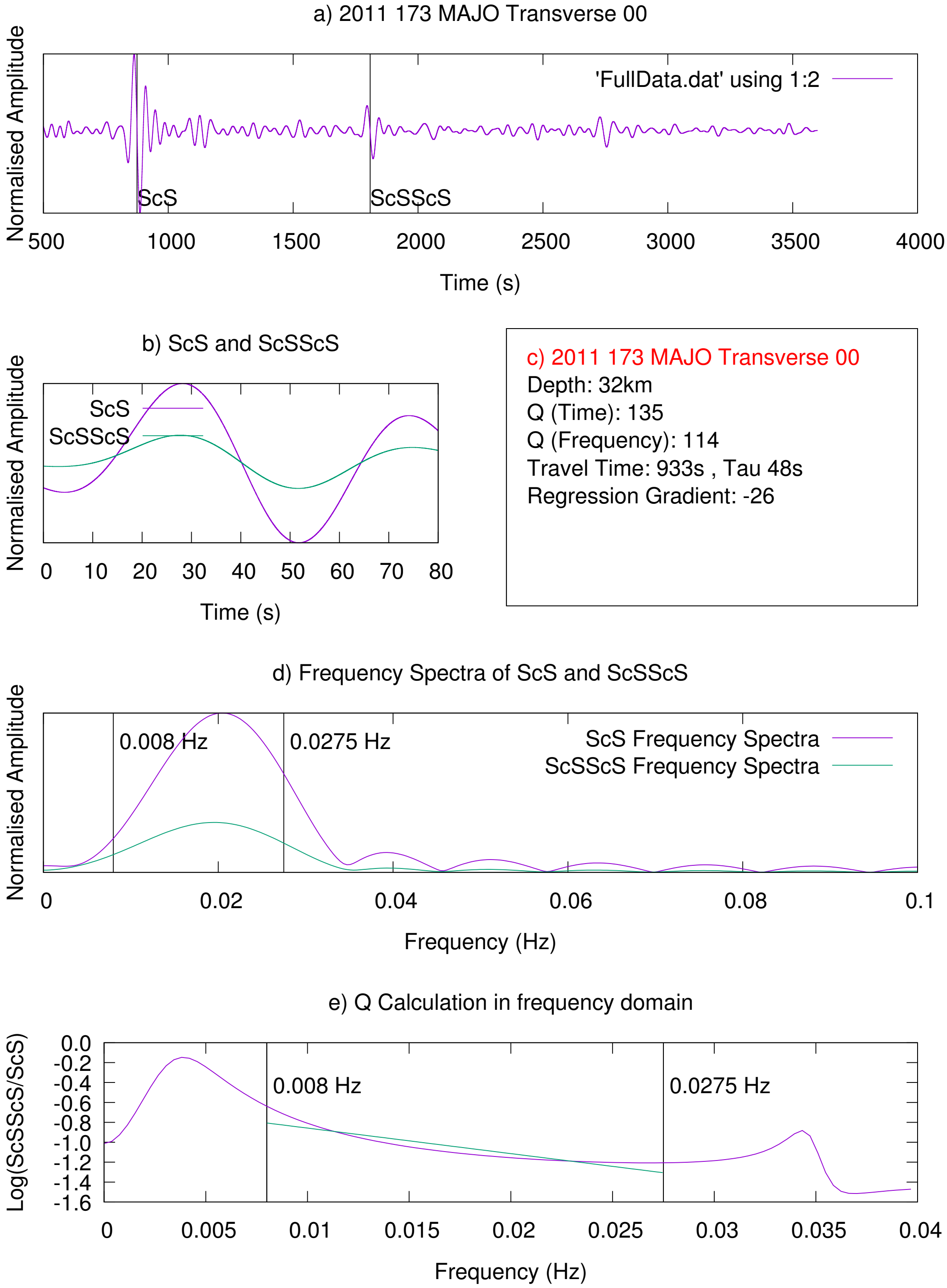

Figure A26: a) Seismogram after butterworth filtering and the locations of the ScS and ScSScS arrivals. b) 80 second ScS and ScSScS time windows plotted on top of eachother. c) Year and Day number (Normal Date: 22/06/2011), Station Name, Component, Instrument, Event depth, Q(time), Q(Frequency), time difference between ScS and ScSScS and the value of the frequency spectra gradient. d) The frequency spectra of the ScS and ScSScS phases and e) Graph upon which spectral gradient is calculated. The green line shows the line fitted through the data.

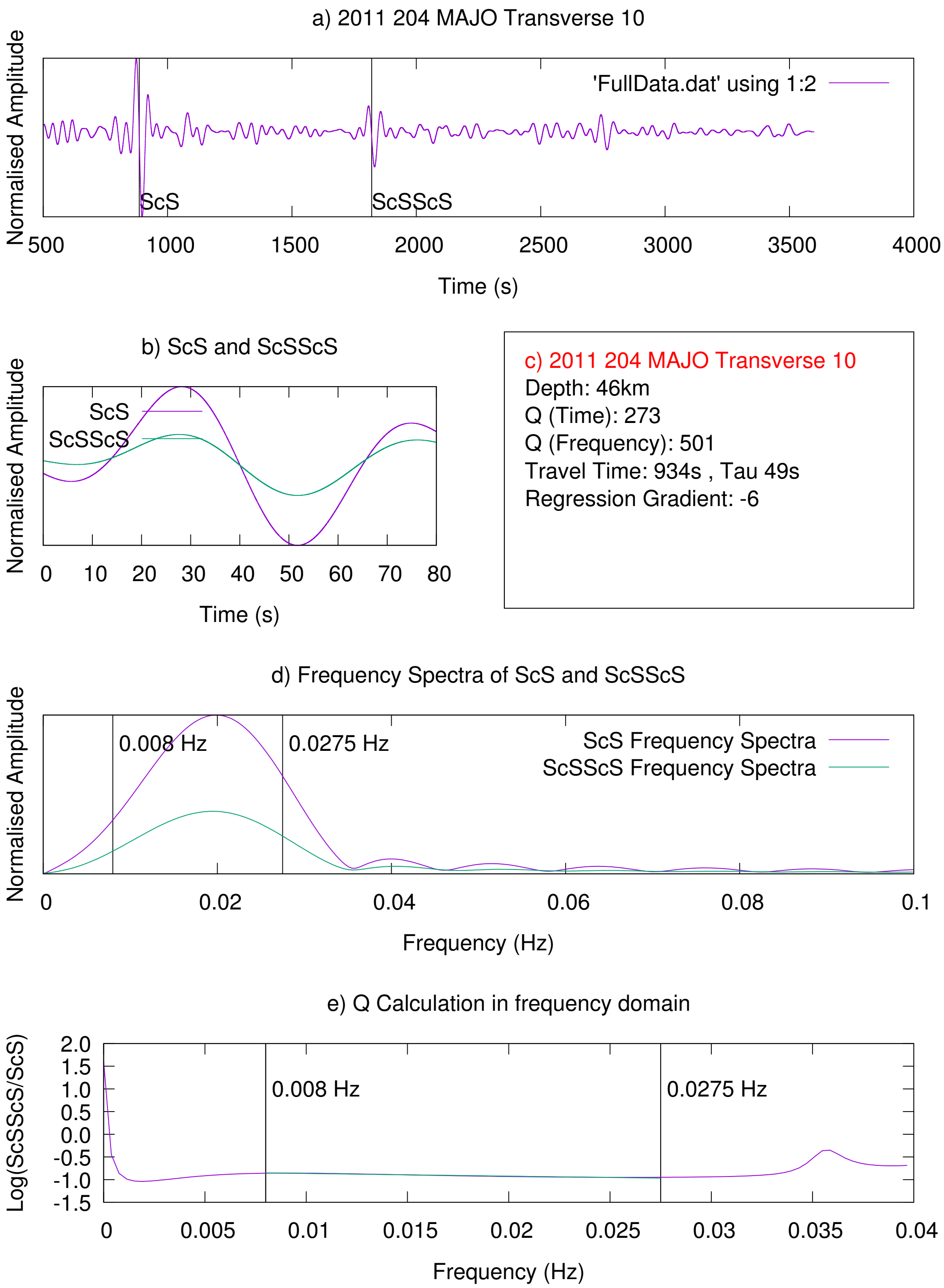

Figure A27: a) Seismogram after butterworth filtering and the locations of the ScS and ScSScS arrivals. b) 80 second ScS and ScSScS time windows plotted on top of eachother. c) Year and Day number (Normal Date: 23/07/2011), Station Name, Component, Instrument, Event depth, Q(time), Q(Frequency), time difference between ScS and ScSScS and the value of the frequency spectra gradient. d) The frequency spectra of the ScS and ScSScS phases and e) Graph upon which spectral gradient is calculated. The green line shows the line fitted through the data.

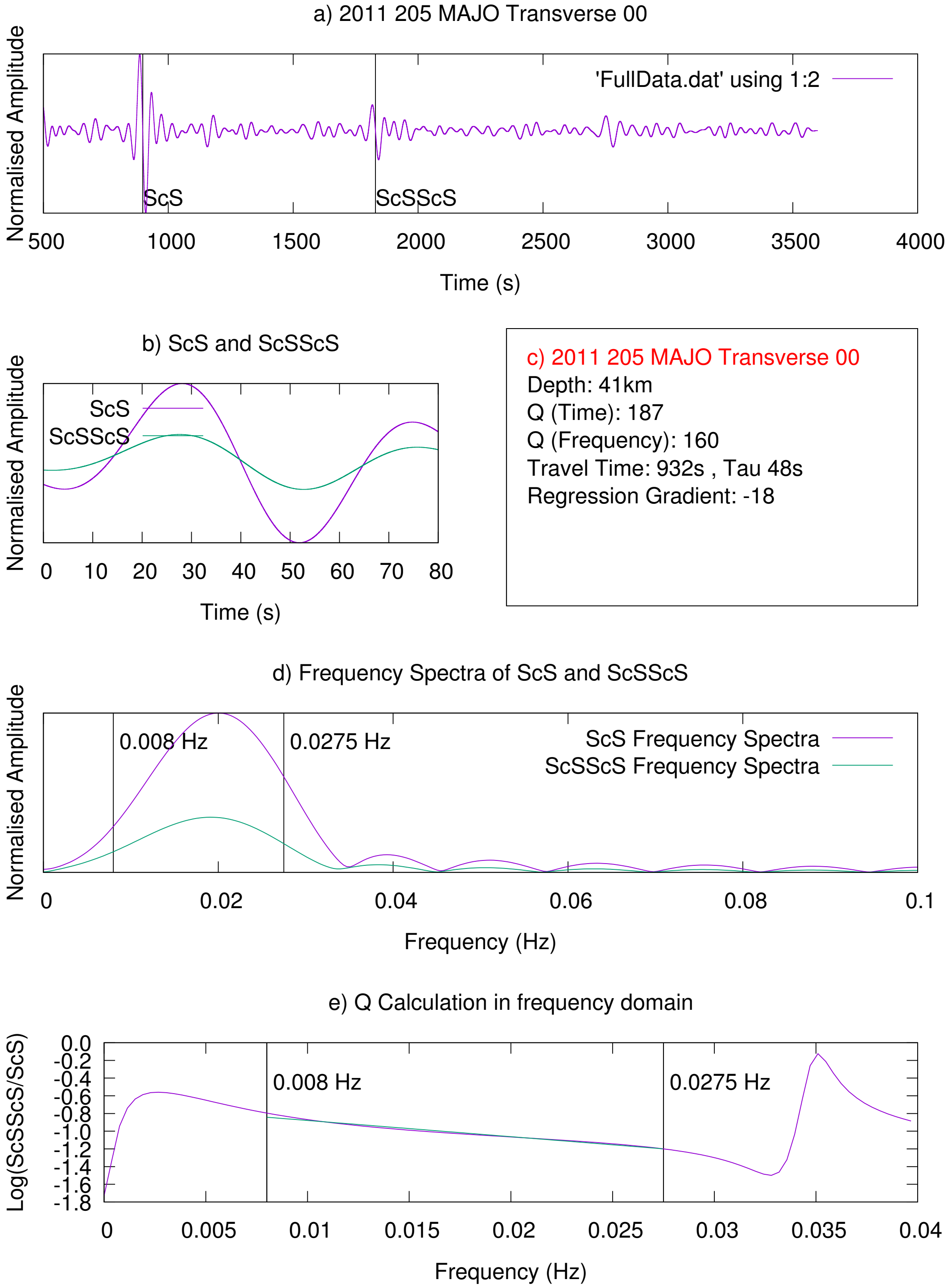

Figure A28: a) Seismogram after butterworth filtering and the locations of the ScS and ScSScS arrivals. b) 80 second ScS and ScSScS time windows plotted on top of eachother. c) Year and Day number (Normal Date: 24/07/2011), Station Name, Component, Instrument, Event depth, Q(time), Q(Frequency), time difference between ScS and ScSScS and the value of the frequency spectra gradient. d) The frequency spectra of the ScS and ScSScS phases and e) Graph upon which spectral gradient is calculated. The green line shows the line fitted through the data.

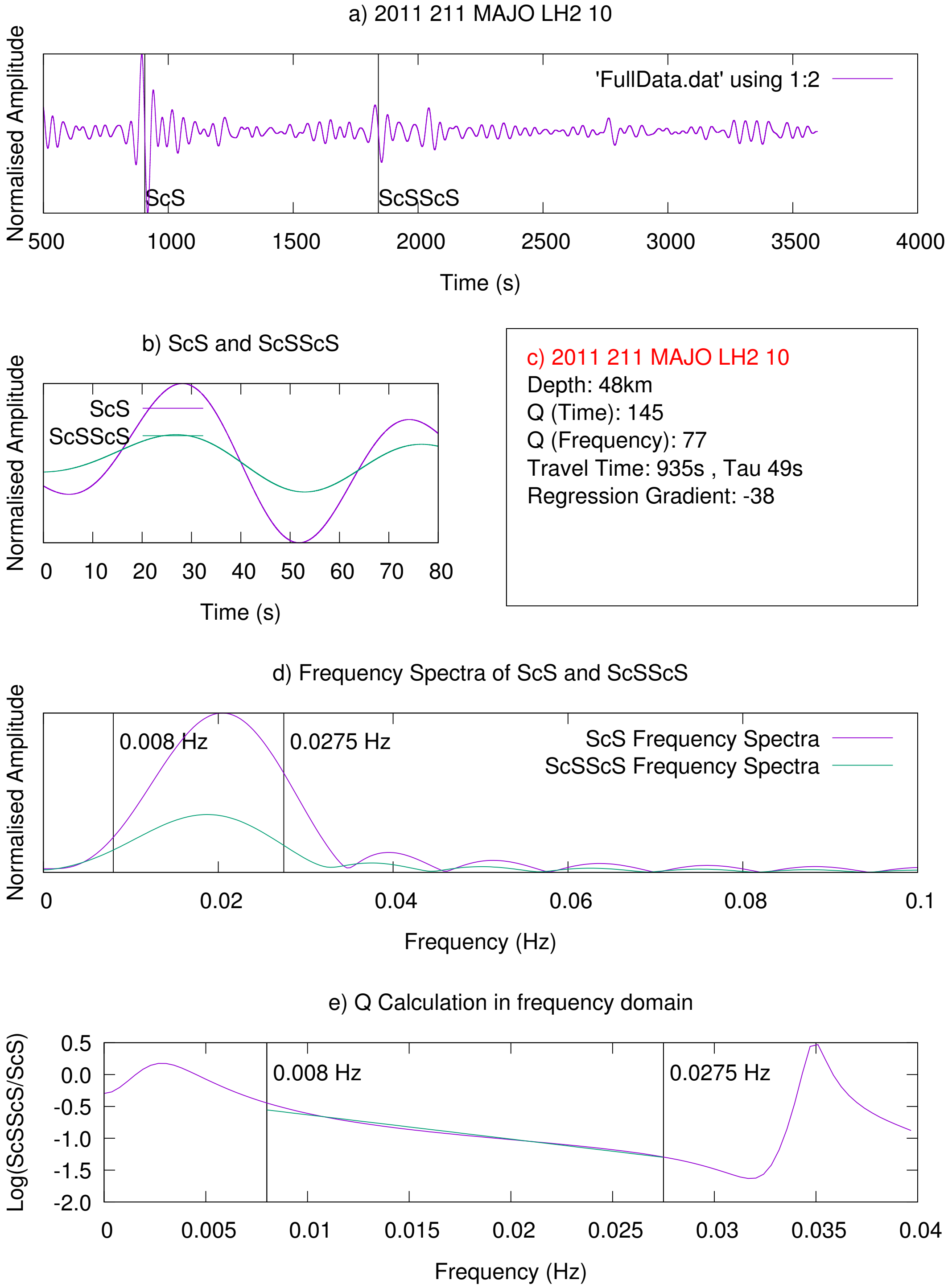

Figure A29: a) Seismogram after butterworth filtering and the locations of the ScS and ScSScS arrivals. b) 80 second ScS and ScSScS time windows plotted on top of eachother. c) Year and Day number (Normal Date: 30/07/2011), Station Name, Component, Instrument, Event depth, Q(time), Q(Frequency), time difference between ScS and ScSScS and the value of the frequency spectra gradient. d) The frequency spectra of the ScS and ScSScS phases and e) Graph upon which spectral gradient is calculated. The green line shows the line fitted through the data.

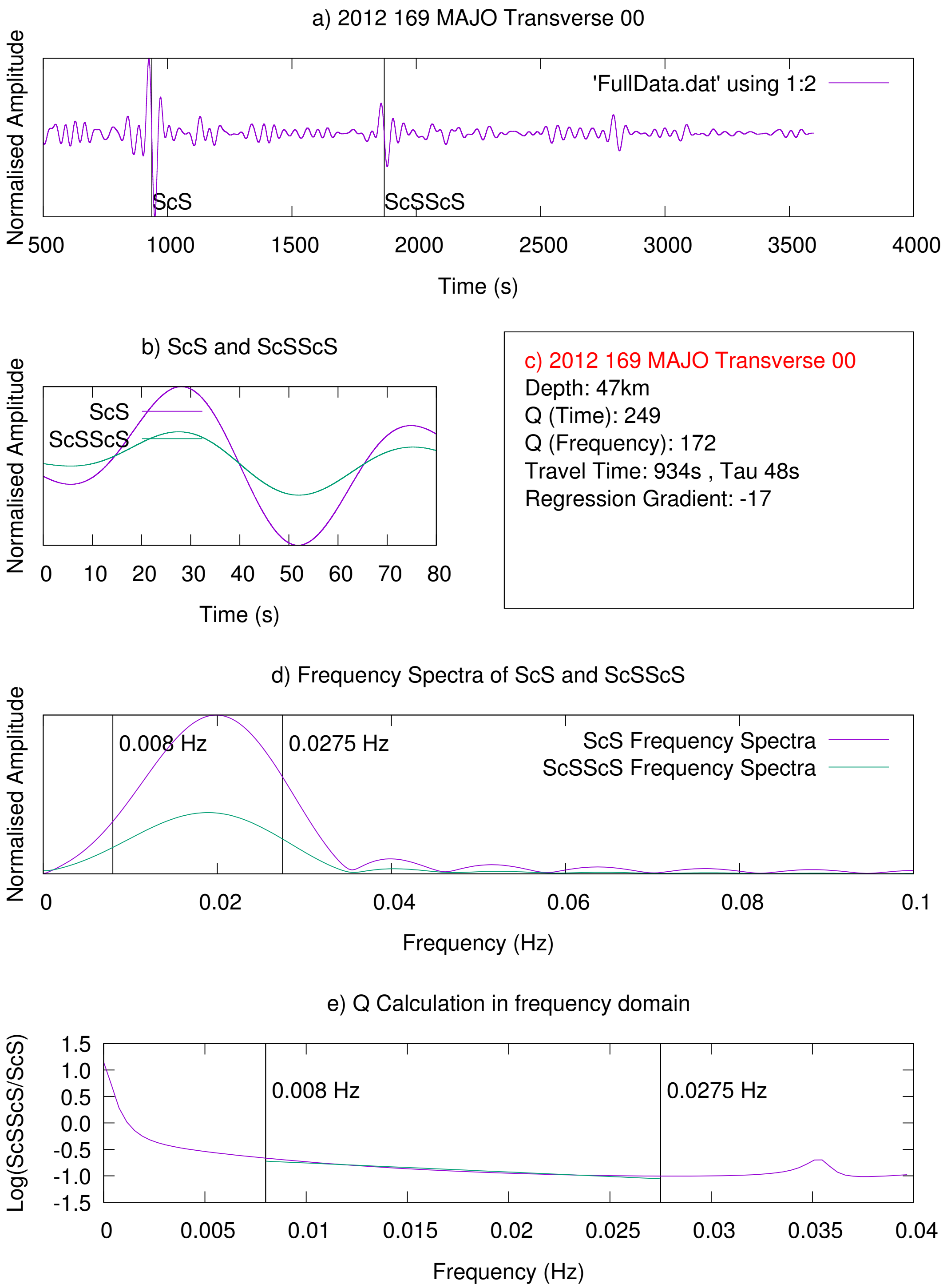

Figure A30: a) Seismogram after butterworth filtering and the locations of the ScS and ScSScS arrivals. b) 80 second ScS and ScSScS time windows plotted on top of eachother. c) Year and Day number (Normal Date: 17/06/2012), Station Name, Component, Instrument, Event depth, Q(time), Q(Frequency), time difference between ScS and ScSScS and the value of the frequency spectra gradient. d) The frequency spectra of the ScS and ScSScS phases and e) Graph upon which spectral gradient is calculated. The green line shows the line fitted through the data.

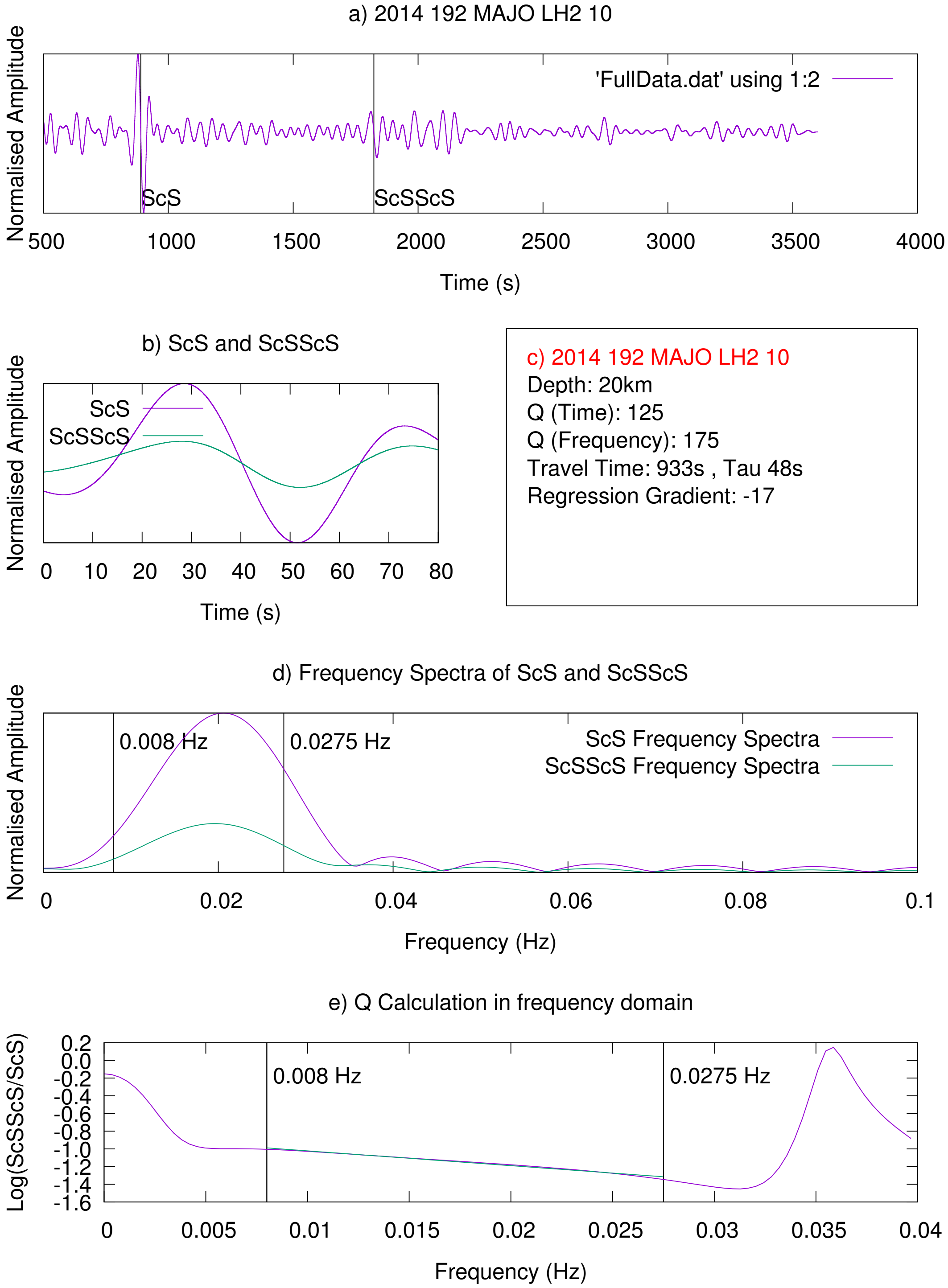

Figure A31: a) Seismogram after butterworth filtering and the locations of the ScS and ScSScS arrivals. b) 80 second ScS and ScSScS time windows plotted on top of eachother. c) Year and Day number (Normal Date: 11/07/2014), Station Name, Component, Instrument, Event depth, Q(time), Q(Frequency), time difference between ScS and ScSScS and the value of the frequency spectra gradient. d) The frequency spectra of the ScS and ScSScS phases and e) Graph upon which spectral gradient is calculated. The green line shows the line fitted through the data.

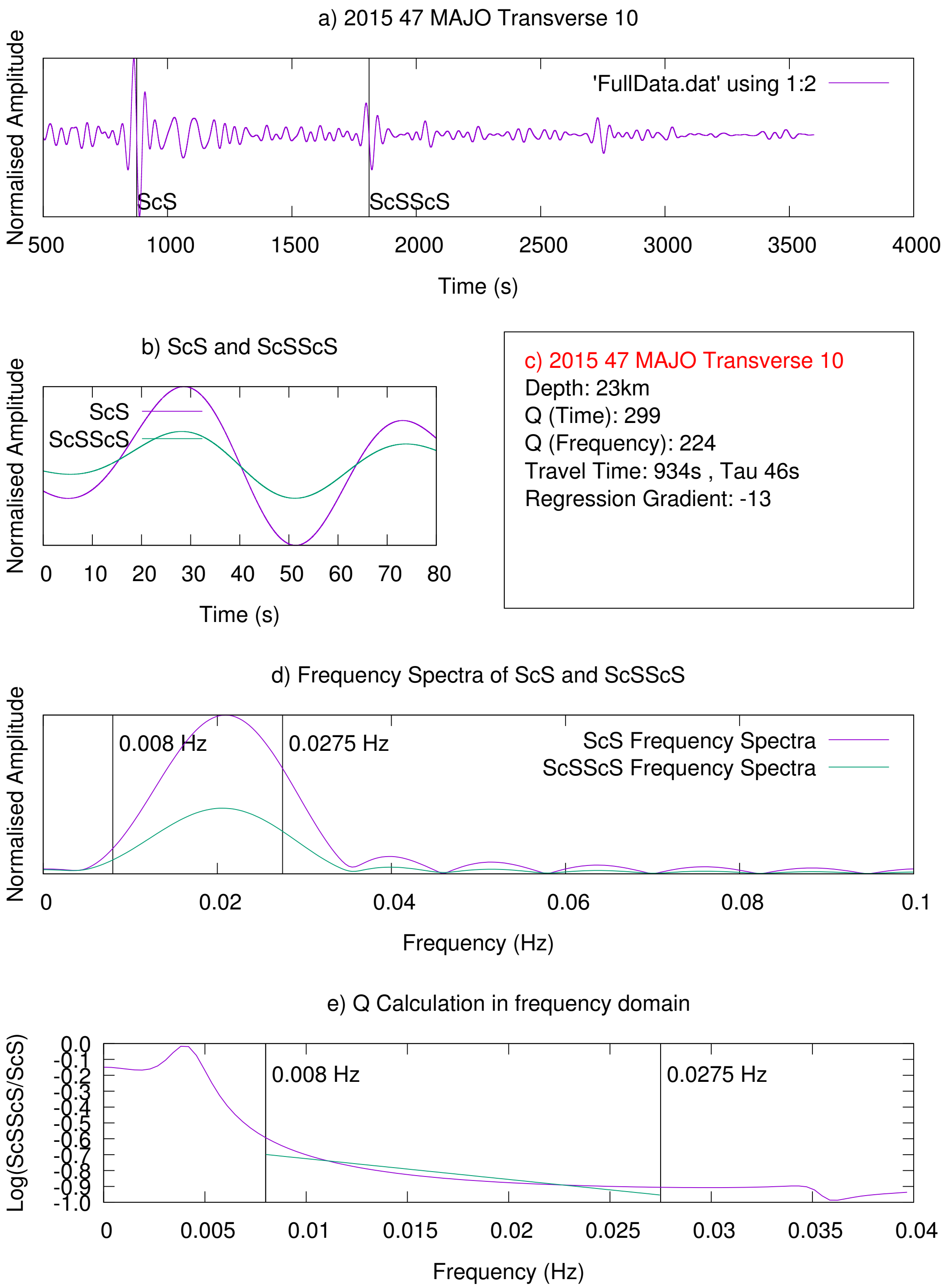

Figure A32: a) Seismogram after butterworth filtering and the locations of the ScS and ScSScS arrivals. b) 80 second ScS and ScSScS time windows plotted on top of eachother. c) Year and Day number (Normal Date: 16/02/2015), Station Name, Component, Instrument, Event depth, Q(time), Q(Frequency), time difference between ScS and ScSScS and the value of the frequency spectra gradient. d) The frequency spectra of the ScS and ScSScS phases and e) Graph upon which spectral gradient is calculated. The green line shows the line fitted through the data.

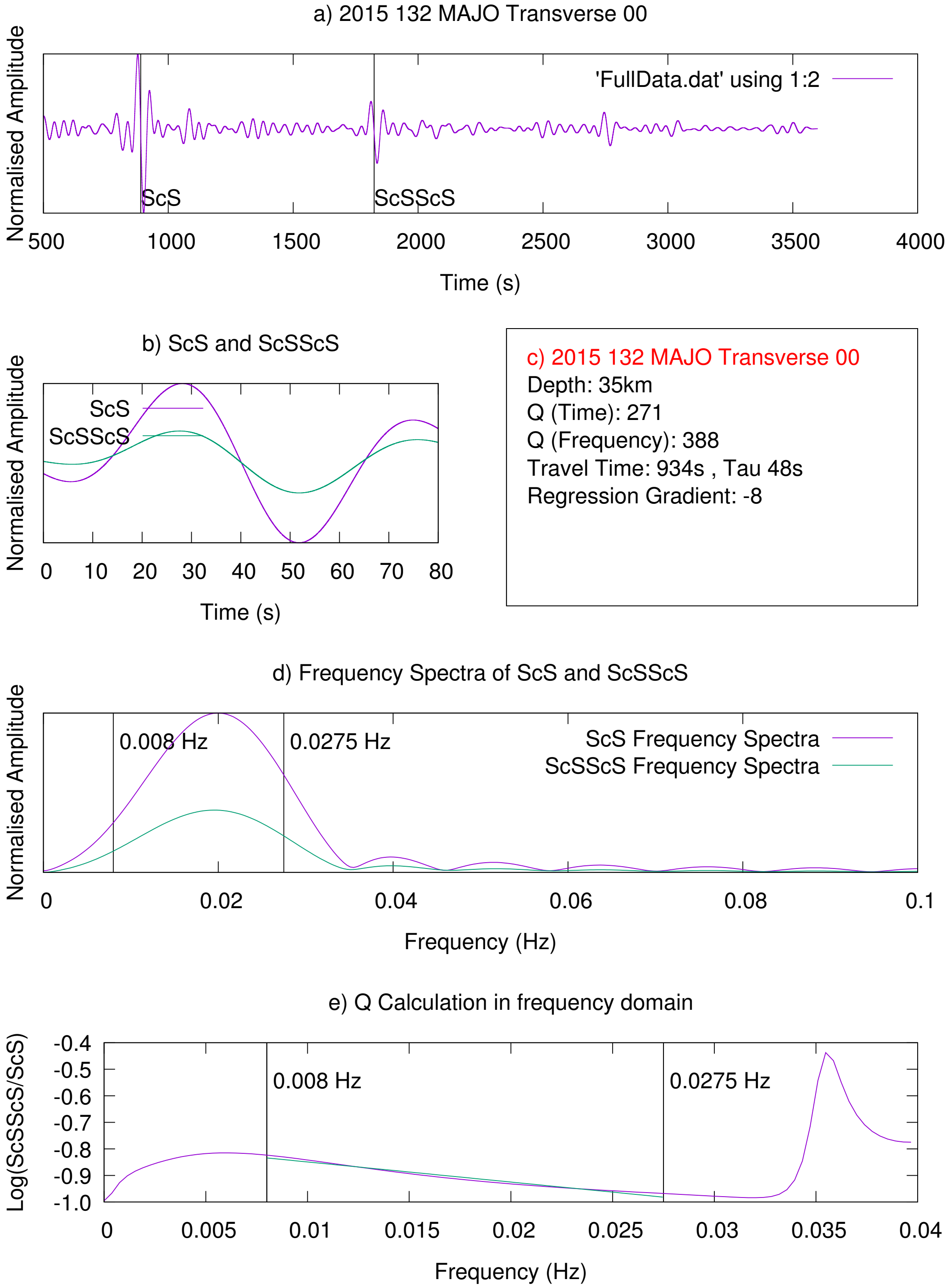

Figure A33: a) Seismogram after butterworth filtering and the locations of the ScS and ScSScS arrivals. b) 80 second ScS and ScSScS time windows plotted on top of eachother. c) Year and Day number (Normal Date: 12/05/2015), Station Name, Component, Instrument, Event depth, Q(time), Q(Frequency), time difference between ScS and ScSScS and the value of the frequency spectra gradient. d) The frequency spectra of the ScS and ScSScS phases and e) Graph upon which spectral gradient is calculated. The green line shows the line fitted through the data.

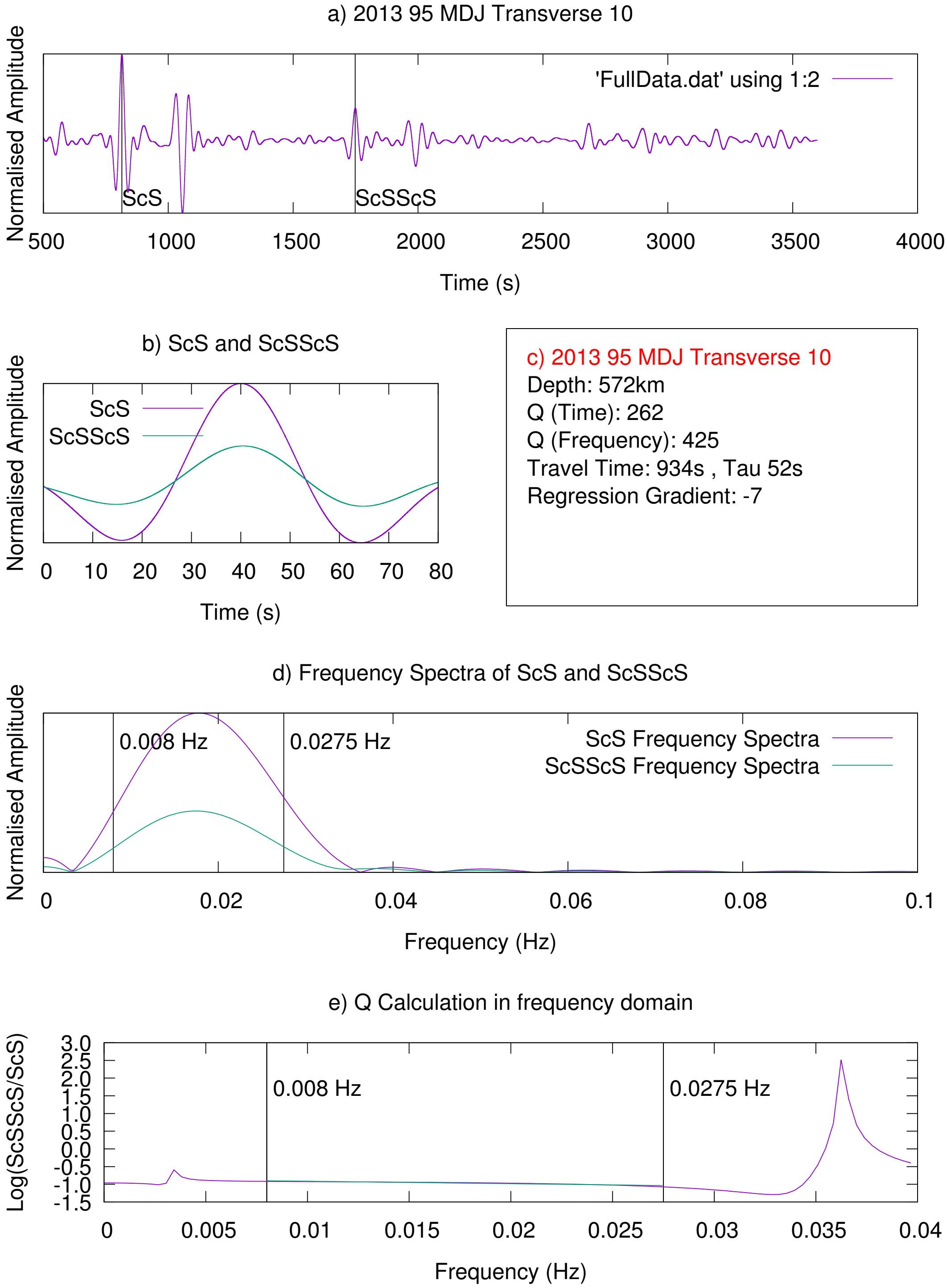

Figure A34: a) Seismogram after butterworth filtering and the locations of the ScS and ScSScS arrivals. b) 80 second ScS and ScSScS time windows plotted on top of eachother. c) Year and Day number (Normal Date: 05/04/2013), Station Name, Component, Instrument, Event depth, Q(time), Q(Frequency), time difference between ScS and ScSScS and the value of the frequency spectra gradient. d) The frequency spectra of the ScS and ScSScS phases and e) Graph upon which spectral gradient is calculated. The green line shows the line fitted through the data.

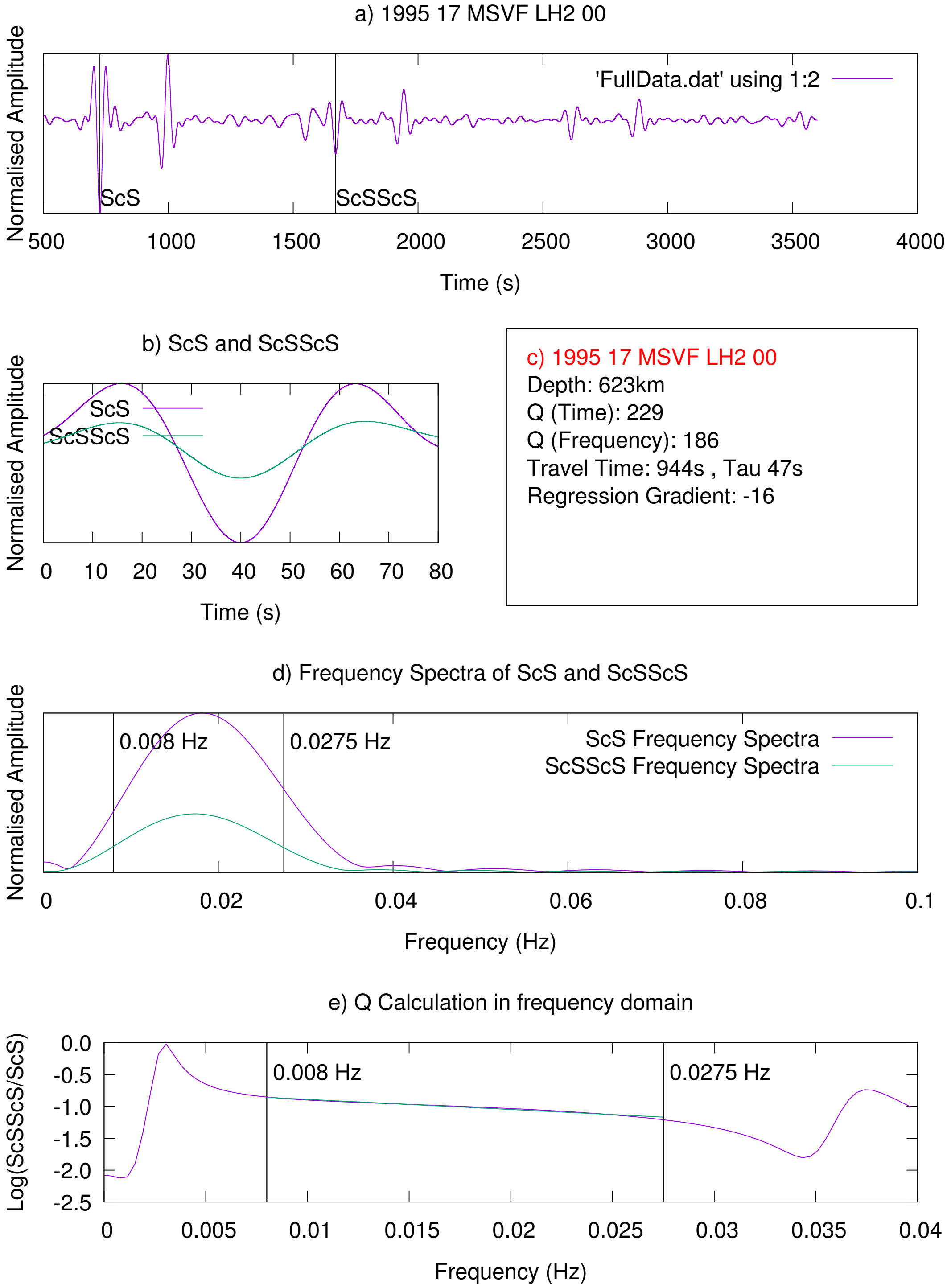

Figure A35: a) Seismogram after butterworth filtering and the locations of the ScS and ScSScS arrivals. b) 80 second ScS and ScSScS time windows plotted on top of eachother. c) Year and Day number (Normal Date: 17/01/1995), Station Name, Component, Instrument, Event depth, Q(time), Q(Frequency), time difference between ScS and ScSScS and the value of the frequency spectra gradient. d) The frequency spectra of the ScS and ScSScS phases and e) Graph upon which spectral gradient is calculated. The green line shows the line fitted through the data.

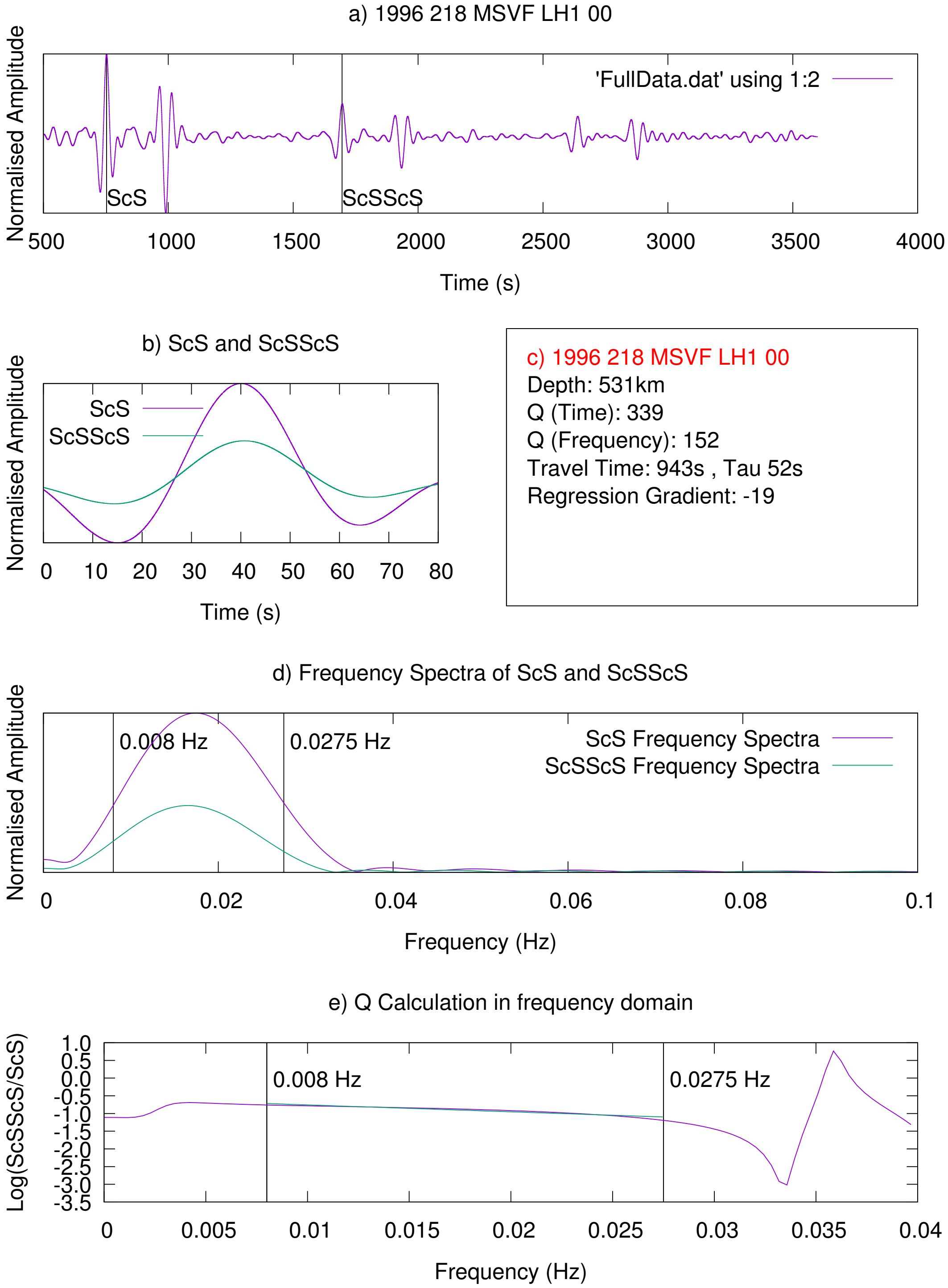

Figure A36: a) Seismogram after butterworth filtering and the locations of the ScS and ScSScS arrivals. b) 80 second ScS and ScSScS time windows plotted on top of eachother. c) Year and Day number (Normal Date: 05/08/1996), Station Name, Component, Instrument, Event depth, Q(time), Q(Frequency), time difference between ScS and ScSScS and the value of the frequency spectra gradient. d) The frequency spectra of the ScS and ScSScS phases and e) Graph upon which spectral gradient is calculated. The green line shows the line fitted through the data.

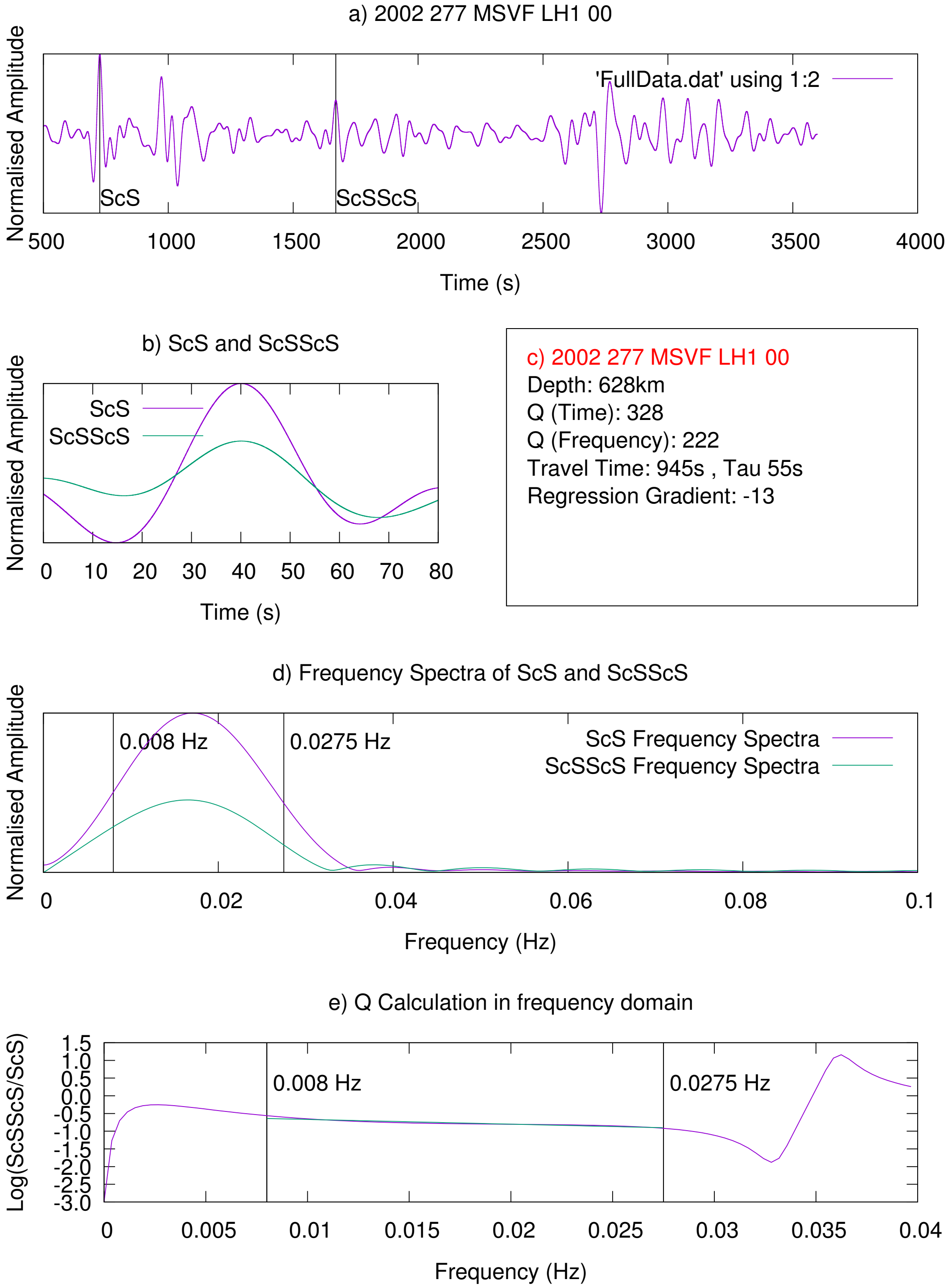

Figure A37: a) Seismogram after butterworth filtering and the locations of the ScS and ScSScS arrivals. b) 80 second ScS and ScSScS time windows plotted on top of eachother. c) Year and Day number (Normal Date: 04/10/2002), Station Name, Component, Instrument, Event depth, Q(time), Q(Frequency), time difference between ScS and ScSScS and the value of the frequency spectra gradient. d) The frequency spectra of the ScS and ScSScS phases and e) Graph upon which spectral gradient is calculated. The green line shows the line fitted through the data.

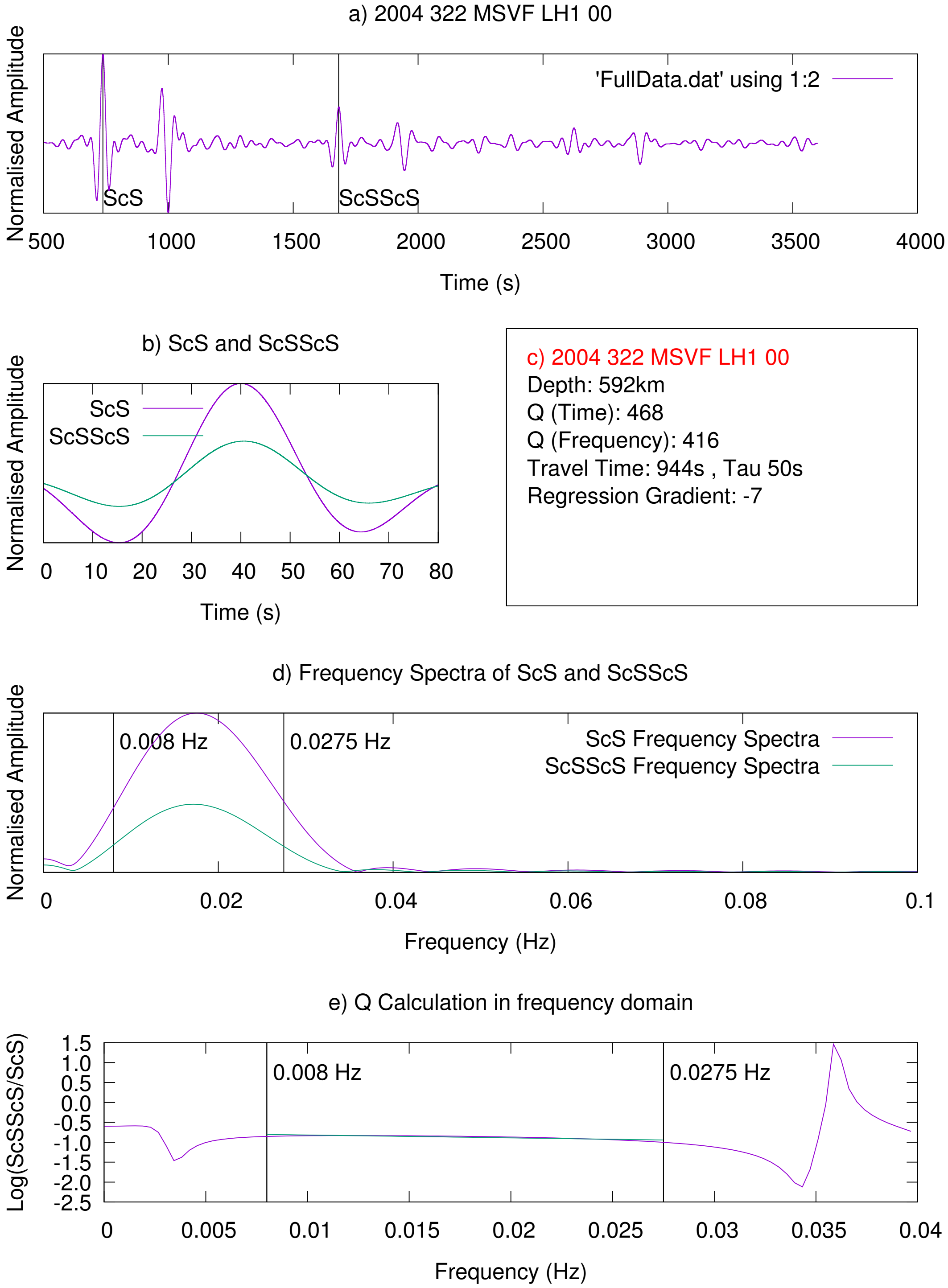

Figure A38: a) Seismogram after butterworth filtering and the locations of the ScS and ScSScS arrivals. b) 80 second ScS and ScSScS time windows plotted on top of eachother. c) Year and Day number (Normal Date: 17/11/2004), Station Name, Component, Instrument, Event depth, Q(time), Q(Frequency), time difference between ScS and ScSScS and the value of the frequency spectra gradient. d) The frequency spectra of the ScS and ScSScS phases and e) Graph upon which spectral gradient is calculated. The green line shows the line fitted through the data.

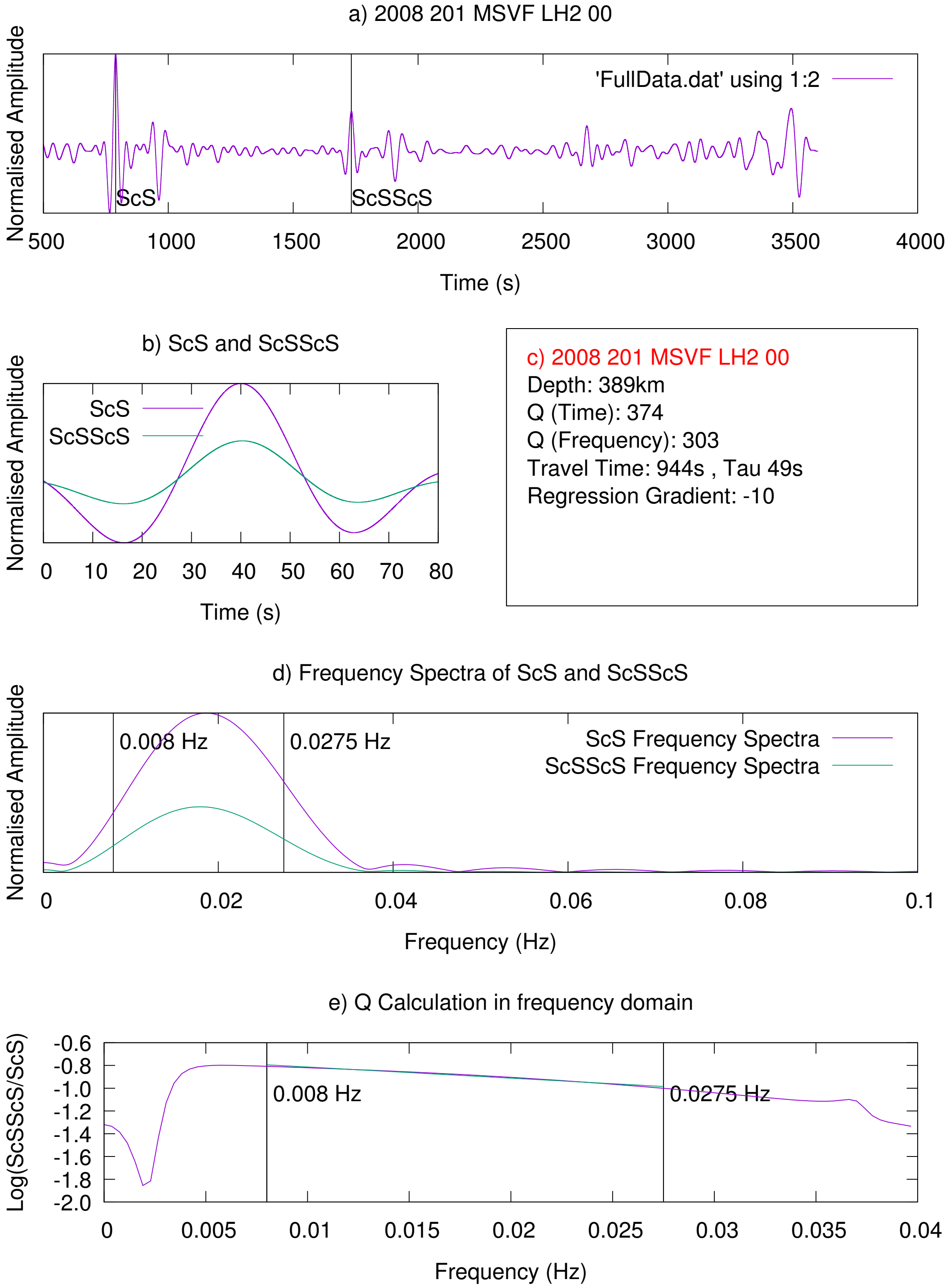

Figure A39: a) Seismogram after butterworth filtering and the locations of the ScS and ScSScS arrivals. b) 80 second ScS and ScSScS time windows plotted on top of eachother. c) Year and Day number (Normal Date: 19/07/2008), Station Name, Component, Instrument, Event depth, Q(time), Q(Frequency), time difference between ScS and ScSScS and the value of the frequency spectra gradient. d) The frequency spectra of the ScS and ScSScS phases and e) Graph upon which spectral gradient is calculated. The green line shows the line fitted through the data.

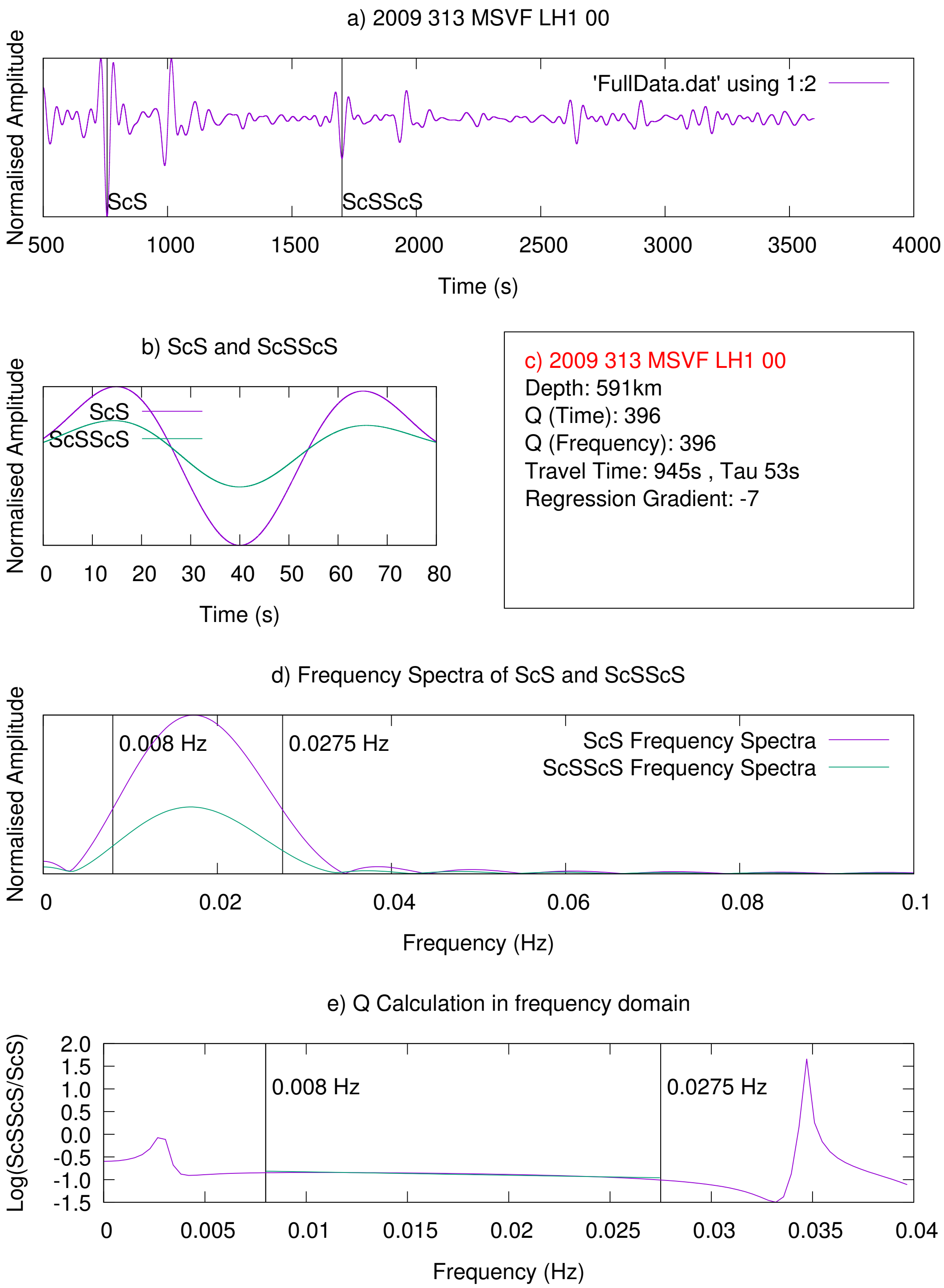

Figure A40: a) Seismogram after butterworth filtering and the locations of the ScS and ScSScS arrivals. b) 80 second ScS and ScSScS time windows plotted on top of eachother. c) Year and Day number (Normal Date: 09/11/2009), Station Name, Component, Instrument, Event depth, Q(time), Q(Frequency), time difference between ScS and ScSScS and the value of the frequency spectra gradient. d) The frequency spectra of the ScS and ScSScS phases and e) Graph upon which spectral gradient is calculated. The green line shows the line fitted through the data.

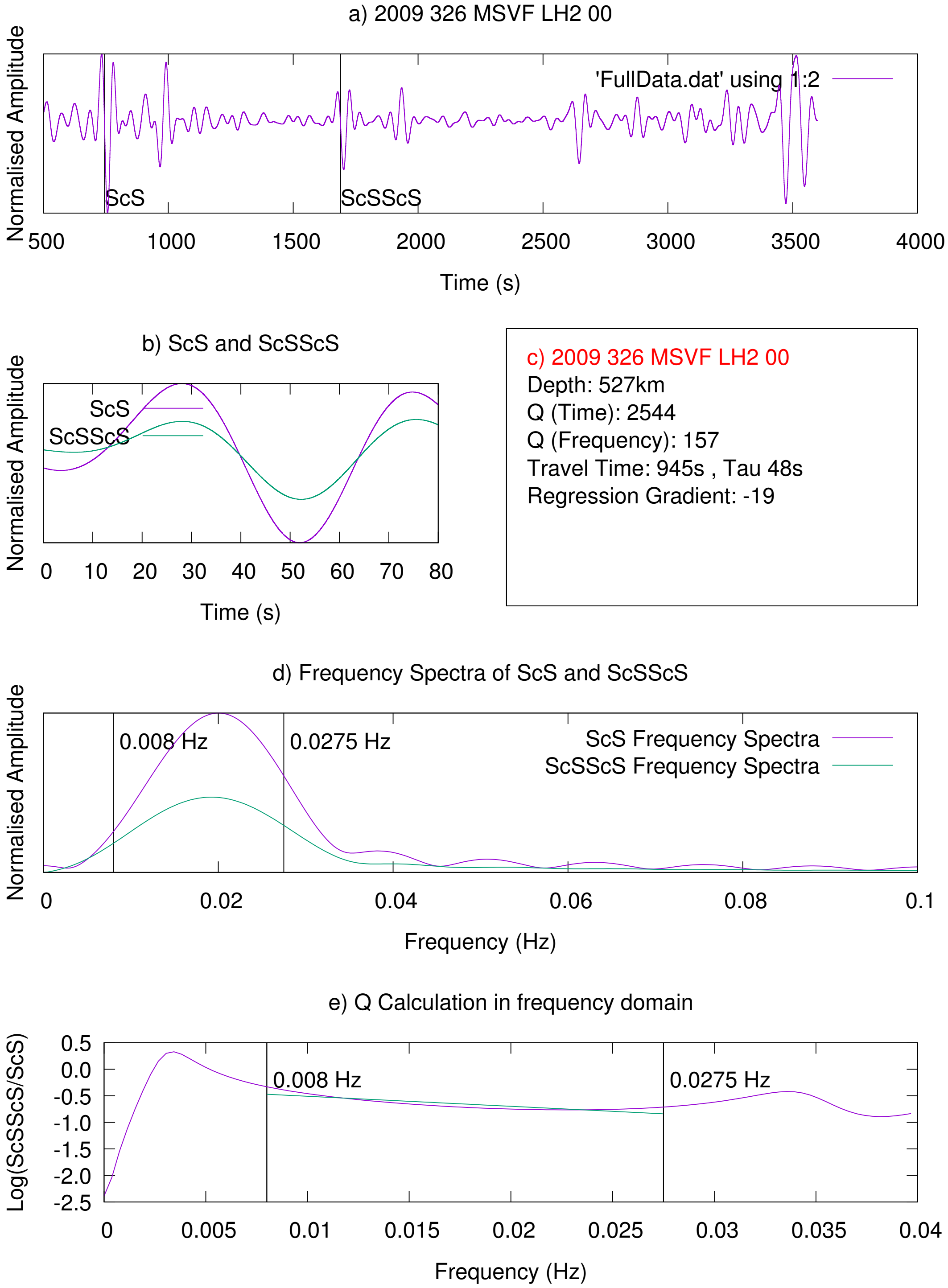

Figure A41: a) Seismogram after butterworth filtering and the locations of the ScS and ScSScS arrivals. b) 80 second ScS and ScSScS time windows plotted on top of eachother. c) Year and Day number (Normal Date: 22/11/2009), Station Name, Component, Instrument, Event depth, Q(time), Q(Frequency), time difference between ScS and ScSScS and the value of the frequency spectra gradient. d) The frequency spectra of the ScS and ScSScS phases and e) Graph upon which spectral gradient is calculated. The green line shows the line fitted through the data.

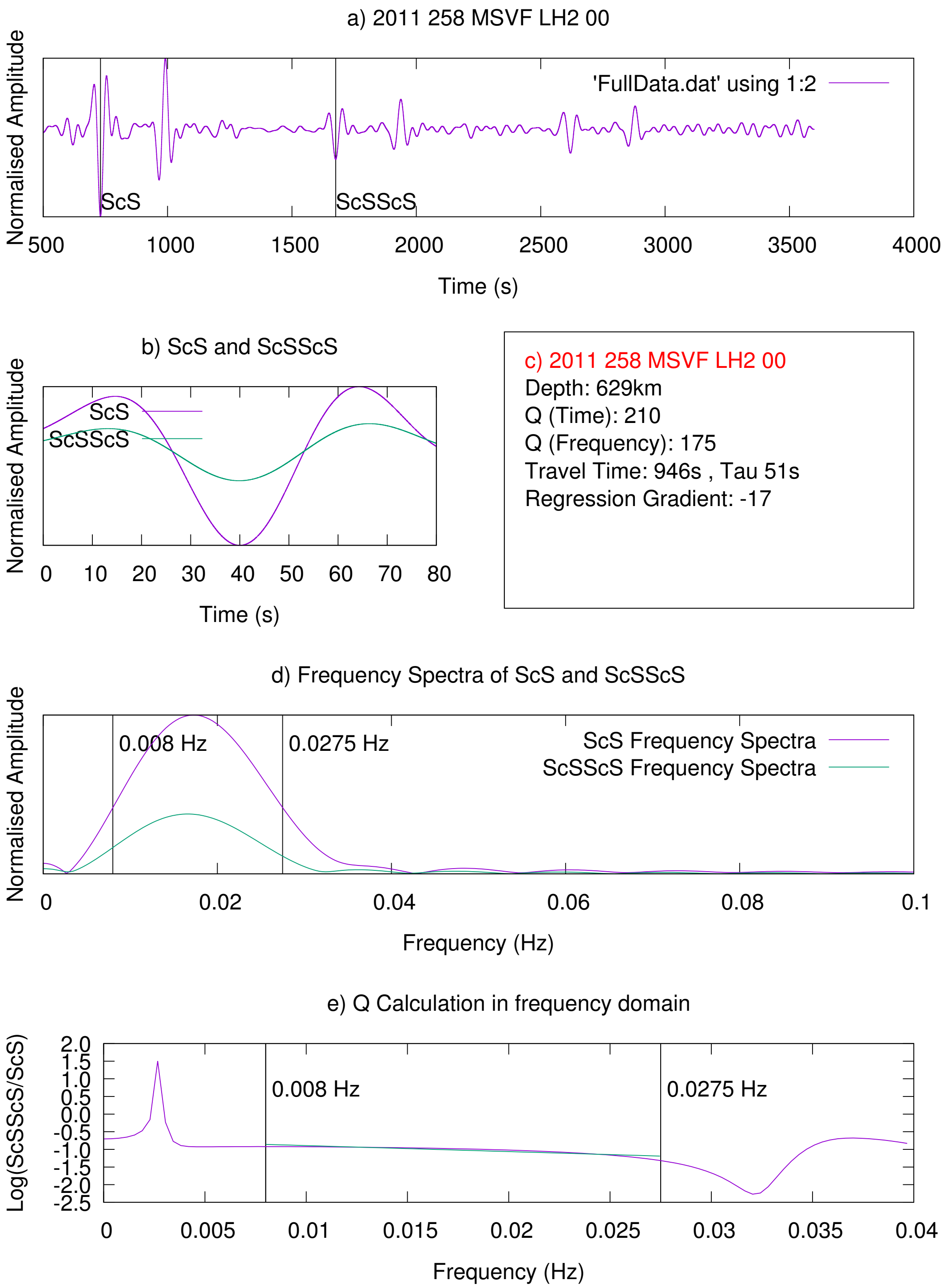

Figure A42: a) Seismogram after butterworth filtering and the locations of the ScS and ScSScS arrivals. b) 80 second ScS and ScSScS time windows plotted on top of eachother. c) Year and Day number (Normal Date: 15/09/2011), Station Name, Component, Instrument, Event depth, Q(time), Q(Frequency), time difference between ScS and ScSScS and the value of the frequency spectra gradient. d) The frequency spectra of the ScS and ScSScS phases and e) Graph upon which spectral gradient is calculated. The green line shows the line fitted through the data.

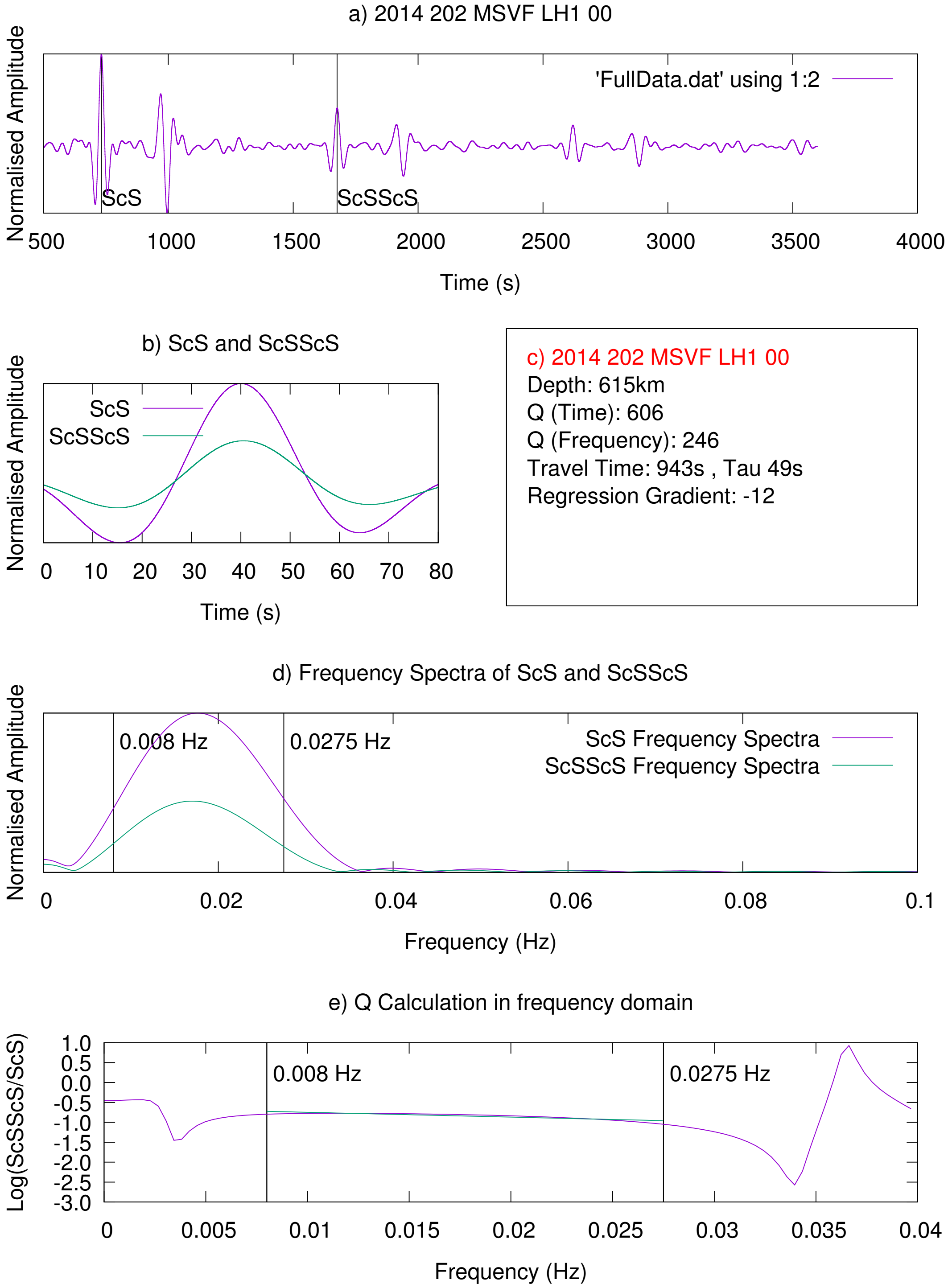

Figure A43: a) Seismogram after butterworth filtering and the locations of the ScS and ScSScS arrivals. b) 80 second ScS and ScSScS time windows plotted on top of eachother. c) Year and Day number (Normal Date: 21/07/2014), Station Name, Component, Instrument, Event depth, Q(time), Q(Frequency), time difference between ScS and ScSScS and the value of the frequency spectra gradient. d) The frequency spectra of the ScS and ScSScS phases and e) Graph upon which spectral gradient is calculated. The green line shows the line fitted through the data.

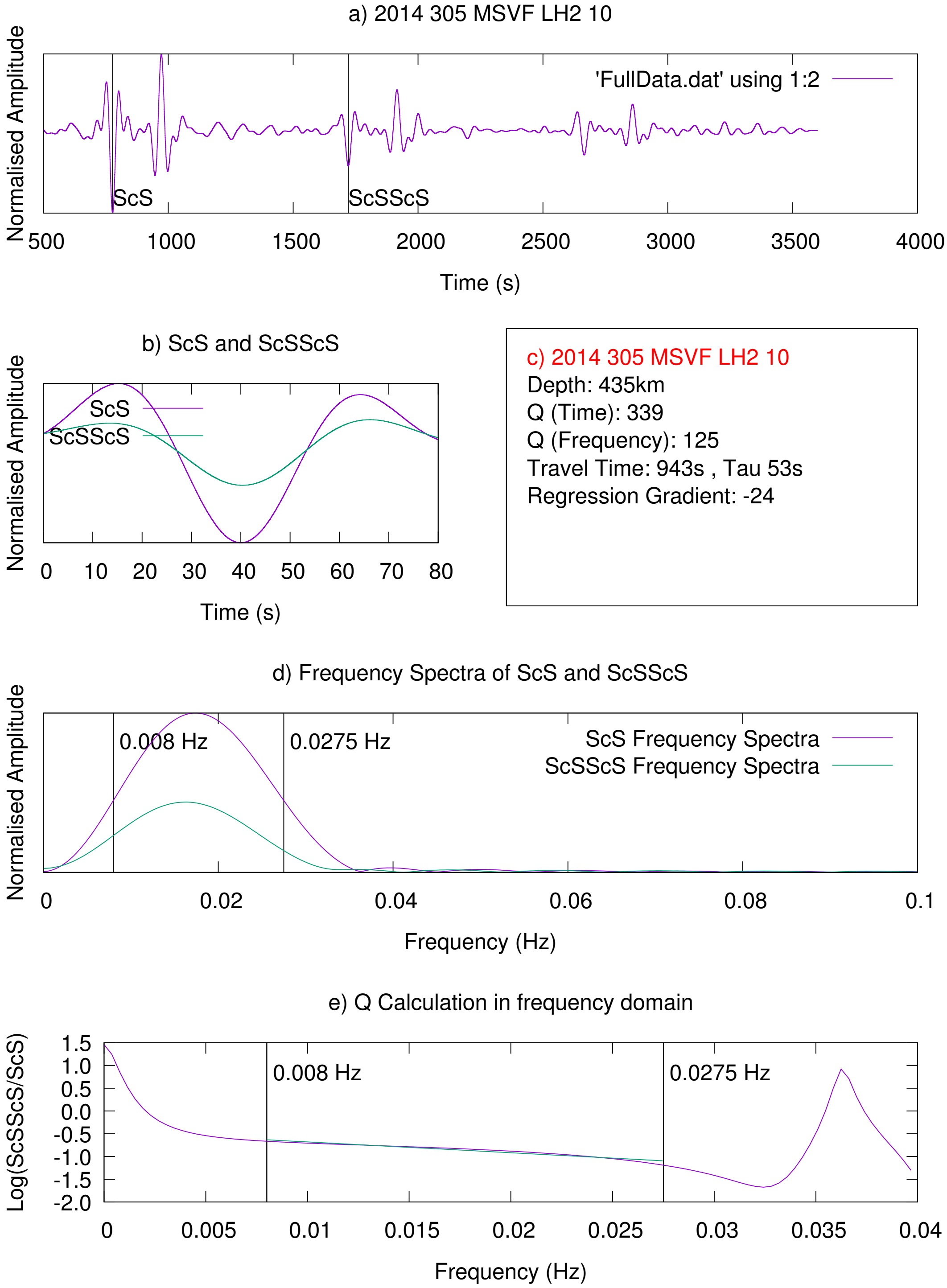

Figure A44: a) Seismogram after butterworth filtering and the locations of the ScS and ScSScS arrivals. b) 80 second ScS and ScSScS time windows plotted on top of eachother. c) Year and Day number (Normal Date: 01/11/2014), Station Name, Component, Instrument, Event depth, Q(time), Q(Frequency), time difference between ScS and ScSScS and the value of the frequency spectra gradient. d) The frequency spectra of the ScS and ScSScS phases and e) Graph upon which spectral gradient is calculated. The green line shows the line fitted through the data.

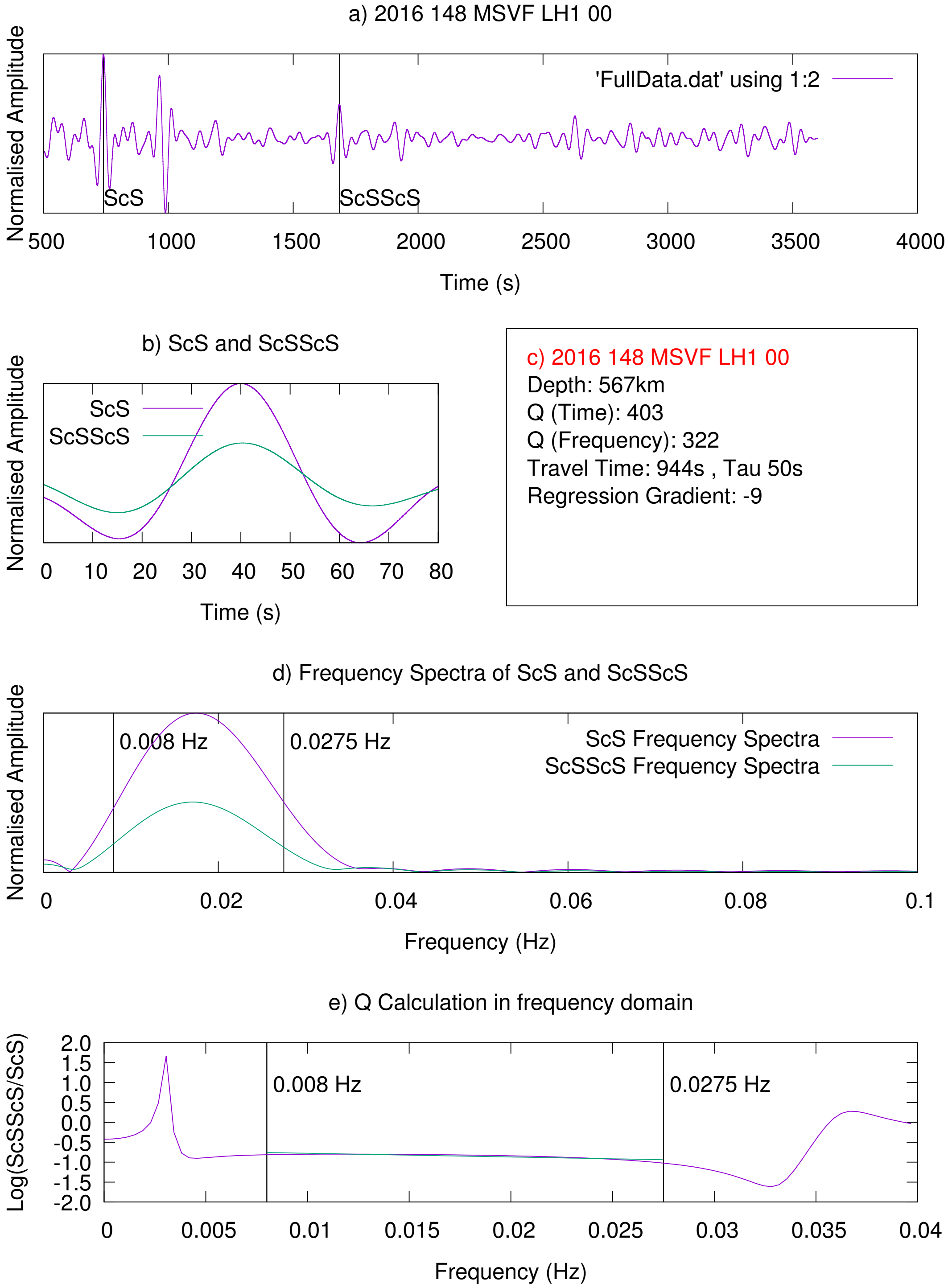

Figure A45: a) Seismogram after butterworth filtering and the locations of the ScS and ScSScS arrivals. b) 80 second ScS and ScSScS time windows plotted on top of eachother. c) Year and Day number (Normal Date: 27/05/2016), Station Name, Component, Instrument, Event depth, Q(time), Q(Frequency), time difference between ScS and ScSScS and the value of the frequency spectra gradient. d) The frequency spectra of the ScS and ScSScS phases and e) Graph upon which spectral gradient is calculated. The green line shows the line fitted through the data.

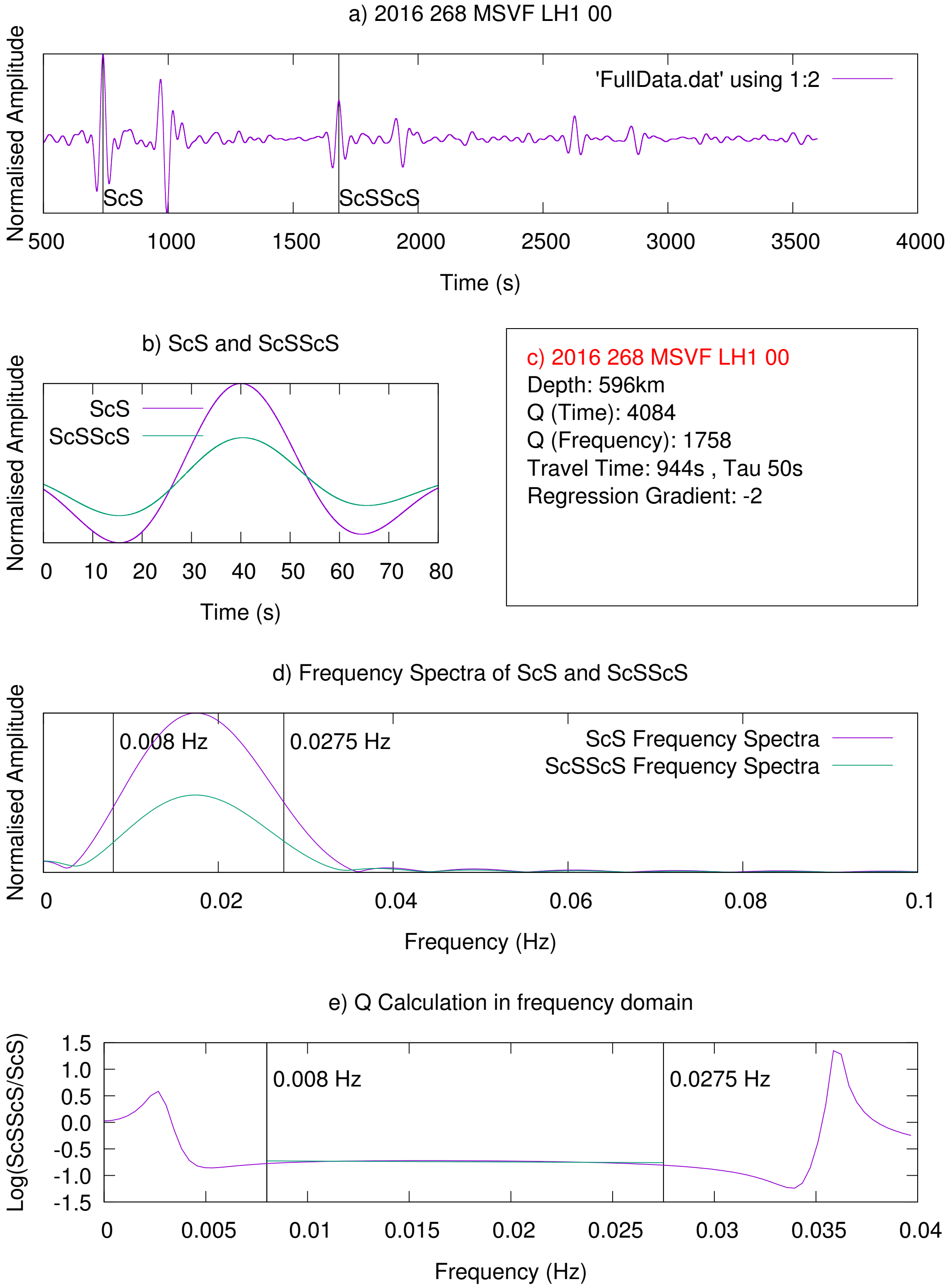

Figure A46: a) Seismogram after butterworth filtering and the locations of the ScS and ScSScS arrivals. b) 80 second ScS and ScSScS time windows plotted on top of eachother. c) Year and Day number (Normal Date: 24/09/2016), Station Name, Component, Instrument, Event depth, Q(time), Q(Frequency), time difference between ScS and ScSScS and the value of the frequency spectra gradient. d) The frequency spectra of the ScS and ScSScS phases and e) Graph upon which spectral gradient is calculated. The green line shows the line fitted through the data.

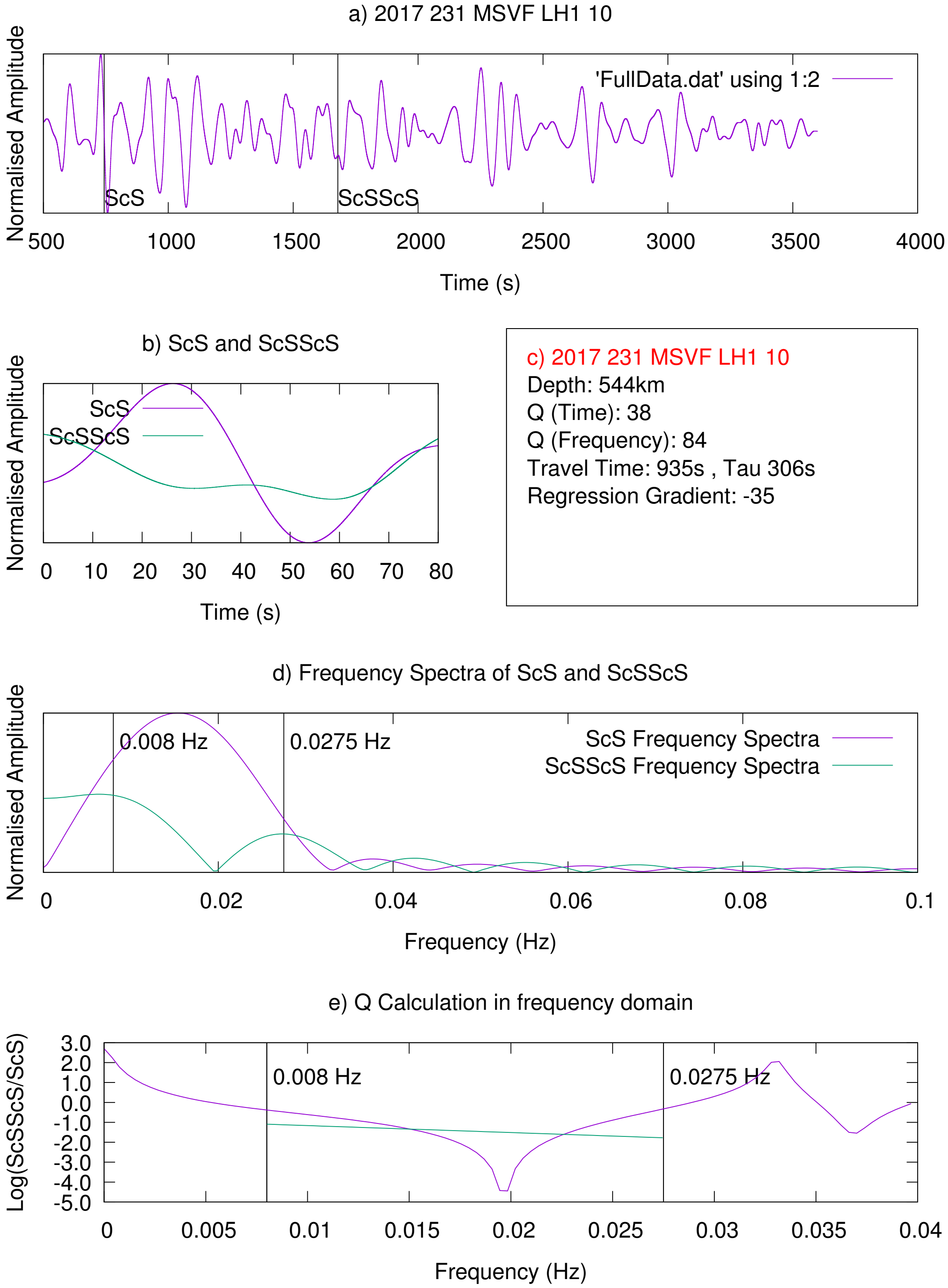

Figure A47: a) Seismogram after butterworth filtering and the locations of the ScS and ScSScS arrivals. b) 80 second ScS and ScSScS time windows plotted on top of eachother. c) Year and Day number (Normal Date: 19/08/2017), Station Name, Component, Instrument, Event depth, Q(time), Q(Frequency), time difference between ScS and ScSScS and the value of the frequency spectra gradient. d) The frequency spectra of the ScS and ScSScS phases and e) Graph upon which spectral gradient is calculated. The green line shows the line fitted through the data.

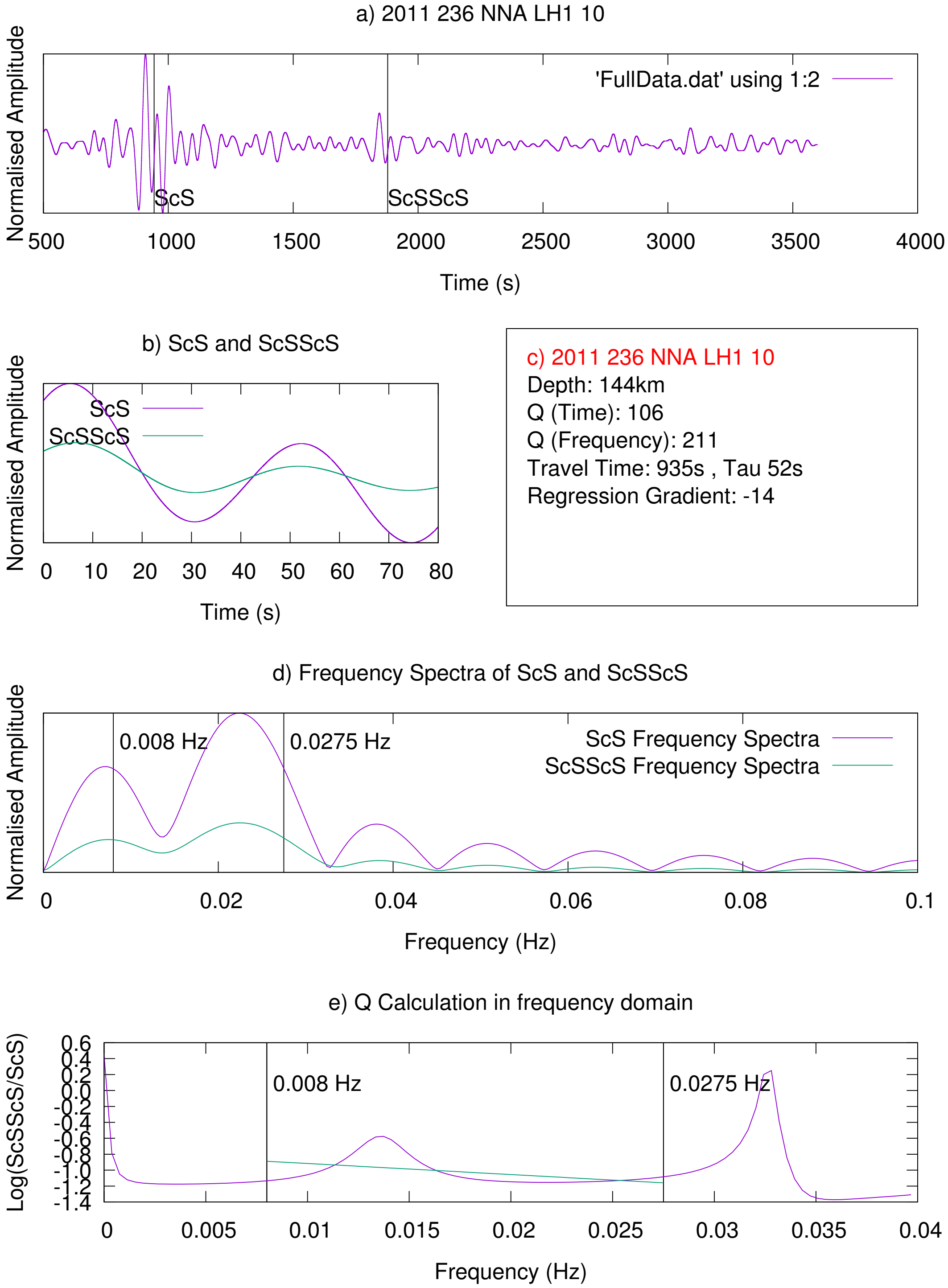

Figure A48: a) Seismogram after butterworth filtering and the locations of the ScS and ScSScS arrivals. b) 80 second ScS and ScSScS time windows plotted on top of eachother. c) Year and Day number (Normal Date: 24/08/2011), Station Name, Component, Instrument, Event depth, Q(time), Q(Frequency), time difference between ScS and ScSScS and the value of the frequency spectra gradient. d) The frequency spectra of the ScS and ScSScS phases and e) Graph upon which spectral gradient is calculated. The green line shows the line fitted through the data.

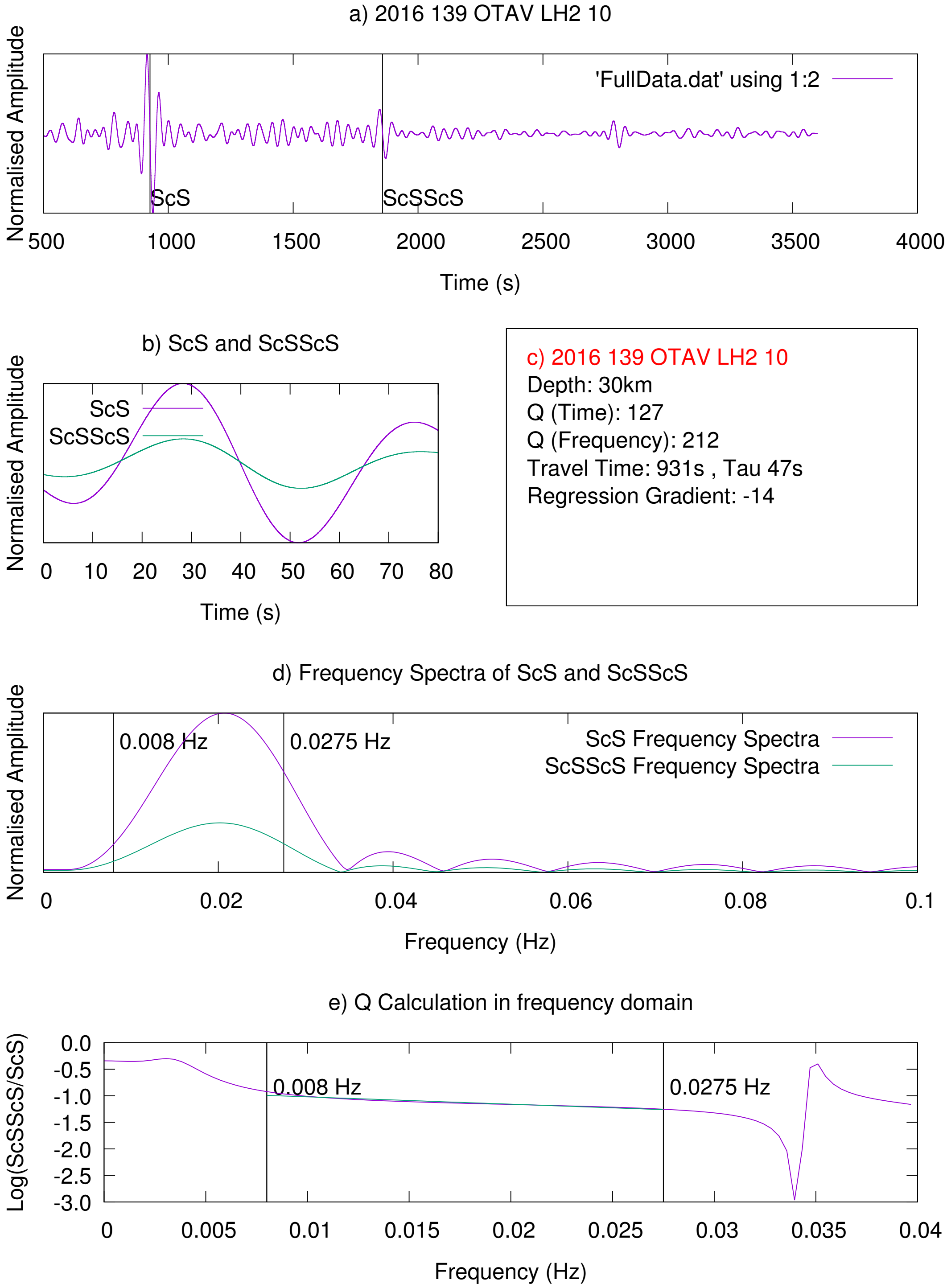

Figure A49: a) Seismogram after butterworth filtering and the locations of the ScS and ScSScS arrivals. b) 80 second ScS and ScSScS time windows plotted on top of eachother. c) Year and Day number (Normal Date: 18/05/2016), Station Name, Component, Instrument, Event depth, Q(time), Q(Frequency), time difference between ScS and ScSScS and the value of the frequency spectra gradient. d) The frequency spectra of the ScS and ScSScS phases and e) Graph upon which spectral gradient is calculated. The green line shows the line fitted through the data.

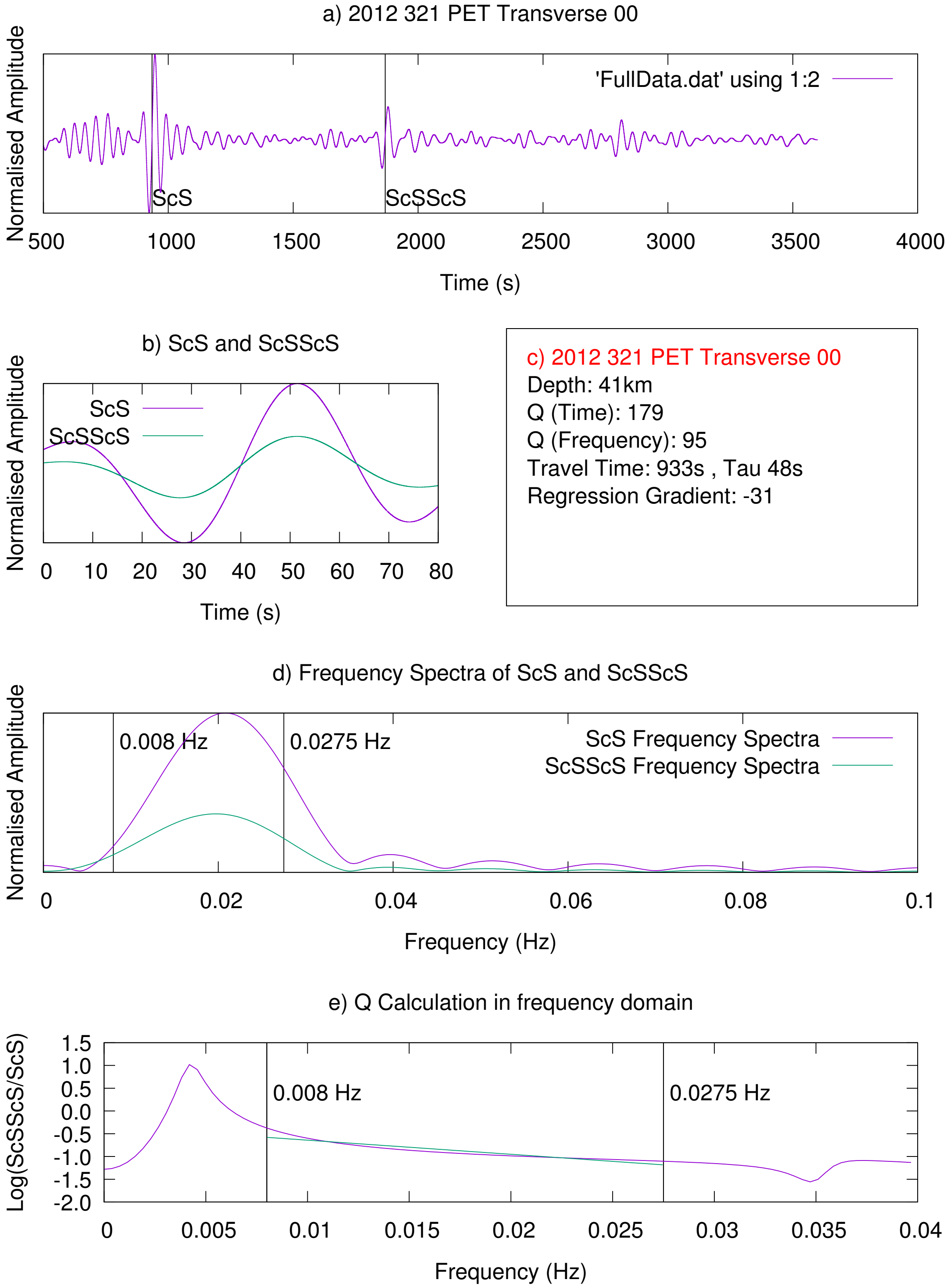

Figure A50: a) Seismogram after butterworth filtering and the locations of the ScS and ScSScS arrivals. b) 80 second ScS and ScSScS time windows plotted on top of eachother. c) Year and Day number (Normal Date: 16/11/2012), Station Name, Component, Instrument, Event depth, Q(time), Q(Frequency), time difference between ScS and ScSScS and the value of the frequency spectra gradient. d) The frequency spectra of the ScS and ScSScS phases and e) Graph upon which spectral gradient is calculated. The green line shows the line fitted through the data.

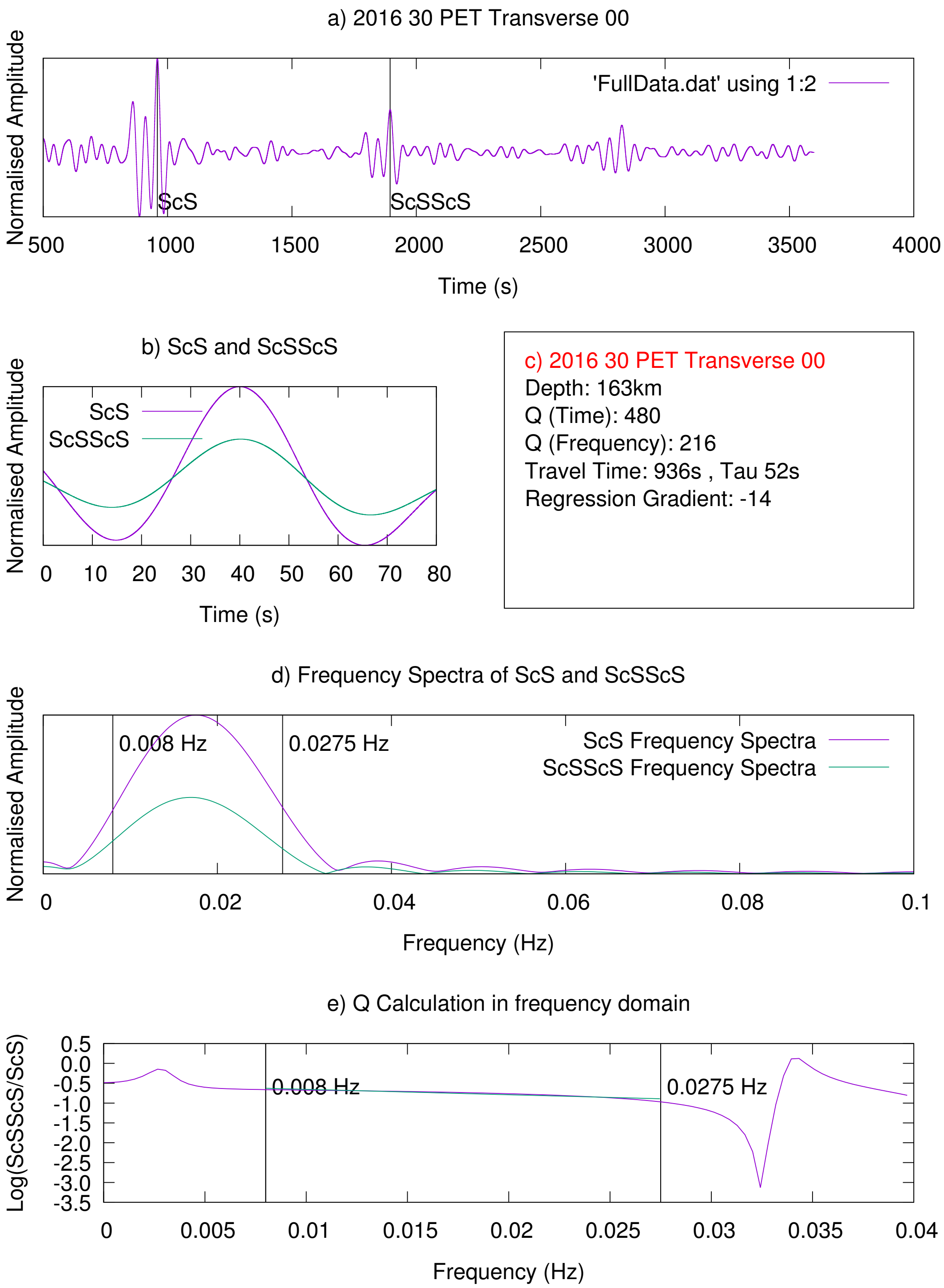

Figure A51: a) Seismogram after butterworth filtering and the locations of the ScS and ScSScS arrivals. b) 80 second ScS and ScSScS time windows plotted on top of eachother. c) Year and Day number (Normal Date: 20/03/2016), Station Name, Component, Instrument, Event depth, Q(time), Q(Frequency), time difference between ScS and ScSScS and the value of the frequency spectra gradient. d) The frequency spectra of the ScS and ScSScS phases and e) Graph upon which spectral gradient is calculated. The green line shows the line fitted through the data.

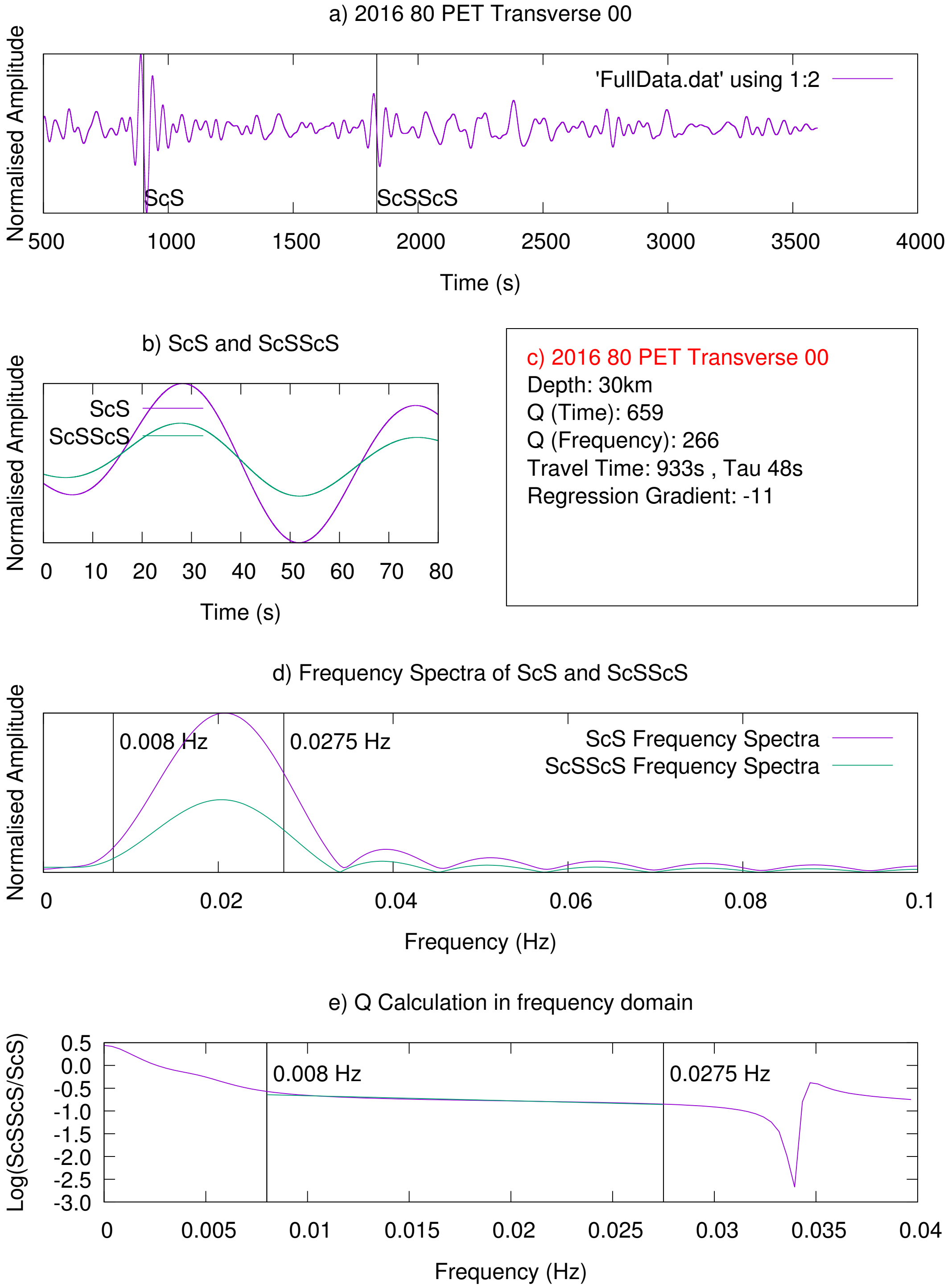

Figure A52: a) Seismogram after butterworth filtering and the locations of the ScS and ScSScS arrivals. b) 80 second ScS and ScSScS time windows plotted on top of eachother. c) Year and Day number (Normal Date: 20/03/2016), Station Name, Component, Instrument, Event depth, Q(time), Q(Frequency), time difference between ScS and ScSScS and the value of the frequency spectra gradient. d) The frequency spectra of the ScS and ScSScS phases and e) Graph upon which spectral gradient is calculated. The green line shows the line fitted through the data.

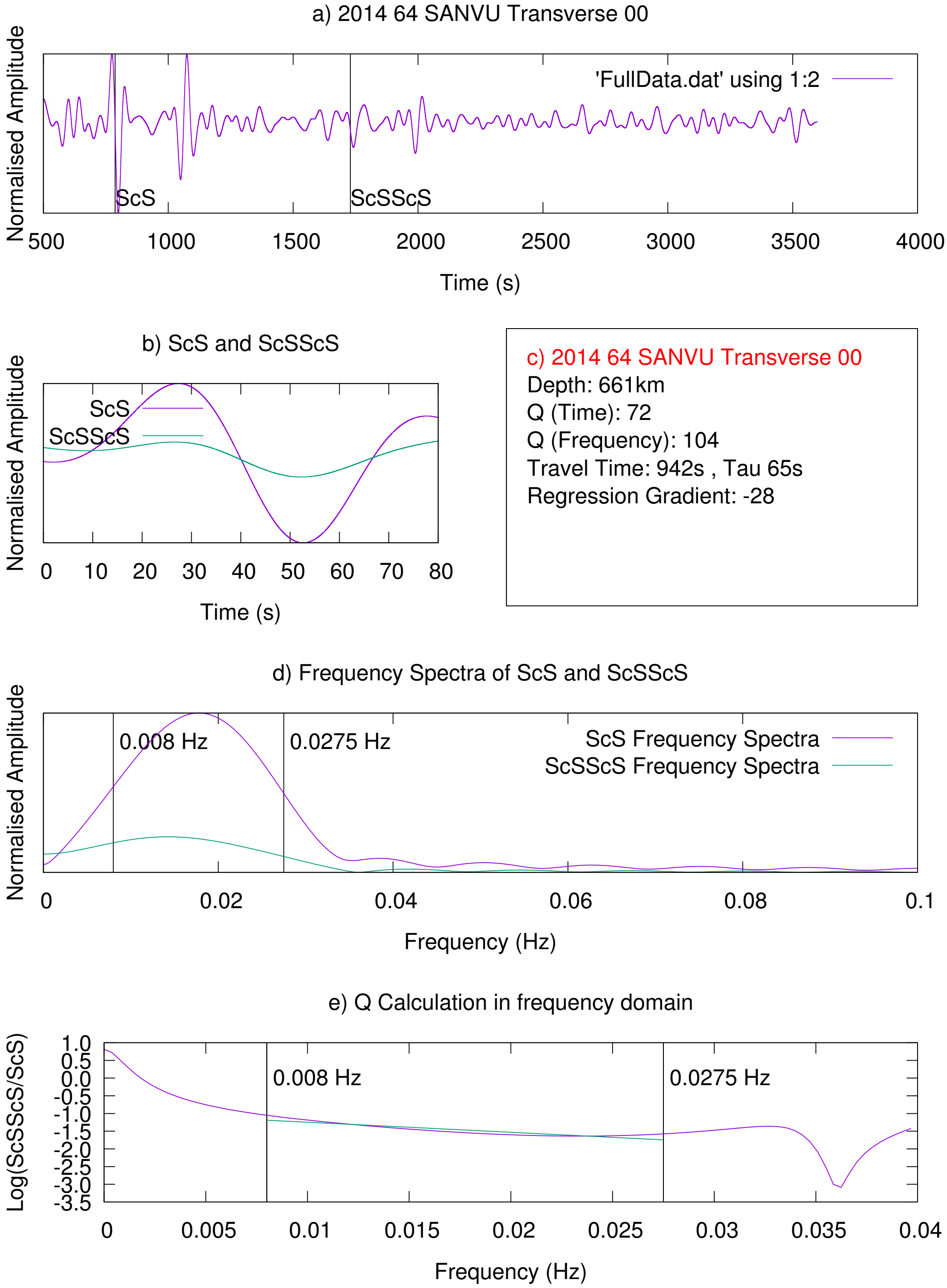

Figure A53: a) Seismogram after butterworth filtering and the locations of the ScS and ScSScS arrivals. b) 80 second ScS and ScSScS time windows plotted on top of eachother. c) Year and Day number (Normal Date: 05/03/2014), Station Name, Component, Instrument, Event depth, Q(time), Q(Frequency), time difference between ScS and ScSScS and the value of the frequency spectra gradient. d) The frequency spectra of the ScS and ScSScS phases and e) Graph upon which spectral gradient is calculated. The green line shows the line fitted through the data.

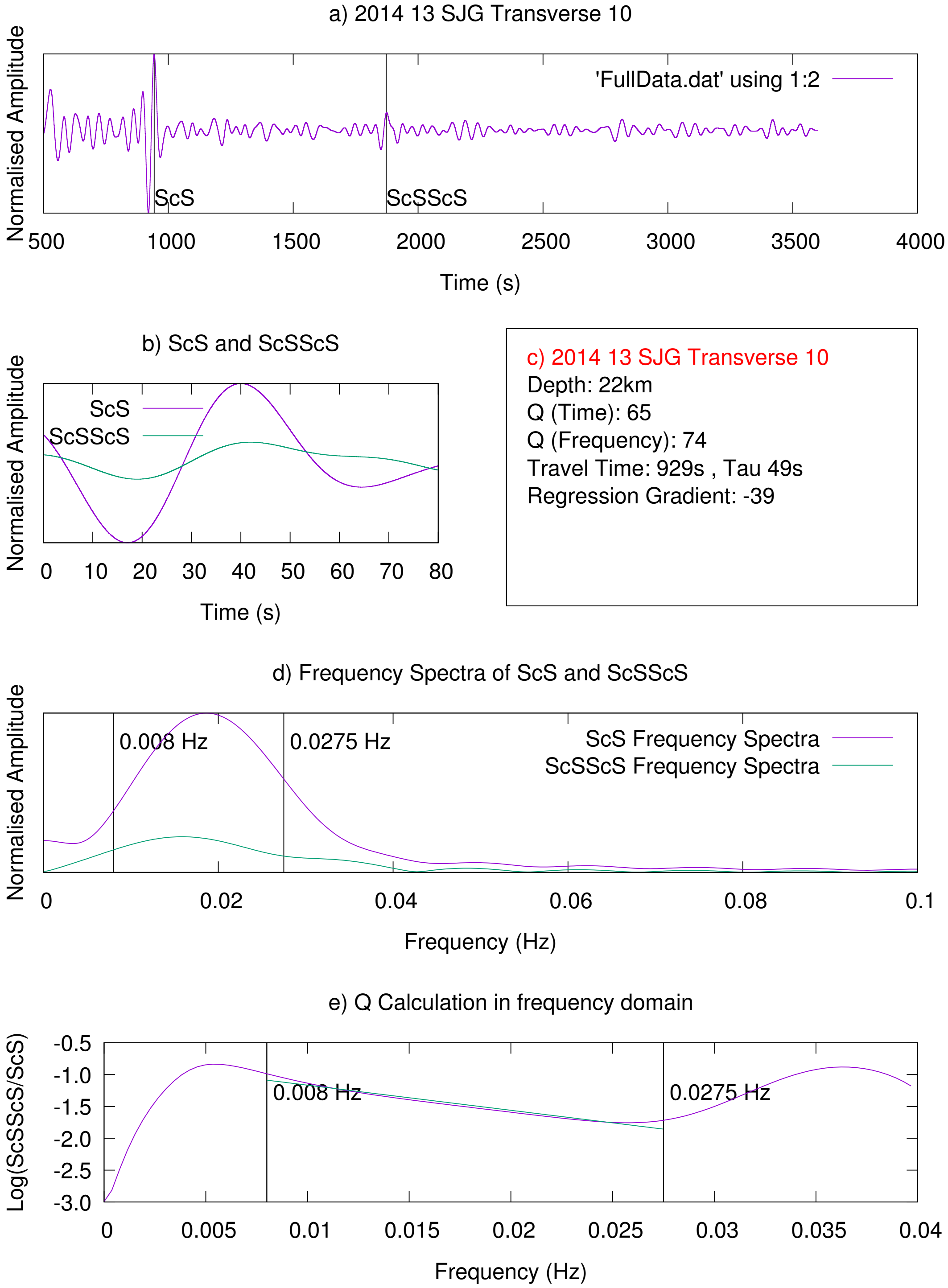

Figure A54: a) Seismogram after butterworth filtering and the locations of the ScS and ScSScS arrivals. b) 80 second ScS and ScSScS time windows plotted on top of eachother. c) Year and Day number (Normal Date: 13/01/2014), Station Name, Component, Instrument, Event depth, Q(time), Q(Frequency), time difference between ScS and ScSScS and the value of the frequency spectra gradient. d) The frequency spectra of the ScS and ScSScS phases and e) Graph upon which spectral gradient is calculated. The green line shows the line fitted through the data.

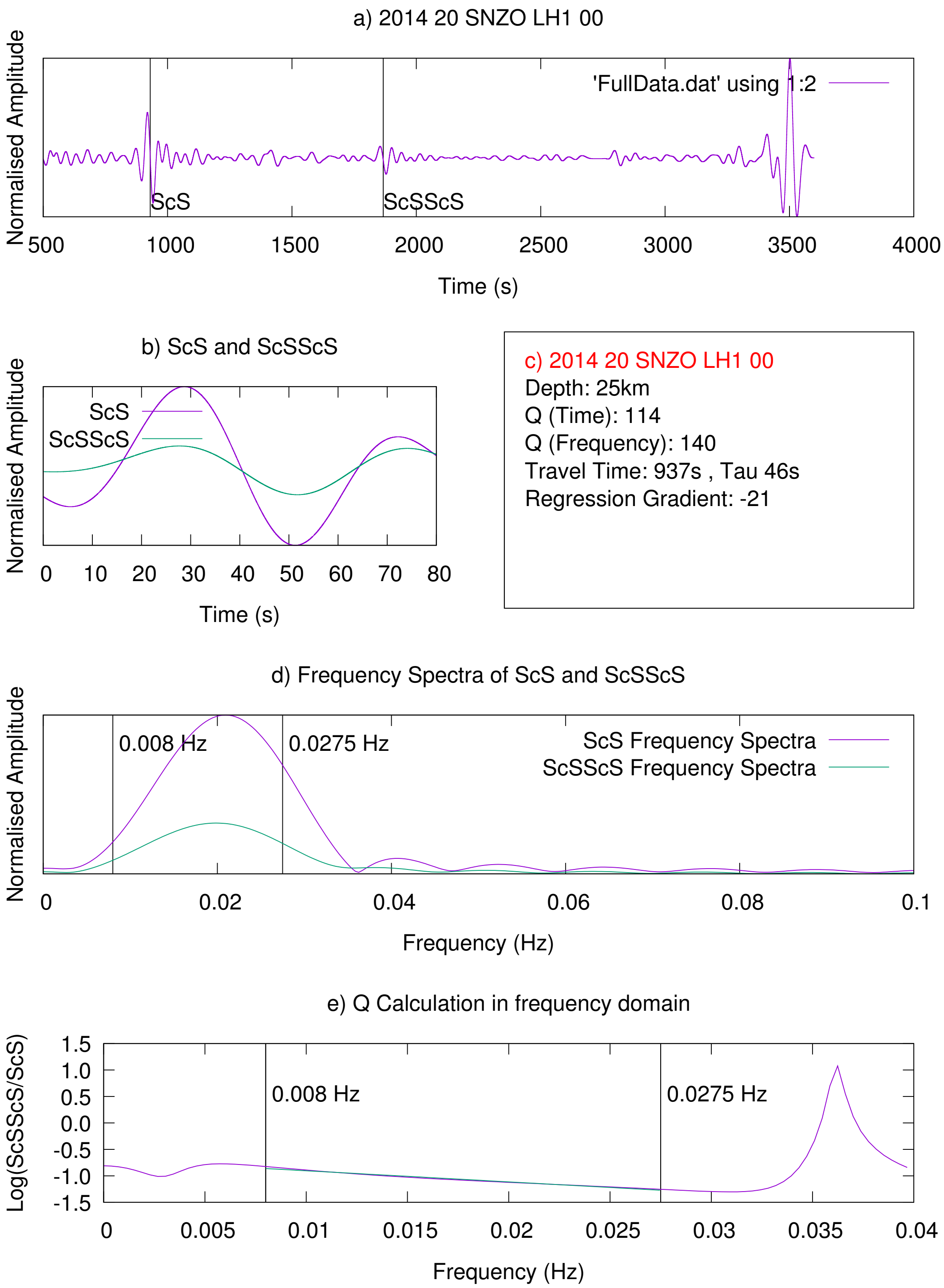

Figure A55: a) Seismogram after butterworth filtering and the locations of the ScS and ScSScS arrivals. b) 80 second ScS and ScSScS time windows plotted on top of eachother. c) Year and Day number (Normal Date: 20/01/2014), Station Name, Component, Instrument, Event depth, Q(time), Q(Frequency), time difference between ScS and ScSScS and the value of the frequency spectra gradient. d) The frequency spectra of the ScS and ScSScS phases and e) Graph upon which spectral gradient is calculated. The green line shows the line fitted through the data.

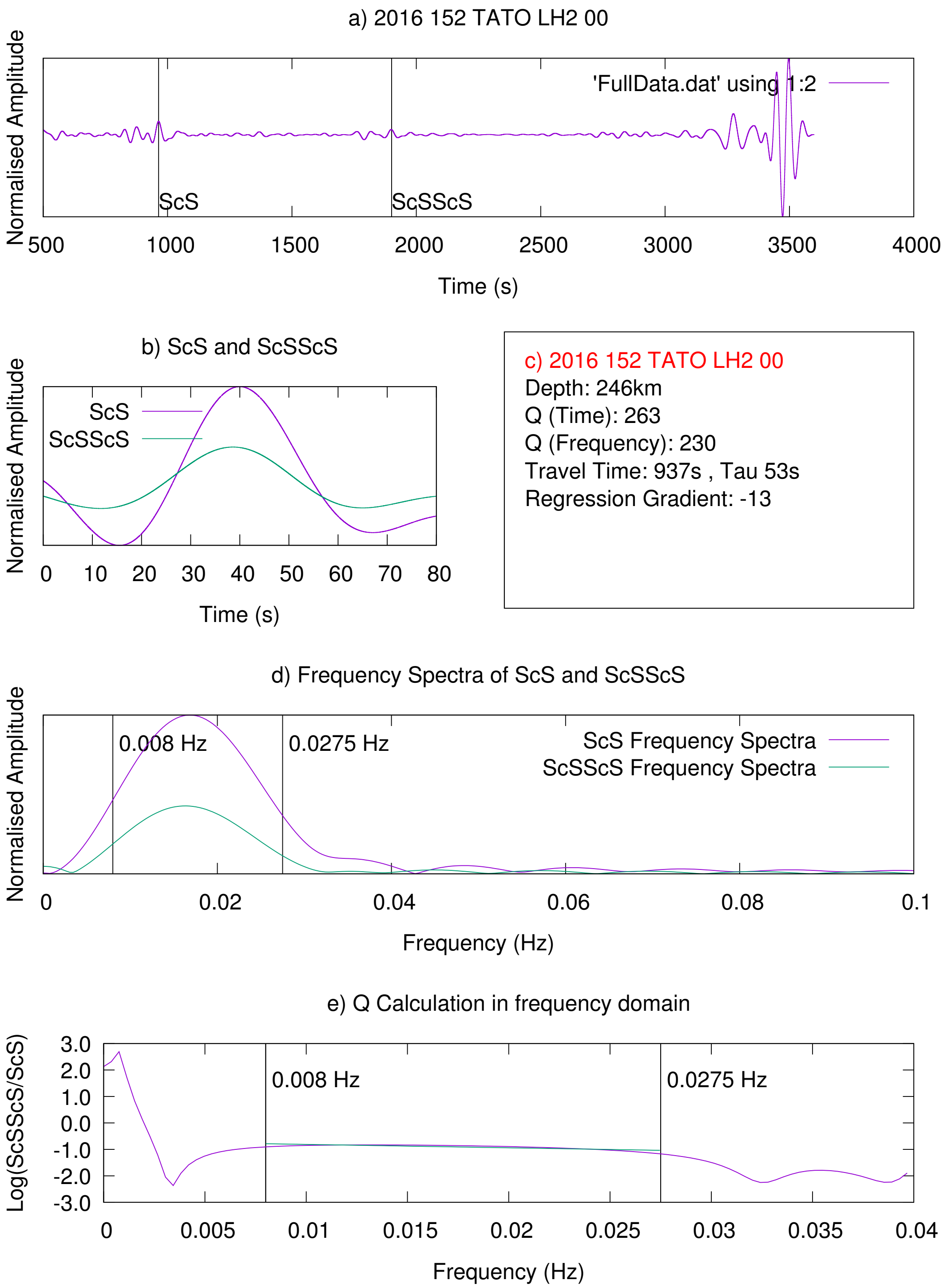

Figure A56: a) Seismogram after butterworth filtering and the locations of the ScS and ScSScS arrivals. b) 80 second ScS and ScSScS time windows plotted on top of eachother. c) Year and Day number (Normal Date: 31/05/2016), Station Name, Component, Instrument, Event depth, Q(time), Q(Frequency), time difference between ScS and ScSScS and the value of the frequency spectra gradient. d) The frequency spectra of the ScS and ScSScS phases and e) Graph upon which spectral gradient is calculated. The green line shows the line fitted through the data.

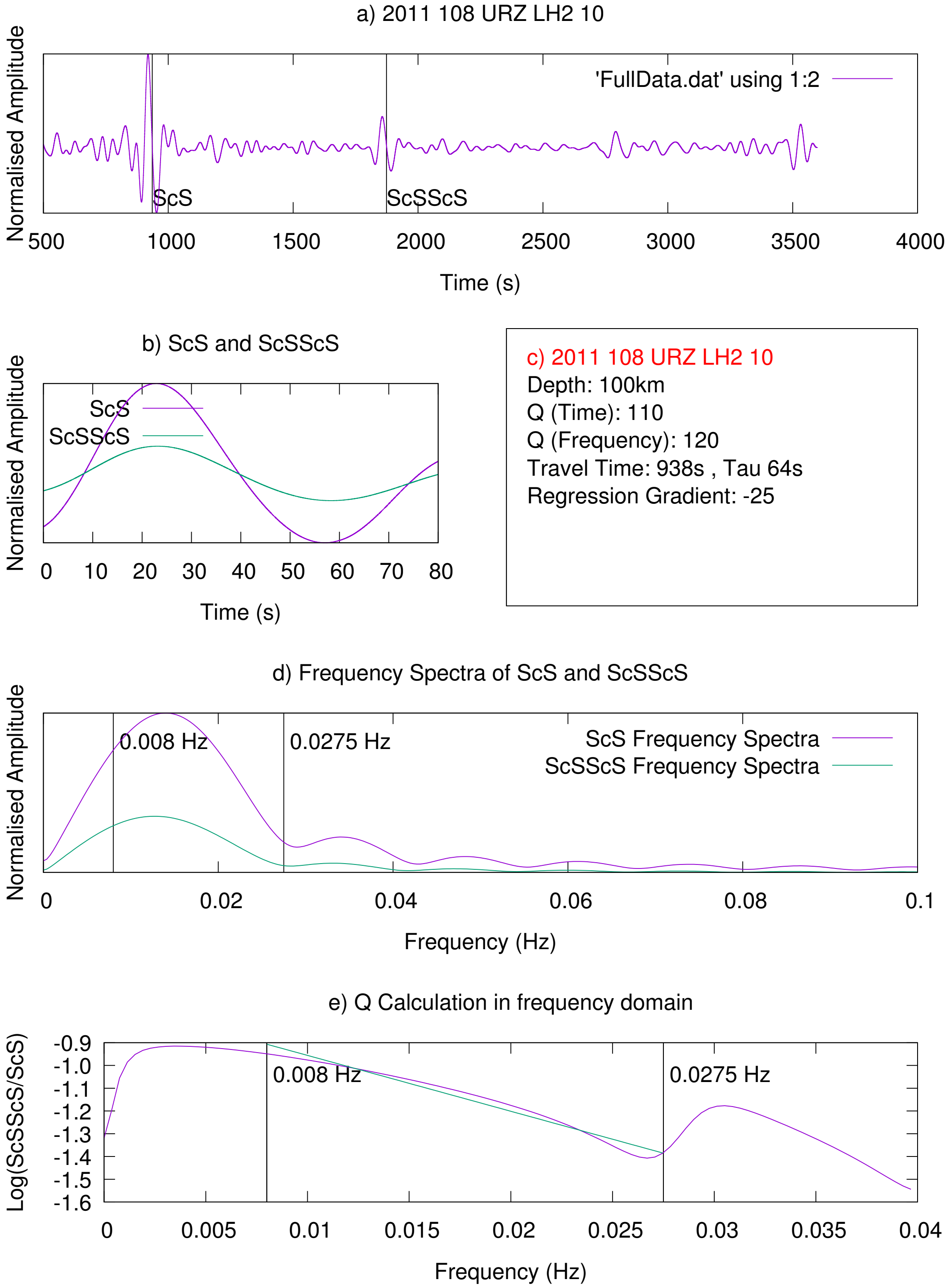

Figure A57: a) Seismogram after butterworth filtering and the locations of the ScS and ScSScS arrivals. b) 80 second ScS and ScSScS time windows plotted on top of eachother. c) Year and Day number (Normal Date: 18/04/2011), Station Name, Component, Instrument, Event depth, Q(time), Q(Frequency), time difference between ScS and ScSScS and the value of the frequency spectra gradient. d) The frequency spectra of the ScS and ScSScS phases and e) Graph upon which spectral gradient is calculated. The green line shows the line fitted through the data.

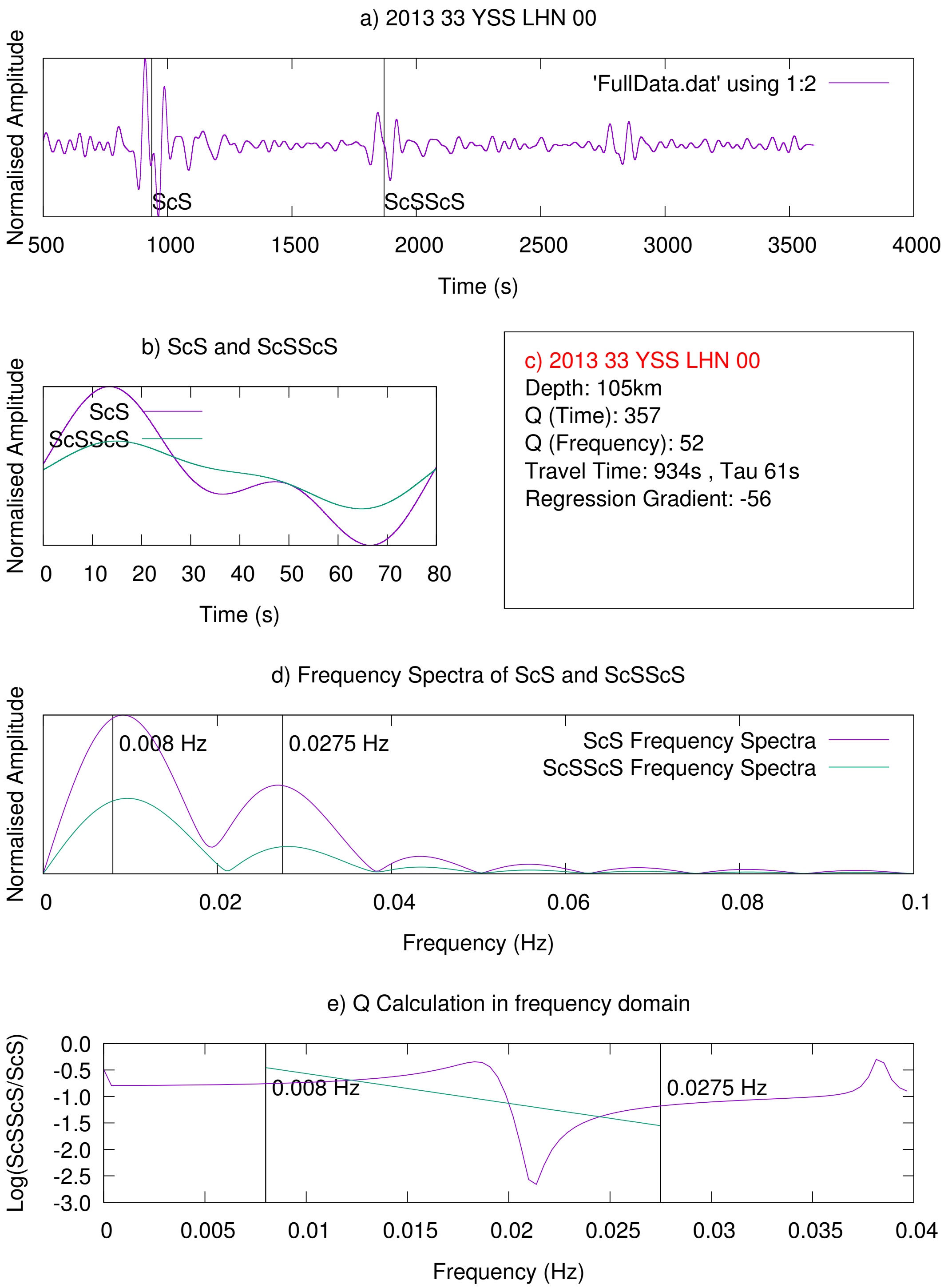

Figure A58: a) Seismogram after butterworth filtering and the locations of the ScS and ScSScS arrivals. b) 80 second ScS and ScSScS time windows plotted on top of eachother. c) Year and Day number (Normal Date: 02/02/2013), Station Name, Component, Instrument, Event depth, Q(time), Q(Frequency), time difference between ScS and ScSScS and the value of the frequency spectra gradient. d) The frequency spectra of the ScS and ScSScS phases and e) Graph upon which spectral gradient is calculated. The green line shows the line fitted through the data.